SURFACE PLASMON ENHANCED OPTICAL PROPERTIES OF COMPLEX SHAPED GOLD NANOPARTICLES

by

Achyut Maity

(Enrolment No.-PHYS05201204003)

Saha Institute of Nuclear Physics, Kolkata

A thesis submitted to the
Board of Studies in Physical Sciences

In partial fulfillment of requirements
for the degree of
DOCTOR OF PHILOSOPHY
of
HOMI BHABHA NATIONAL INSTITUTE

July, 2017

Homi Bhabha National Institute

Recommendations of the Viva Voce Committee

As members of the Viva Voce Committee, we certify that we have read the dissertation prepared by ACHYUT MAITY entitled "SURFACE PLASMON ENHANCED OPTICAL PROPERTIES OF COMPLEX SHAPED GOLD NANOPARTICLES" and recommend that it may be accepted as fulfilling the thesis requirement for the award of Degree of Doctor of Philosophy.

Chairman - Prof. Satyaranjan Bhattacharyya **Date:** 06/10/2017
SBhattacharyya

Guide / Convener - Prof. Tapas Kumar Chini **Date:** 06/10/2017
Tapas kumar Chini

Co-guide - NA **Date:**

Examiner - Dr. Dipak Kumar Goswami **Date:** 06/10/2017
DKgoswami

Member 1- Dr. Biswarup Satpati **Date:** 06/10/17
Biswarup Satpati

Member 2- Prof. Supratic Chakraborty **Date:** 06/10/17
Supratic Chakraborty

Final approval and acceptance of this thesis is contingent upon the candidate's submission of the final copies of the thesis to HBNI.

I/We hereby certify that I/we have read this thesis prepared under my/our direction and recommend that it may be accepted as fulfilling the thesis requirement.

Date: 6/10/2017

Place: Kolkata

Tapas kumar Chini

Co-guide (if applicable) **Guide**

STATEMENT BY AUTHOR

This dissertation has been submitted in partial fulfillment of requirements for an advanced degree at Homi Bhabha National Institute (HBNI) and is deposited in the Library to be made available to borrowers under rules of the HBNI.

Brief quotations from this dissertation are allowable without special permission, provided that accurate acknowledgement of source is made. Requests for permission for extended quotation from or reproduction of this manuscript in whole or in part may be granted by the Competent Authority of HBNI when in his or her judgment the proposed use of the material is in the interests of scholarship. In all other instances, however, permission must be obtained from the author.

Achyut Maity

DECLARATION

I, hereby declare that the investigation presented in the thesis has been carried out by me. The work is original and has not been submitted earlier as a whole or in part for a degree / diploma at this or any other Institution / University.

Achyut Maity

List of Publications arising from the thesis

Peer reviewed journals

1. *Probing Localized Surface Plasmons of Trisoctahedral Gold Nanocrystals for Surface Enhanced Raman Scattering.*
   A. Maity, A. Maiti, B. Satpati, A. Patsha, S. Dhara, and T. K. Chini, *J. Phys. Chem. C*, **2016**, 120, 27003.

2. *Effect of Intertip Coupling on the Plasmonic Behavior of Individual Multitipped Gold Nanoflower.*
   A. Maity, A. Maiti, P. Das, D. Senapati, and T. K. Chini, *ACS Photonics*, **2014**, 1, 1290.

Conference proceedings

1. *Trisoctahedral gold nanocrystal: A promising candidate for the study of plasmonics using cathodoluminescence.*
   A. Maity, A. Maiti, B. Satpati, and T. K. Chini, *AIP Conf. Proc.* **2016**, 1731, 80026.

Conference & Workshop presentations

1. Poster Presentation at The 8th International Conference on Surface Plasmon Photonics (SPP8, May 22-26, 2017), Academia Sinica, Taipei, Taiwan with the topic entitled with *Imaging Surface Plasmonic Modes of Individual Complex Shaped Gold Nanoparticle using Cathodoluminescence.*

2. Paper Presentation at 60th DAE Solid State Physics Symposium (December 21-25, 2015), Amity University, Uttar Pradesh, Noida, India with the

topic entitled with *Complex Shaped Au Trisoctahedral (TOH) Particle: A Promising Candidate for Plasmonics Study.*

3. Participation at International Workshop On Emerging Areas in Photonics and Future Applications (IWPFA-2015, December 7-12, 2015), CSIR-Central Glass & Ceramic Research Institute, Kolkata, India.

4. Participation at Current Trends in Research on Electron Microscopy in Material Science (December 22, 2014), CSIR-Central Glass & Ceramic Research Institute, Kolkata, India.

5. Poster Presentation at International conference on Electron Microscopy and XXXIV Annual Meeting of the Electron Microscope Society of India (July 3-5, 2013), Saha Institute of Nuclear Physics, Kolkata, India with the topic entitled with *Plasmon Assisted Photon Emission from Fast Electron Excited Metal Nanoparticle: A Finite-Difference Time-Domain Numerical Approach.* ***2013***

Achyut Maity

Dedicated to my "Family" and "Teachers"

Acknowledgements

Once I was like every other master degree student in India, with a dream of pursuing Ph.D degree for higher study. Yet, I could never have imagined a successful Ph.D journey so fulfilling. No dream is ever chased alone. As I look back I have many people to thank for their great support that I have received over past 5 years during my Ph.D tenure. Before I mention some of them, I would like to apologize to everyone who is not mentioned.

First of all, I would like to acknowledge my thesis and research advisor, Prof. Tapas Kumar Chini. There is no proper words to convey my deepest gratitude and respect for him. He has inspired me to become an independent researcher and helped me realize the power of critical reasoning. He also demonstrated what a brilliant and hard-working scientist can accomplish. His enthusiasm and unmatched support, coupled with his tremendous care to ensure my career were going as I wished, made him a great advisor and also a excellent friend. One simply could not wish for a better or friendlier supervisor. Your indefatigable work ethic and boundless curiosity and enthusiasm, over-lavish encouragement and thoughtfully over-delicate feedback and the style to celebrate joyful moments of paper publication are really awesome. Thank you very much Tapas-da.

Besides my advisor, I would like to thank the rest of my doctoral committee members: Prof. Satyaranjan Bhattacharyya, Dr. Biswarup Satpati, Prof. Supratic Chakraborty. They generously gave their time to offer me strong support, encouragement, and valuable advice toward improving my work. Thank you for keeping your office doors open and available always when I needed it. I take here the opportunity to acknowledge useful suggestions and help from every faculty members of the Surface Physics and Material Science Division. I would like to thank Prof. Milan Kumar Sanyal, the former Director, and Prof. Ajit Kumar Mohanty, the present Director, Saha Institute of Nuclear Physics, for giving me the opportunity to work in the institute and utilize its resources and also for providing me all kinds of necessary financial support.

I would also like to specially thank my collaborators, who gave so freely of their time and their talents. Thanks to Prof. Sandip Dhara and Dr. Avinash Patsha

of Indira Gandhi Centre for Atomic Research for their crucial help and wonderful analysis of SERS data. Thank you Avinash for all of the meetings, chats and discussions.

Many thanks to Prof. Dulal Senapati and his group of Saha Institute of Nuclear Physics, for providing us gold nanoflower samples. A special thanks to Dr. Munmun Bardhan, Mairayee Bhattacharya and Sudeshna Das Chakraborty for their valuable comments and advice about chemical synthesis of gold nanoparticles.

My acknowledgement will never be complete without the special mention of my lab senior, Pabitra Das, who taught me the lab culture and have lived by example to make me understand the hard facts of life. I can never forget my dearest senior Pabitra-da, who taught me all the possible techniques in a very short time before he left the lab. Even after leaving from the lab, I never faced any problem as he is a very kind person who replied my mails full of questions and doubts immediately. The work done with him as a co-worker has taught me how a person can succeed in achieving what seems impossible to begin with. Thanks a ton Pabitra-da for your great support and discussion, in the lab, outside the lab, or in front of a drink at any party.

I want to thank Arpan Maiti who as a good friend and amazing lab mate was always willing to help and give his best suggestions. It would have been a lonely lab without him.

A substantial amount of time of PhD life is spent with seniors, friends and juniors. I would like to thank Sirshendu-da, Abhishak-da, Shyamal-da, Debasree-di, Debraj-da, Arpan-da, Uttam-da, Jayanta-da, Suvankar-da, Tanmay-da, Tanusree-di, Anwesha-di, Sourav, Asish, Abdul, Rajendra, Debaleen, Mithun, Abhijit, Arijit, Arka, Pintu, Anindita, Gourav, Abhijit, Bibhuti, Samrat, Abhishek for their timely support and being so trustworthy.

It is a pleasure to thank my Post M.Sc batchmets at the SINP, Aritra, Chiranjib, Nausad, Anshu, Ashim, Amrita, Tapas, Sabuj, Sukanto, Gouranga, Kuntal (Nayek), Kuntal (Mondal), Tirthankar, Sanjukta, Binita, Sanjib, Pankaj, Debajyoti, Suvankar, Kamalendu, Mily, Sourav, Tapas (Paul), Kumar, Sudip, Hena, Chitralekhha, Barnamala for the wonderful times we shared, specially the outing trips or picnic or the weekend get-togethers. Thank you guys for being friends in true sense of the term for a long time. I think there are very few lucky people who share the good and bad times during the wonderful days of Ph.D with such wonderful friends and among them, I feel myself the luckiest one in this regard. In addition, my sincere and loving thanks to all my friends in school, college, university, Biplab, Shuvasis, Arpan, Sourav, Bappa, Sabyasachi, Saikat, Krishna, for being with me and their support. I will always remember you guys.

My special thanks goes to my best ever friend and enemy, Sayanee, whose continuous support was always with me during the Ph.D. Your zeal, sincerity, honesty and pace of working towards science give me inspiration for doing science. I thank you for boosting up my moral and not letting me down anytime. Without your support, it would have been a dream only to become a doctor of philosophy.

And most of all, I would like to share this moment of happiness with my loving, supportive, encouraging, family where the most basic source of my life energy resides. The support of my parents has been unconditional all these years and without their encouragement, prayers and understanding it would have been impossible for me to finish this work. I very fondly acknowledge my elder brothers and their sweet and lovely wives, and kids, Titli, Jhilik, Tathoi and Titir for their love and support. I sincerely thank all my relatives who were with me for their love and encouragement.

Finally, I would like to thank everybody who was important to the successful realization of this Thesis, as well as expressing my apology that I could not mention personally one by one.

SINP, Kolkata
July, 2017 Achyut Maity

Contents

Synopsis

In the search for new optical materials contributing towards localized surface plasmon resonance (LSPR), the study of metal nanoparticles (MNPs) of various shape and sizes has been a major focus of research in the area of photonics. LSPR is a result of resonant collective oscillations of conduction band electrons in MNPs and exhibits strong enhancement of near electromagnetic (EM) field intensity at surface of MNPs, as well as, the enhancement of the far-field scattering by the particle.[1, 2] The EM field enhancement from such plasmonic metal nanostructures shows remarkable applications in biosensing and bioimaging,[3, 4] photovoltaics,[5, 6] optical trapping [7] and surface-enhanced Raman scattering (SERS),[8] which develop the basis of a rapidly developing field of research in nano-photonics called plasmonics.[1, 9-11] Additionally, the LSPR condition also shows a remarkable enhancement of the near-field at the surface of the MNP, especially localized in the regions of sharp edges, corners, tips, and apex, depending on the complexity of the morphology of the nanoparticles. The regions characterized by highly localized and strongly enhanced electromagnetic (EM) fields, known as plasmonic hot spots, are responsible to manipulate light-matter interactions and boost non-linear phenomena. For instance, MNPs much smaller than the wavelength of light have been considered as the potential candidate for the massive signal enhancement achieved in SERS. The powerful vibrational spectroscopy technique is mainly governed by the amplification of EM fields generated through the excitation of LSPs of the SERS substrate. The SERS activity crucially depends on the LSP properties of MNPs on selected substrate. The noble MNPs (Ag and Au) are most commonly used for SERS activity, in the form of colloidal solution, as well as, solid substrates because of their unique optical properties. The three major factors involved in the Raman enhancement by MNPs are the size, shape and relative position of the NPs. Furthermore, the enhanced field associated with SPs makes them suitable for use as sensors, and commercial systems have already been developed for sensing biomolecules. Moreover, the particles having sharp surface curvatures and tips may provide multiple hotspots at their curvatures, tips and also at the junction between two or more NPs. The particles having sharp surface curvatures and tips like nanoprism,[12-14] nanorod,[15] nanodecahedra,[16-18] and nanostar/flower [19] are exploited extensively owing to the strong localization of the EM fields at their sharp corners or tips. Therefore, it is highly demanding to understand the LSP properties of individual MNPs of complex shaped geometry while using them for SERS activity, in the form ensemble MNPs on solid substrates.

In this context, the single particle LSPR spectroscopy is a most powerful technique that has enough ability to explore or reveal properties of nanoparticle at single particle level which is often overlooked or neglected or mixed in the ensemble measurements. Most of the studies for real-space imaging of plasmonic resonances of MNPs utilizing optical far-field techniques (excitation and detection in the far-field) are diffraction limited and thus a spatial resolution with a length scale below 200 nm is not easily achievable. Other well-adapted techniques to probe LSPRs at the single NP level are photon scanning tunneling microscopy, scanning near-field optical microscopy (SNOM),[20] and apertureless SNOM.[21] These techniques can achieve better spatial resolution but often require fabrication of a very delicate probe in the form of a nanoscale sharp tip and may suffer from probe-sample interactions, distorting the signal of interest. In contrast, the use of tightly focused electron beam from electron microscope is reported to probe SPs either through detection of energy loss by the inelastically scattered electrons transmitted through the sample, called electron energy loss spectroscopy (EELS) [10, 11, 16] in case of scanning transmission electron microscopy (STEM)/transmission electron microscopy (TEM) or through detection of electron beam induced luminescence from the sample, called cathodoluminescence (CL) [13, 14, 22] in case of scanning electron microscopy (SEM). These local electron probes show excellent spatial resolution from about 20 nm (for SEM) to near atomic resolution level (for

STEM),[23] thereby providing a unique resource for studying single particle spectroscopy. The EELS probes a quantity close to the full EM local density of states (EMLDOS). On the other hand, the CL measures a different quantity called radiative EMLDOS.[24] As the electron beam can be raster scanned in SEM / STEM, one can also obtain the information about the spatial variations of the EMLDOS. Additionally, the EMLDOS is also accessed by recording a single spectrum at a fixed point.

The primary aim of this thesis is to directly visualize the spatial profile of the LSPR modes of surface plasmon enhanced optical properties of complex shaped gold nanoparticles like Au nanoflower (NF) and nanotrisoctahedron (TOH). The CL detection technique attached with SEM probes the scattering physics of the metal nanoobject as well as allows us to construct excitability photon maps and site specific spectra which are proportional to the local density of optical states (LDOS) of the structure. The surface enhanced Raman scattering (SERS) studies are partly carried out to demonstrate the significance of field enhancement under LSPR conditions in Au MNPs.The experimentally obtained spectral and photon imaging data were extensively analyzed using finite-difference time-domain (FDTD) numerical simulation to generate electric near field intensity maps along with the associated vectorial plots. Gold nanoparticles used in the present study were synthesized using a seed mediated chemical growth method. Finally the experimentally studies have been analyzed with 3D-FDTD numerical simulations.

I have studied CL spectroscopy and imaging on two different multitipped complex shaped (NF and TOH) geometries and demonstrate that the intensity of plasmon induced photon emission and LSPR position strongly depends on the particles size, shape (sharp edges and corners) as well as on the substrate on which they are sitting. In case of Au NF particle, I have studied the the effect of intertip coupling on the plasmonic behavior of individual multitipped gold nanoflower. It is the first experimental realization on the selective excitation of two closely lying tips from the same spherical core of a multitipped gold nanoparticle with flower-like morphology

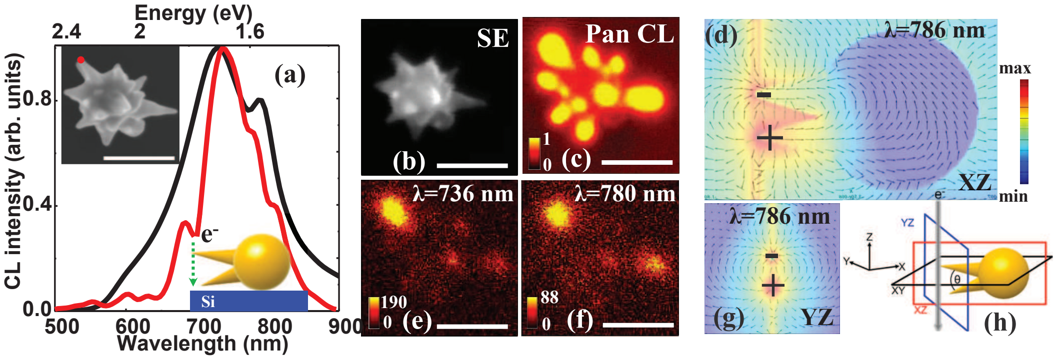

Figure 1: *(a) The experimentally acquired (red) and simulated CL (black) spectra from the in the wavelength range 500-700. (b) and (c) represent the SE and PAN CL image respectively. (e) and (f) represents the monochromatic CL images, whereas simulated near-field intensity* ($|E|^2$) *maps and the corresponding field maps are represented at (d) and (g). (h) Schematic diagram of the geometrical configuration of the Au NF along with the coordinate system used in the numerical simulation. nm.*

which also gives strong multipeaked resonance in the near-infrared region of the far-field emission spectra showing a clear signature of tip to tip coupling (shown in Figure 1). The simulated near field intensity maps acquired at the coupled LSPR mode show strong local field enhancement near the apex as well as in-between the closely lying upper and lower tip with strong dipolar charge oscillation. Besides, I have also studied the radiative localized surface plasmon resonance (LSPR) modes of an isolated single TOH Au nanoparticle with high resolution spatial information on the LDOS across the visible to near-IR (NIR) spectral range (shown in Figure 2). The CL analyses combined with FDTD simulations have helped us to identify two dipole-active LSP modes. The higher wavelength (low energy) surface plasmon mode is governed by the dipolar mode of oscillations between the apexes of the particle, which is basically 3-fold degenerate in nature. The dipolar oscillation is also active for lower wavelength (higher energy) LSP mode but charge pattern oscillation takes place between base and apex points along the in-plane and out-of-plane direction. The proximity of the substrate with respect to the point of excitation also plays a role, especially on the degenerate apex-apex LSP mode

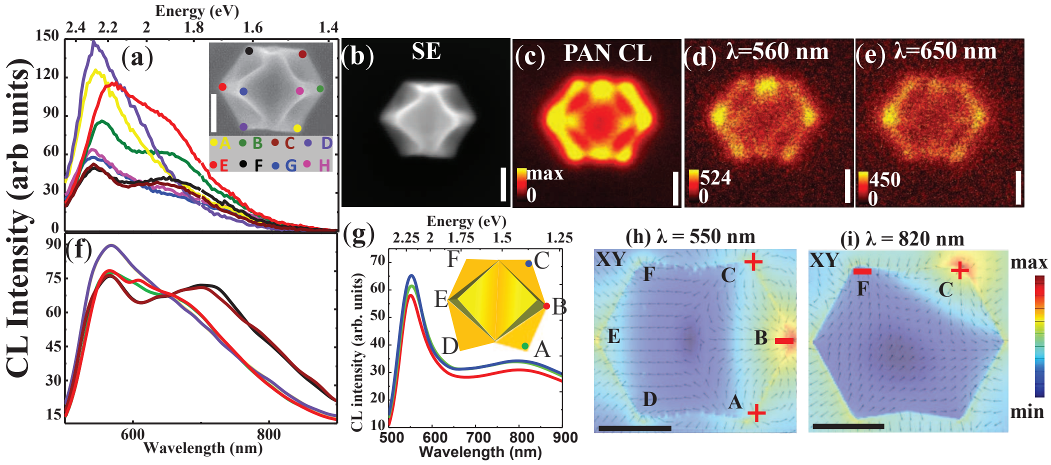

Figure 2: *(a) CL spectra from selected points marked as A-H of the studied TOH Au particle. The inset SEM image shows the electron beam impact points with different colored dots. The SEM image and the corresponding panchromatic CL map/image of the same morphology are shown in (b) and (c) respectively. (d)-(e) monochromatic CL maps/images. (f) 3D-FDTD simulated spectra of the modelled TOH structure for beam impact at the points (A, B..., F). (g) Simulated CL spectrum from the selected points of the TOH structure for modelling under free-standing configuration. (h) and (i) simulated near field intensity ($|E|^2$) and corresponding field vector maps at different resonant wavelengths.*

of nanoparticle due to inherent anisotropy and complexity of the TOH Au particle. Pronounced enhancement in the Raman scattering has also been reported by performing Raman spectroscopic measurements on Rhodamine 6G (R6G)-covered TOH Au NPs aggregates on a Si substrate.

In summary, I expect the results and conclusion that presented in this thesis, may lead a better way in understanding the LSPR properties of complex shaped metal nanoparticles at single particle level that might have far reaching consequences in light energy harvesting, optical communication, optical sensors, biosensing, and designing nanoparticle embedded solar cells.

Bibliography

[1] S. A. Maier, *Plasmonics: Fundamentals and Applications, Springer US* (2007).

[2] T. W. Odom, and G. C. Schatz, Chem. Rev. **111**, 3667-3668, (2011) .

[3] A. G. Brolo, Nat. Photonics. **6**, 709-713, (2012).

[4] X. Huang, I. H. El-Sayed, W. Qian and M. A. El-Sayed, J. Am. Chem. Soc. **128**, 2115-2120, (2006).

[5] H. A. Atwater and A. Polman, Nat. Mater. **9**, 205-213, (2010).

[6] A. Polman, Science, **322**, 868-869, (2008).

[7] M. L. Juan, M. Righini and R. Quidant, Nat. Photonics. **5**, 349-356, (2011).

[8] K. Kneipp, Y. Wang, H. Kneipp, L. T. Perelman, I. Itzkan, R. R. Dasari and M. S. Feld, Phys. Rev. Lett. **78**, 1667, (1997).

[9] S. A. Maier and H. A. Atwater, J. Appl. Phys. **98**, 011101, (2005).

[10] M. Koiak and O. Stéphan, Chem. Soc. Rev. **43**, 3865, (2014).

[11] F. J. García de Abajo, Rev. Mod. Phys. **82**, 209-275, (2010).

[12] J. Nelayah, M. Kociak, O. Stéphan, F. J. García De Abajo, M. Tencé, L. Henrard, D. Taverna, I. Pastoriza-Santos, L. M. Liz-Marzán and C. Colliex, Nat. Phys. **3**, 348-353, (2007).

[13] P. Chaturvedi, K. H. Hsu, A. Kumar, K. H. Fung, J. C. Mabon and N. X. Fang, ACS Nano. **3**, 2965-2974, (2009).

[14] P. Das, T. K. Chini, and J. Pond, J. Phys. Chem. C. **116**, 15610-15619, (2012).

[15] P. Das and T. K. Chini, J. Phys. Chem. C. **118**, 26284-26291, (2014).

[16] V. Myroshnychenko, J. Nelayah, G. Adamo, N. Geuquet, J. Rodríguez-Fernández, I. Pastoriza-Santos, K. F. MacDonald, L. Henrard, L. M. Liz-Marzán, N. I. Zheludev, et al., Nano Lett. **12**, 4172, (2012).

[17] P. Das and T. K. Chini, J. Phys. Chem. C. **116**, 25969-25976, (2012).

[18] A. Maiti, A. Maity and T. K. Chini, J. Phys. Chem. C. **119**, 18537-18545, (2015).

[19] P. Das, A. Kedia, P. S. Kumar, N. Large and T. K. Chini, Nanotechnology. **24**, 405704 (2013).

[20] R. M. Bakker, A. Boltasseva, Z. Liu, R. H. Pedersen, S. Gresillon, A. V. Kildishev, V. P. Drachev, V. M. Shalaev, Opt. Express. **15**, 13682-13688, (2007).

[21] M. Rang, A. C. Jones, F. Zhou, Z-Y. Li, B. J. Wiley, Y. Xia, M. B Raschke, Nano Lett. **8**, 3357-3363, (2008).

[22] N. Yamamoto, K. Araya, and F. J. García de Abajo, Phys. Rev. B: Condens. Matter Mater. Phys. **64**, 205419, (2001).

[23] K. Suenaga, M. Tence, C. Mory, C. Colliex, H. Kato, T. Okazaki, H. Shinohara, K. Hirahara, S. Bandow, S. Iijima, Science. **290**, 2280-2282, (2000).

[24] A. Losquin and M. Kociak, ACS Photonics. **2**, 1619-1627, (2015).

List of Figures

Chapter 1

General introduction

This chapter describes a broad overview of optical properties of the metal nanoparticles and its' potential applications. Important highlights in the history of the field of metal nanoparticles, the basic principles of plasmon resonances as well as the advantage of using the spectroscopic techniques like Cathodoluminescence (CL) and surface-enhanced Raman scattering (SERS) to probe the plasmonic properties of the metal nanoparticles are also included.

1.1 Introduction

The phenomenon resulting from the interaction of visible light with metal nanoparticles (MNPs) has painted its contributory mark in history of mankind and civilization from the ancient age. The earliest engineered nanoparticles are often attributed to the ancient Romans, Egyptians, and Chinese. Despite not having any scientific ideas of what they were making, they were successfully able to prepare nanoparticle solutions of gold and other precious metals with reasonably control over particle size and composition. These antiquarian nanoparticle solutions were famous for lustre decorations due to its' optical behavior and often used in making stained glass paint arts (Figure 1.1(a)), other luxurious Roman crafts like the "Lycurgus Cup" (Figure 1.1(b) and (c))etc. Although the observations and evidences of the interaction of light and MNPs were available throughout its thousand-year old history, the scientific origin of such colorful behavior was completely unknown. However, it takes many centuries to know the underlying science of the coloration of stained glass paints which is nothing but the absorption and scattering phenomenon of visible light in presence of colloidal MNPs. The colorful optical properties of colloidal gold solutions were partly explained by Michael Faraday in 1847 [1–3] calling the solution "a beautiful ruby fluid" (Figure 1.2), and noting that "a mere variation in the size of particles gave rise to a variety of resultant colours". The world would have to wait more than half a century before detailed experimental results were published for plasmons living on the surface of a MNP,[4, 5] though an understanding of the electromagnetic response of a perfect sphere with a given dielectric function had existed following the explanation given by Gustav Mie in 1908.[6] Such combination of detailed experimental as well as

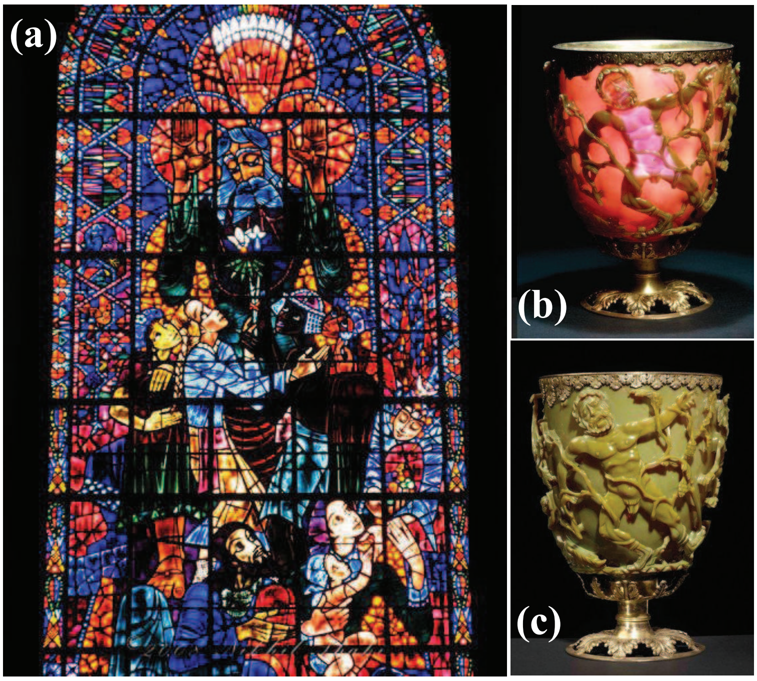

Figure 1.1: *(a) Surface plasmon effects can be seen in the stained glass of some medieval cathedrals. The Lycurgus cup contains plasmon-supporting silver and gold nanoparticles that cause it to appear (b) red in transmission and (c) green in reflection. Image courtesy: (a) Canterbury Cathedral (http://sew-graceful.blogspot.in). (b) and (c) Trustees of the British Museum (http://www.ibtimes.co.uk)*

theoretical explanations not only solved the century-old mystery about the color of the stained glass but also have given birth to a new field in nanoscience which has established that the optical properties of MNPs are basically caused by the collective excitation of the conduction electrons in a MNP known as "plasmons". In case of noble metal nanoparticles, when an electromagnetic (EM) radiation is incident on the nanoparticle, its surface electron cloud oscillates coherently relative to a lattice of positive ions, due to the alternating field of the incident radiation that also leads to a surface charge distribution. Now such collective oscillation associated with different surface charge distribution is known as surface plasmons (SPs).

Figure 1.2: *Michael Faraday's colloid, a suspension of gold nanoparticles in a liquid. Image courtesy: Paul Wilkinson/Royal Institution*

Qualitatively there are two types of surface plasmon: (a) surface plasmon polaritons (SPPs) which is propagating in nature and (b) localized surface plasmons (LSPs) which is localised in nature. Just as water ripples travel along the surface of a pond after a stone is thrown into it, collective oscillations of conduction electrons called surface plasmon polaritons (SPPs) can be made to propagate along the interface between a dielectric and metal (Figure 1.3(a)) by any external EM wave.[7–10] On the contrary, LSP is completely localised within the surface of the nanoparticle (Figure 1.3(b)). However, the optical frequency excitations of both type of surface plasmons in nanostructures have drawn an intense attention in research interest in the past decade for its' potential use in photovoltaic,[10–12] chemical sensing,[13] surface enhanced Raman scattering (SERS),[14, 15] ultramicroscopy,[8, 11, 16] medicine,[17, 18] and many other applications.

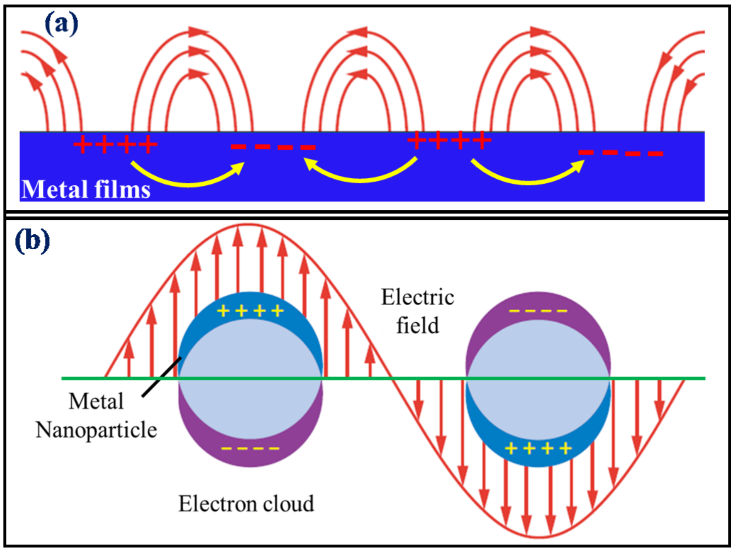

Figure 1.3: *Schematic of (a) propagating surface plasmons of a metal surface and (b) localized surface plasmons (LSPs) of a metal nanosphere.*

1.2 Motivation

1.2.1 Localised surface plasmon resonance properties of metal nanoparticle

Much attention has been paid in recent years to control and manipulate light [19, 20] using MNPs. The basic physical concept discussed mostly in this connection is the idea of the so-called localized surface plasmons (LSPs), which are non propagating excitations of the conduction electrons in MNPs. LSPs in small MNP, mostly act like the surface charge density waves. With analogy, as the note sounded by a bell entirely depends on its shape, size as well as the material because acoustic waves are confined at its surface, the optical properties of an MNP depends on its shape, size and material because of LSP confinement at its surface. Similarly, as acoustic energy density in a bell concentrates at antinodes of acoustic waves, LSP energy density concentrates at antinodes of LSP waves in small volumes close to the surface of the MNP.[21] LSP when excited resonantly with a particular wavelength of the exciting light or evanescent wave associated with fast-moving electrons, shows considerable enhancement of the far-field intensity and similar enhancement of the near-field at the surface of the MNP,[7, 8, 11, 21] especially localized in the regions of sharp edges,[22–25] corners,[26–28] tips,[29–31] and apex,[26, 27] depending on the morphology of the nanoparticles. The regions characterized by highly localized and strongly enhanced EM fields, known as plasmonic “hot spots”,[32] are responsible for large enhancements in surface enhanced Raman scattering (SERS) signals and have several interesting effects, such as enhanced fluorescence [33] or enhanced photo carrier generation,[11, 34] that can have potential applications in biosensing,[13, 35, 36] and single molecule detection.[14, 37, 38]

1.2.2 Importance of complex shaped gold (Au) nanoparticles

The localized surface plasmon resonance (LSPR) greatly relies on the dielectric property of the constitute material of MNPs. As an example, silver (Ag) nanoparticles are the most studied in the literature due to its huge application in a number of scientific areas and applications.[39] The strong oxidation affects the resonances condintion down to 350 nm for Ag NPs that degrades plasmonic properties over time rapidly. Copper NPs are also known as the promising candidate for plasmonic studies due to their natural abundance, low cost and good conductivity. Unfortunately the oxidation process again degrades the LSPR properties of Cu nanoparticles forming the Cu_2O and CuO.[40] In contrast, Gold (Au) is

often chosen because of its chemical stability, resistance to oxidation and biocompatibility. Au NPs have drawn much attention in biomedical applications including labeling and biosensing owing to its fascinating features such as ease of synthesis and and non-cytotoxicity.[41, 42] The functionalization processes of Au NPs with with biomolecules open a new way in biomedical applications including contrast agents,[43] drug delivery vectors,[44] localized heat therapy,[44–46] and ultra-sensitive biomarkers.[47] In case of Au NPs the LSPR properties mainly occur at visible region which has a very important implications in surface-enhanced spectroscopies,[8, 40, 48] sub-wavelength optics,[49] and bio-photonics.[50, 51]
Au NPs having simple geometry like rod,[52, 53] triangle,[36] sphere,[54] disk,[55], wedge [56] etc. have been used extensively in NP based plasmonic applications since last few decades. Besides, the complex shaped NPs also offer an intense attention owing to their fascinating and strong nonlinear optical phenomenon. Moreover nanoparticle with complex morphology having tipped surface features such as surface-textured nanospheres,[57–59] nanopolyhedra,[28, 58, 60] multibranched nanostars,[29–31, 61–63] are favorable for possessing multiple hot spots that also shows remarkable applications in sensing, imaging and surface enhanced Raman scattering (SERS).[58, 64–67] In a few recent literature it has been shown that that Au nanoparticles of more complex geometries enclosed by various high-index facets, which might have applications in catalytic activities.[68–70] In this context, multitipped (also called multipod, nanostar, or nanoflower) MNPs, especially, gold nanostars/nanoflowers [29–31, 61–63] are an exciting new class of plasmonic structures. Gold nanoflowers (AuNFs) consist of a near-spherical core from which

numerous sharp tips of different lengths point outward. The significant tunability of the localized surface plasmon resonance (LSPR) wavelength over a wide range (from visible to NIR regime of the spectrum) and the corresponding strong electromagnetic (EM) field enhancement near apex of the tips have been utilized in many fields including detection and diagnosis of cancer affected cells,[71] plasmon enhanced microscopy such as surface-enhanced Raman scattering,[64, 72, 73] photoelectron emission,[32] and photoluminescence [74] studies. Apart from it, another new class of Au nanostructure, namely, trisoctahedral (TOH), which is a polyhedron bounded by 24 exposed high-index facets with Miller indices of $\{hkl\}$ $(h > l)$, has drawn much attention [75–80] because of its' superior catalytic [68–70] and SERS activities [58, 68] caused by the presence of high density of atomic steps and dangling bonds on the high-index facets.

1.2.3 Surface enhanced Raman scattering (SERS)

Since the first observations of the Raman spectra of pyridine on roughened silver were made in 1974,[81] SERS has been used extensively as a signal transduction mechanism in real-world sensor applications and state-of-the-art surface science in the past two decades. SERS has also been implemented for trace analyzing of pesticides,[82] anthrax,[83] and nuclear waste [84] as well as identification of bacteria,[85] genetic diagnostics,[86] and immunoassay labeling.[87, 88] Additionally the recent advancement in spectroscopic instrumentation, nanofabrication methods, theoretical modeling, and novel detection schemes has established the SERS technics as a powerful analytical tool.

Since the discovery of the phenomenon, the mechanism of SERS enhancement remains an active research topic. The powerful vibrational spectroscopy technique is mainly governed by the amplification of EM fields generated through the excitation of LSP of the SERS substrate.[89, 90] The SERS activity crucially depends on LSP properties of MNPs on selected substrate. The Au MNPs are most commonly used for SERS activity, in the form of colloidal solution, as well as, solid substrates because of their unique optical properties. The three major factors involved in the Raman enhancement by MNPs are the size, shape and relative position of the NPs. Moreover, the particles having sharp surface curvatures [58, 68, 91] and tips [65, 67, 92] may provide multiple hotspots at their surface curvatures, sharp tips and also at the junction between two or more NPs. In this context, the particles having sharp surface curvatures and tips like nanoprism,[22, 23, 93] nanorod,[25] nanodecahedra,[26, 27, 94] and nanostar/flower [29, 30] are exploited extensively owing to the strong localization of the EM fields at their sharp corners or tips. Therefore, it is highly demanding to understand the LSP properties of individual MNPs of different size and shape while using them for SERS activity, in the form ensemble MNPs on solid substrates.

1.3 Study of single particle LSPR properties with electron beam based CL spectroscopy and imaging in SEM

Single particle approaches have shown to be a powerful tool in fundamental studies and are gaining momentum as part of devices and sensing technology owing to their multiplexing capabilities and small sensing volume.[95] The single particle studies are most powerful technique that has enough ability to explore or reveal properties of nanoparticle at single level which is often overlooked or neglected or mixed in the ensemble measurements. Ensemble measurements always provide an average signal from all the particles of all different shapes and sizes that also washes out individual information about the environmental effect on each particle. Consequently, optical techniques like UV-VIS spectroscopy probe ensembles of NPs and are suffered by large inhomogeneous broadening due to the diversity of particles and conditions. Even single particle spectroscopy technique like dark field microscopy (DFM),[96, 97] a light source excites the whole volume of the nanoparticle and therefore unable to probe the rich features arising out from the different parts of the highly complex shaped nanostructures like nanostar/flower and trisoctahedron. Other well adapted techniques to probe LSPRs at the single NP level are photon scanning tunneling microscopy,[98] scanning near-field optical microscopy (SNOM),[99] and apertureless SNOM.[100] These techniques achieve better spatial resolution but often require fabrication of very delicate probe in the form of a nanoscale sharp tip and may suffer from probe-sample interactions distorting the signal of interest.

An excellent alternative is electron microscopy based techniques, i.e. electron energy loss spectroscopy (EELS),[22, 26, 31, 101, 102] and cathodoluminescence (CL) spectroscopy.[23–25, 27, 30, 103–106] The high spatial resolution of about 1 nm or better for such techniques [22, 26, 107] is mainly governed by the ability of a modern scanning or transmission electron microscope (SEM or TEM) to focus an electron beam down to a diameter of 1 nm or below. The excitation mechanism of LSP modes with an electron beam is quite different from that of the optical excitation. An electron, or a beam of electrons, moving in vacuum can act as an evanescent source of super-continuum light.[8] A finely focused electron beam can act as a local probe to excite plasmons selectively.

The working principle of CL-SEM is that, energy is coupled from energetic electrons to the plasmon modes of the metallic nanostructure and subsequently to the propagating light modes that constitute one of the prominent decay channels for plasmons and causes enhancement in near field as well as the far-field intensity. Mapping the spatial variation of the photon emission is a direct probe of resonant modes of plasmonic nanostructures and, consequently, provides a direct way to map the local electric fields.

1.4 FDTD-based electrodynamic calculations for metal nanoplasmonics

The surface plasmonic property of MNP is nothing but the interaction between incoming EM wave attached with incoming light beam or electron beam and the plasmon wave attached with the MNP. Consequently surface plasmons can be described by classical electromagnetic theory, i.e. Maxwells equations, when the electron mean free path in the metal (at room temperature typically $\sim$ 20 nm for Au and $\sim$ 38 nm for Ag metals respectively) is much shorter than the plasmon wavelength. In 1908, Gustav Mie gave a quantitative explanation of the size dependent optical properties of metal nano spheres approaching the analytical solution of EM waves.[6] Unfortunately Mie theory is only applicable to very simple isotropic geometry like sphere or infinite cylinder. In contrast, numerical simulations are capable of solving the Maxwell's equations in any anisotropic and arbitrarily shaped metal NPs including the complex shaped nanogeometries like nanostar, nano TOH etc. The numerical simulation of Maxwell's equation for complex objects was first introduced by Purcell and Pennypacker using Discrete Dipole Approximation (DDA).[108] However in past few decades many new computational tools, such as the finite difference time domain method (FDTD),[62, 109, 110] the boundary element method (BEM) [111, 112] and finite element method (FEM) [113] are introduced to understand the responses of small metal NPs to light or electron beam. Among several numerical methods, FDTD method has drawn rich attention to study the LSP properties of nanosystems due to simple parametrization, simple implementation and time consuming.

1.5 Seed mediated wet chemical synthesis

It is very well known fact that the shape manipulation of a plasmonic nanoparticle represents the most powerful means of tailoring and fine-tuning its LSPR properties as the frequency and amplitude of the resonance are sensitive to particle shape, which determines how the free electrons are polarized and distributed on the surface. During the past decade, several types of chemical methods have been established for preparing high-quality complex shaped Au nanoparticles,[114, 115] enabling a systematic study of LSPR dependencies on the size, shape, and structure (solid versus hollow) of MNPs. Among several synthesis procedures, seed-mediated wet chemical synthesis method has been widely applied in the synthesis of metal nanoparticles because of the facility of the synthetic process and the high yield of the products. The seed-mediated synthesis of Au particles can be divided into two main synthetic steps: (1) preperation of highly monodisperse spherical Au seeds, and (2) the growth of larger nanoparticles by slowly reducing additional Au onto the previously synthesized seeds. The seeds are used as the center of the nucleation process in growth phase of the NP formations which helps to maintain monodispersity in the final nanoparticle colloid.[75] Here seed mediated protocol have been used the to synthesize both the Au nanostar/nanoflower and Au TOH shaped NPs.

1.6 The outline of the thesis

This thesis is concerned with synthesis and optical characterization of complex shaped Au MNPs. The seed mediated wet chemical protocol has been employed for synthesizing Au complex shaped NPs. Next the transmission electron microscopy and related technique have been used to confirm the crystalline structure and purity of the synthesized Au NPs. The plasmonic properties of these NPs are characterized using cathodoluminescence (CL) technique in a high resolution scanning electron microscope (HRSEM) and surface enhanced Raman scattering (SERS) technique. Finally the experimentally acquired studies have been analyzed with 3D-FDTD numerical simulations. Following this introductory chapter, this thesis consists of six chapters.

Chapter 2 deals with the details of the chemical synthesis protocols to synthesize complex shaped Au NPs. The details of the CL setup in HRSEM, which is the primary characterization tool throughout this thesis have also been described. Moreover the basic principles of other experimental techniques used in characterization are briefly discussed along with the actual instrumental configurations.

Chapter 3 explores the basic relationship between SP studies and CL technique. In the latter part of the chapter, the implementation of FDTD numerical approach has been discussed.

Chapter 4 discusses the effect of intertip coupling on the plasmonic behavior of individual multitipped Au nanoflower.

Chapter 5 demonstrates the ideas about probing localized surface plasmons of TOH Au NPs for surface enhanced Raman scattering.

Finally in **Chapter 6** a summary of the thesis has been presented.

Chapter 2

Experimental methods

This chapter describes chemical routes to synthesize MNPs, the CL-SEM instrument that is used as a main optical characterization tool throughout the thesis and the basic principles of several characterization tools relevant to this thesis.

2.1 Introduction

A brief description of the synthesis of complex shaped Au NF and TOH NPs and the experimental techniques for their morphological, elemental, structural and plasmon driven optical studies are discussed in this chapter. Nanoparticles were syntheiszed using seed mediated wet chemical processes. Both the electron microscopy techniques namely field emission (FE) based scanning electron microscope (SEM) and transmission electron microscope (TEM) were used for morphological and structural studies of the as synthesized NPs. Study of the compositional details has been carried out using energy dispersive x-ray spectrometry (EDS) in TEM. Finally the investigation of localized surface plasmon enhanced optical properties of the NPs were studied using CL and Raman techniques.

2.2 Seed mediated wet chemical synthesis

2.2.1 Synthesis of Au nanoflower

2.2.1.1 Chemicals

Chemicals including Gold (III) chloride trihydrate ($HAuCl_4{\cdot}3H_2O$) $\geq$99.9% trace metal basis, Silver nitrate ($AgNO_3$) BioXtra $\geq$99% (titration), Sodium borohydride (H_4BNa) granular, 10-40 mesh 98%, L-Ascorbic acid ($C_6H_8O_6$) ACS reagent $\geq$99%, and Hexadecyltrimethyl ammonium bromide or CTAB ($C_{19}H_{42}BrN$) assay $\geq$99% (AT) were purchased from Sigma-Aldrich (Germany) and used for the synthesis without any further purification. All the synthesis and experimental works have been done by using Milli-Q water.

Gold nanoflowers (GNFs) are synthesized by using multi step seeding-based nanotemplating method [67] where the final step seed is a nano template for pre determined tailored shape. In the first step, we synthesize spherical gold nano-seed by adding 0.5 mL of 10^{-2} M $HAuCl_4$ solution with 20 mL water in a small vial. Next 0.2 mL of 2.5×10^{-2} M trisodium citrate ($Na_3C_6H_5O_7$) solution was added drop wise and left for 1 min to mix well. After that 60 μL of 10^{-1} M ice cold freshly prepared $NaBH_4$ solution is added drop by drop which changes the color of solution from light yellow to light red. We keep this seed solution for another 2 hrs before using it for the next synthesis step. During this time, the colour of the solution turns to deep red.

2.2.1.2 First growth step to synthesize gold nano popcorns (GNPops)

In the first growth step, we have synthesized mono dispersed GNPops with average size of about 45 ± 3 nm. To synthesize GNPops, we dissolve 0.049 gm of CTAB in 45 mL water (2.8×10^{-3} M) by mild heating and simultaneous constant slow stirring. To this solution, 2 mL of 10^{-2} M $HAuCl_4$ solution is added and stirred for additional 1 min. Then 300 μL of 10^{-2} M freshly prepared $AgNO_3$ solution is added gently, mixed well and then 320 μL of 10^{-1} M ascorbic acid is added drop wise. As soon as the solution becomes colourless, 500 μL of gold nanoseed solution (as prepared) is added at a time. The solution becomes deep blue within a minute and it is left still for 2 hrs before using it for the next synthesis step.

2.2.1.3 Nano-templating step to synthesize GNFs

In the second growth step we have synthesized intrinsically mono dispersed GNFs with size (diameter) variation between 110-360 nm. To synthesize different sized

GNFs with differential petal openings, we used 11 different growth solutions by dissolving 0.005, 0.01, 0.025, 0.05, 0.1, 0.25, 0.5, 0.75, 1.0, 1.25 and 1.5 gm of CTAB in 45 mL water by mild heating and constant stirring. To this solution 2 mL of 10^{-2} M $HAuCl_4$ solution was added and stirred for additional 1 min. Then 300 μL of 10^{-2} M freshly prepared $AgNO_3$ solution was added gently, mixed well and then 320 μL of 10^{-1} M ascorbic acid is added drop wise. As the solution becomes colorless, immediately 500 μL of GNPop solution was added at a time as nano-template and the solution is left undisturbed for overnight to complete the growth process and different growth solutions show different bright color. The diluted Au NF solution is drop coated on a cleaned Si (100) wafer and then loaded into the SEM chamber after sufficient drying in ambient condition.

2.2.2 Synthesis of Au nano TOH particle

A seed mediated growth method was used to synthesize the TOH Au particles.[58, 59] Chemicals including gold (III) chloride trihydrate ($HAuCl_4.3H_2O$)$\geq$ 99.9%, sodium borohydride ($NaBH_4 \geq 99\%$) granular, 98%, L-ascorbic acid ($C_6H_8O_6$) ACS reagent $\geq$ 99%, were obtained from Sigma-Aldrich. (1Hexadecyl) trimethylammonium chloride (CTAC, 96%) was obtained from Alfa Aesar. The Milli-Q water was used throughout the synthesis works. At first, an ice cold freshly prepared solution of 0.30 mL, 10 mM $NaBH_4$ was quickly injected into a solution composed of 10.00 mL, 0.10 M CTAC, and 0.25 mL, 10 mM $HAuCl_4$ under magnetic stirring (1200 rpm) for colloidal Au seeds preparation. Next, this as-prepared seed solution was diluted 1000 folds with CTAC (0.10 M) solution which was further used for the seed mediated growth technique. Then, the growth solution was prepared by sequentially adding $HAuCl_4$ (0.50 mL, 10 mM) and L-ascorbic acid

(1.0 mL, 0.10 M) into a CTAC (10.00 mL, 0.10 M) solution. Finally, 0.01 mL of the diluted Au seed solution was added to the growth solution and the solution was left undisturbed for overnight to complete the growth process of the TOH Au particles.

As-synthesized TOH shaped Au particles were drop-casted on a mirror-polished side of a piece of cleaned crystalline silicon (Si) substrate for morphological analysis using a FESEM (Zeiss, SUPRA 40). A carbon coated 3 mm grid was dipped within the growth solution and was dried for sufficient long time before inserting it in analysis chamber of TEM for structure investigation using a high resolution transmission electron microscope (HRTEM; FEI, Tecnai G2 F30, S-Twin) operating at 300 kV.

2.3 Characterization tools

Throughout this thesis, field emission scanning electron microscope (FESEM) based cathodoluminscence (CL) technique has been used extensively as the major characterization tool for LSPR studies. The surface enhanced Raman scattering (SERS) studies are partly carried out to demonstrate the significance of field enhancement under LSPR conditions in Au MNPs. In this section the basic description and operation of the characterizing tools shall be discussed.

2.3.1 Scanning electron microscope (SEM)

A Scanning Electron Microscope (SEM) is a powerful magnification tool that utilizes focused beams of electrons to obtain details of morphological information. Typically, SEM is capable of imaging a surface by sweeping a finely focussed electron beam in a raster pattern over an area of sample surface and by detecting secondary electrons emitted from the surface within a high vacuum ambience. The schematic of main components of a SEM is shown in Figure 2.1. These are

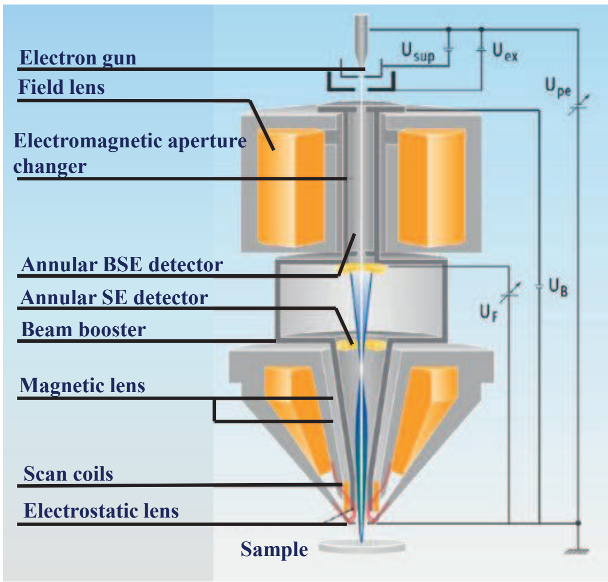

Figure 2.1: *Schematic of FESEM.Here the extractor voltage of first anode, primary beam voltage, booster voltage and filtering grid voltage are designated as* U_{ex}*,* U_{PE}*, UB, UF and EsB respectively. Image courtesy: www.smt.zeiss.com*

electron gun, field lens, electromagnetic aperture changer, magnetic lens, scanning coils, electrostatic lens and detectors. The high energetic electron beam from the field emission gun (FEG) filament reaches to the sample through a of series of lenses (condenser and objective) as well as series of micron size apertures. The FEG cathode contains a sharp metal tip with radius nearly about 100 nm. The typical beam diameter for FEGs is on the order of few nanometers that enables imaging with high spatial resolution. Resolving small specimen features requires probe diameters of similar dimensions. Lenses are used to control the diameter of the beam as well as to focus the beam on the sample. Spacial care must be taken in sample preparation as the the SEM utilizes vacuum conditions. To prevent the charging effect of the samples the samples must be conductive in nature and free from water. Otherwise it will hamper the vacuum facility as well as the imaging quality. All non-metals need to be made conductive by coating the sample with a thin layer of conductive material. The chamber pressure is maintained below 1×10^{-5} mbar by a turbo pump backed by a rotary pump having oil trap and oil mist filter that guarantees contamination free vacuum environment. The field emission gun (FEG) was kept at ultra high vacuum UHV (pressure level 10^{-10} mbar) by an ion pump (nominal pumping speed for dry N_2 is 53 l/s).

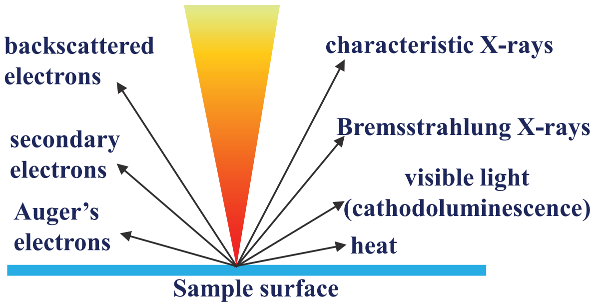

Figure 2.2: *Types of interactions between electrons and a sample.*

Interaction of high energetic electron beam with sample gives rise to different kind of signals through electron-sample interactions as shown in Figure 2.2.The resulting region over which the incident electrons interact with the sample is known as interaction volume. The interaction volume increases with increasing incident beam energy and decreases with increasing average atomic number of the specimen. Secondary electrons and backscattered electrons are commonly used for imaging the surface morphology and topography of the samples. The typical escape depth of the low-energy (<50 eV) secondary electrons is approximately 5-50 nm whereas the backscattered electrons (energy varies from zero to incident electron energy) can escape from 100 times larger depth compared to the secondary electrons. Consequently, SEs are very sensitive to topography of the surface. Besides, the X-ray generation is produced by inelastic collisions of the incident electrons with electrons in discrete ortitals (shells) of atoms in the sample. The emitted photons (characteristic X-rays) are used for quantitative and semiquantitative analyses of elemental analysis. Depending on the detection of different kind of emitted signals, different aspects of electron-solid interaction based characterization of materials are possible, which is an unique feature of electron microscopes (SEM and TEM).

2.3.2 Cathodoluminescence (CL) in a SEM

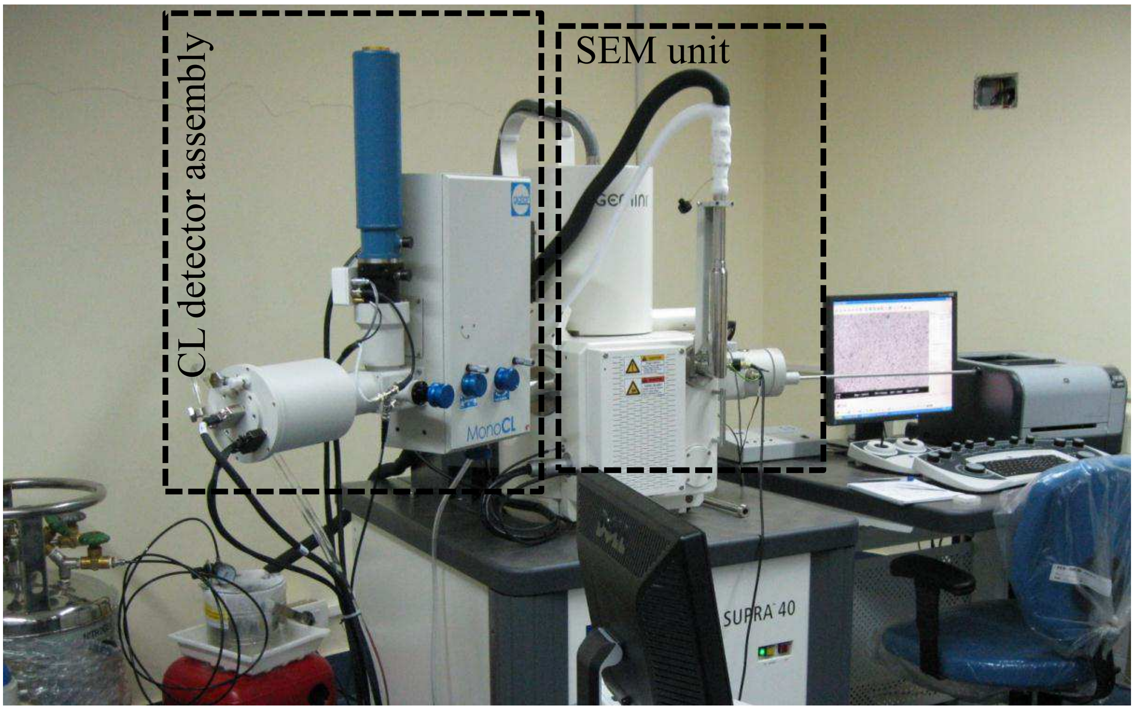

Figure 2.3: *Photograph of the CL-SEM system installed at the Saha Institute of Nuclear Physics, Kolkata.*

The CL-SEM facility, described here, was designed at the Saha Institute of Nuclear Physics (SINP), Kolkata and was custom fabricated by Carl Zeiss, Germany and Gatan, UK. The CL-SEM facility has two units; a probe forming unit that delivers few nanometer size focused electron beam (ZEISS SUPRA40 field emission gun (FEG) SEM) and an optical detection unit (MonoCL3, Gatan) (shown in Figure 2.3).[116] The schematic of the CL-SEM system is shown in Figure 2.4.

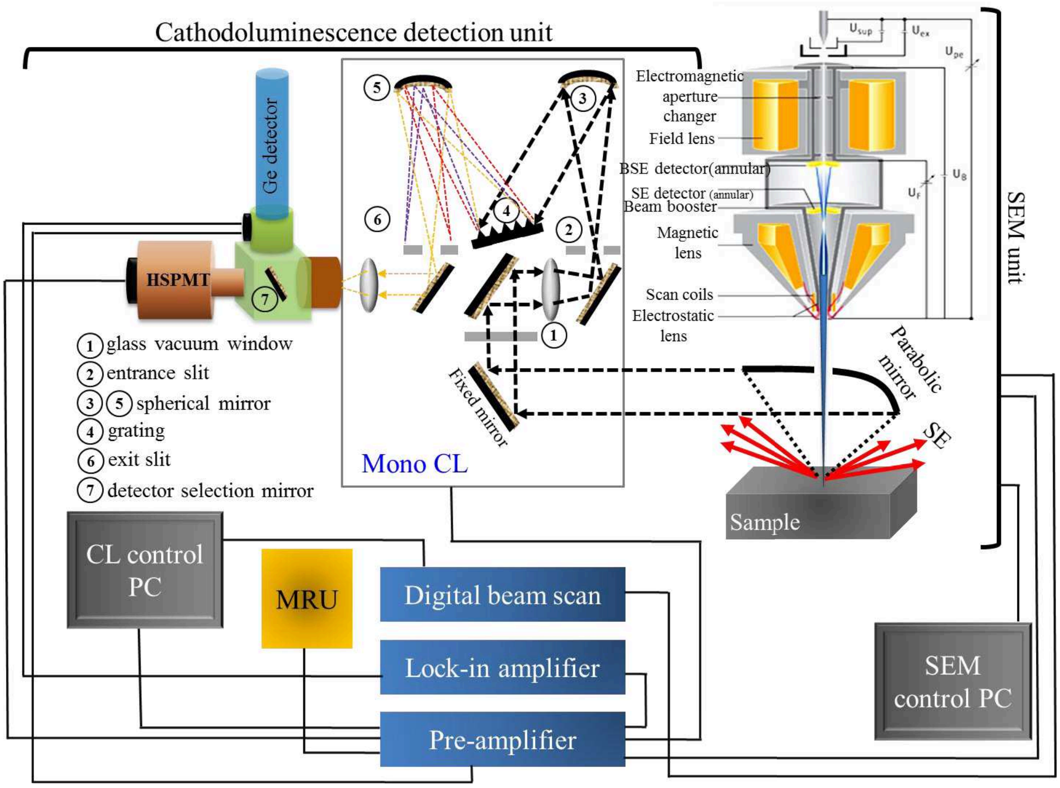

Figure 2.4: *Schematic diagram of the CL-SEM system.*

The MonoCL3 system is equipped with a retractable paraboloid mirror placed inside the SEM chamber. The electron beam (e-beam) from the FEG of the SEM reaches the sample through a hole of 1 mm diameter on the paraboloid mirror. The mirror is capable of collecting emitted light signals from the sample under consideration within a solid angle of 1.42π sr of the full 2π of the upper half sphere. The collected light signal is collimated through a hollow aluminum tube and directed to a Czerny-Turner type optical monochromator of focal length of 300 mm. Finally the signal from the monochromator is fed to a Peltier-cooled high sensitivity photo multiplier tube (HSPMT). In order to capture maximum amount of light signal, top surface of the sample must be kept at the focal plane of the paraboloid mirror. In our experimental arrangements this is achieved by putting the sample top surface 1 mm below the bottom plane of the mirror. This focal adjustment (shown in Figure 2.5) is very carefully done before every set of experiments and the detailed procedure can be found elsewhere.[116] The system was calibrated before every set of experiments using 404.66 nm mercury spectral line of an in line discharge lamp

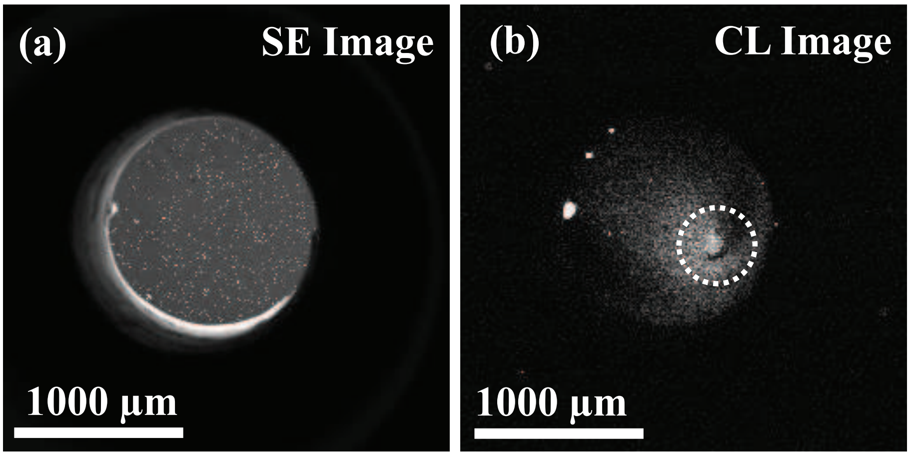

Figure 2.5: *(a) SE image at the lowest possible magnification of the SEM. The circular hole is the aperture of the mirror (1 mm diameter). Beneath this is the specimen under consideration. (b) Panchromatic CL image after height adjustment between the mirror and sample surface using the stepper motor controlled sample stage with utmost care. The brightest zone encircled by white dots is the focal position of the specimen commonly called as hot spot.*

for better accuracy in data collection from the sample (shown in Figure 2.6). The

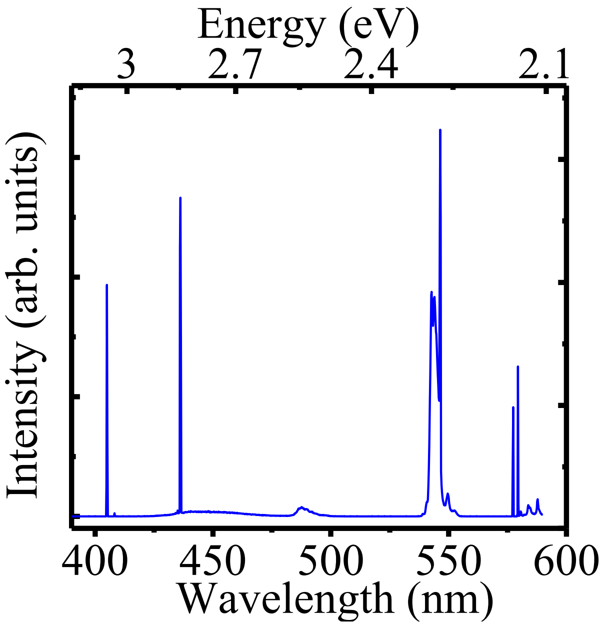

Figure 2.6: *Calibration lamp spectra with entrance and exit slit width of 100 μm*

CL system can be operated in two modes, namely, monochromatic and panchromatic. In the monochromatic mode, the electron beam is either scanned over an area of interest (area analysis) or fixed onto a selected point (spot analysis) of the sample. The photons emitted from the sample pass through the monochromator and enter the HSPMT detector and the recording of CL spectra is accomplished. Then monochromatic CL images or photon maps at selected peak wavelengths are obtained by scanning the electron beam over the sample while allowing only the light signal of desired wavelength to pass through the monochromator to the HSPMT. In the panchromatic mode, the monochromator is bypassed and the emitted light is directly fed to the HSPMT detector resulting in a CL emission map that contains all the wavelengths lying within the detection range (300 nm-900 nm) of the HSPMT. Both the monochromatic and panchromatic mode of CL operation also allow us simultaneous acquisition of secondary electron (SE) images enabling direct correlation between plasmonic response and the particle morphology.

2.3.3 Raman spectroscopy

Figure 2.7: *Photograph of the micro-Raman spectrometer.*

Raman spectroscopy is a vibrational spectroscopy involving the inelastic scattering of incident photons by a molecule. The Raman effect results from the change in polarizability of the molecule induced by the interaction of vibrational and/or rotational motions of molecules with the electromagnetic radiation. When a monochromatic light (at frequency ν_0) illuminates molecules with internal modes of vibration most of the scattering occurs at the same frequency as the incident source which is termed as Rayleigh scattering. Besides, a very small portion of the incident light is scattered off from the molecules with a shifted frequency (either red or blue shifted from ν_0 to ν_0'). The frequency difference between the incident light and the scattered light equals to the molecular vibrational frequency ($\Delta\nu$),

$$\nu_0 \pm \nu_0' = \Delta\nu \tag{2.1}$$

This phenomenon is referred to as Raman effect. A typical Raman spectrum will contain multiple Raman peaks depending on the number of vibrational mode modes for the molecule. The $\nu_0 - \nu_0'$ (red shifted) and $\nu_0 + \nu_0'$ (blue shifted)lines are known as Stokes and anti-Stokes lines. corresponding to a specific vibrational. The intensities of the anti-Stokes peaks are smaller than those for the Stokes peaks. Raman scattering is generally considered to be a very weak scattering process (approximately 10^6-10^8 scattering events are required to generate one Raman scattered photon).[117] In Raman spectroscopy, the vibrational frequency (ν_0') are measured as a shift from the incident beam frequency (ν_0). The Raman shift can be expressed as

$$\Delta\nu = (\frac{1}{\lambda_{incident}})(\frac{1}{\lambda_{scattered}})cm^{-1} \tag{2.2}$$

The collected Raman scattering intensity in spectrometer can be expressed as

$$I_s = (\frac{8\pi^4\alpha^2}{\lambda^4 r^2})(1+\cos^2\theta)I_0 \tag{2.3}$$

where α is polarizability of the molecule, λ is wavelength of the incident light, I_0 is incident intensity, θ is angle between incident and scattered light, and r is distance from center of scattering to detector. The Raman signal can be enhanced by increasing the electric field interacting with the few molecules. The field enchantment can be obtained by surface plasmons of metal nanoparticles when they are excited with laser light source under the LSPR condition. Considering certain assumptions in the experimental configuration, it is shown that the Raman intensity can be enhanced by a factor equal to the fourth power of the local field enhancement which is often referred as the $|E|^4$ approximation in SERS. [90]

Raman scattering studies were performed using micro-Raman spectrometer (in-

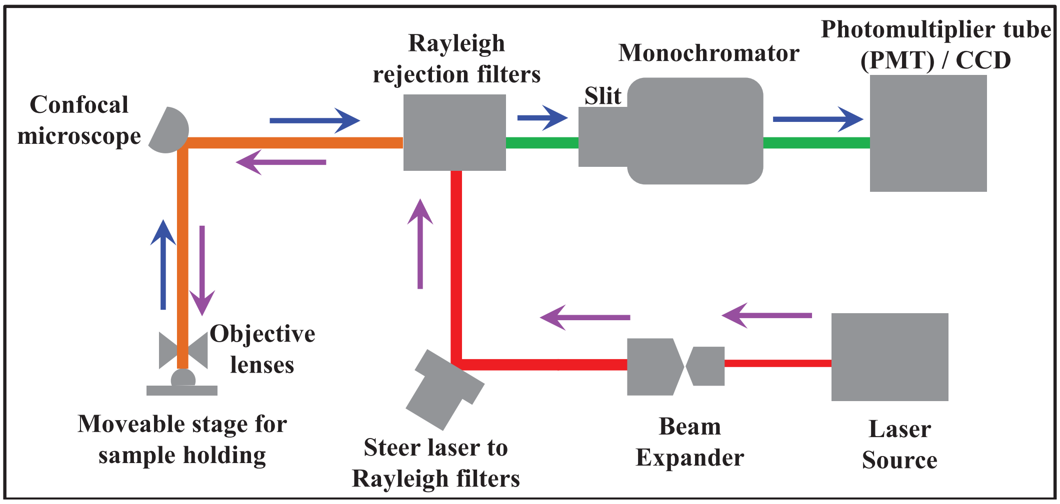

Figure 2.8: *Schematic of the micro-Raman spectrometer.*

Via, Renishaw) mounted in the back scattering configuration (shown in Figure 2.7). The Block diagram of the Raman setup with major parts are shown in Figure 2.8. The major parts of the Raman spectrometer are listed below:

1. Excitation source: Continuous wave lasers (Ar^+ laser with 514.5 nm).
2. Sample illumination and collection system: set of lenses or microscope (Backscattering configuration, standard and confocal mode, ×5, ×20, ×50, ×100, ×15 (UV), and ×40 (UV) lenses).
3. Notch/Edge filters: Rayleigh rejection filter.

4. Wavelength selector: Monochromator (Gratings; 600, 1800, 2400, and 3000 gr.mm^{-1}).

5. Detector and computer control/processing system: Thermoelectrically cooled CCD and InGaAs detectors.

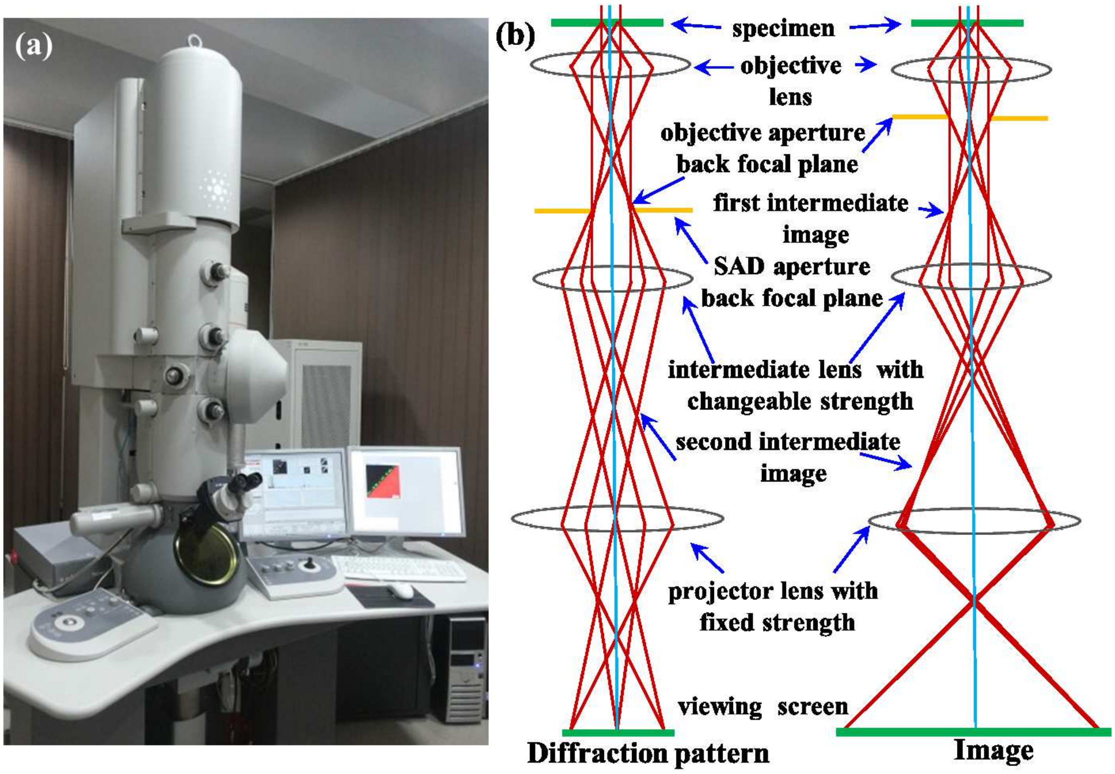

Figure 2.9: *(a) Photograph of the 300 kV high-resolution transmission electron microscope (HRTEM) system. (b) Schematic of TEM: For selected area electron diffraction (SAED), an aperture in the plane of the first intermediate image defines the region of which the diffraction is obtained. In imaging mode, an objective aperture can be inserted in the back focal plane to select one or more beams that contribute to the final image.*

2.3.4 Transmission elecron microscopy (TEM)

The high resolution crystalline analysis of as synthesized nanoparticles was carried out using a high resolution transmission electron microscope (HRTEM) (model: FEI, Technai G2 F30, S-Twin) operated at 300KV as shown in Figure 2.9a. The configuration of a transmission electron microscope (TEM) is shown schematically in Figure 2.9b. Electrons emerging from the electron gun are focused to a thin and almost parallel beam, by a pair of condenser lenses. The sample to be examined is placed at the object plane of the objective lens of the TEM. To obtain a clearly visible image on the phosphor screen, the sample is required to be electron transparent, i.e., thin enough, so that a large portion of the incident electron beam is transmitted through the sample. The transmitted portion of the electron beam is focused by the objective lens. An electron diffraction pattern formed at image plane, is magnified on the viewing screen by the first and second intermediate lens and the projector lens assembly. An area of interest can be selected from the sample image formed at first image plane by the selected area aperture. This selected area acts as a virtual source for the intermediate lens assembly so that only electron diffraction from this area can be observed in the viewing screen and is known as selected area diffraction imaging. In imaging mode of operation of the TEM, a spot from the electron diffraction pattern can be chosen for imaging by another aperture placed above the selected area electron diffraction (SAED) aperture which is called the objective aperture. To obtain an image of the sample, the first intermediate lens is adjusted so that the first image plane becomes its object plane. If the central spot on the optic axis is chosen for imaging by the objective aperture then the TEM image is called a bright field image. If any other diffraction spot is chosen for imaging then the image is called a dark field image.

2.3.5 X-Ray energy dispersive spectroscopy (XEDS)

X-Ray energy dispersive spectroscopy (XEDS) is a powerful technique which detects the X-rays generated from the interaction of the electron beam with the specimen (shown in Figure 2.2) and identifies from which element they originated with help of some electronics and computer display. EDS makes use of the X-ray spectrum emitted by a solid sample bombarded with a focused beam of electrons to obtain a localized chemical analysis. When the characteristic X-rays from different elements deposit energy to the XEDS detector, thousands of electron-hole pairs are generated, the number of which is directly proportional to energy of the X-rays. This X-ray spectrum comprises with element-specific-characteristic peaks with well-defined energies which provides the possibility to distinguish most elements in the periodic table. The XEDS analysis for compositional characteristic of the nanoparticles are performed with a EDS spectroscopy attached with the Technain G2 F30 S-Twin TEM machine used in the present work.

Chapter 3

Localised Surface plasmons and cathodoluinscence (CL): Basic concepts and numerical approaches

This chapter describes very briefly the physics of probing localized surface plasmons of metal nanoparticles by using the CL and SERS techniques.

3.1 Introduction

Recent interest in nanotechnology is driven by the unique and novel properties of noble metal nanoparticles (MNPs) interacting with incident electromagnetic (EM) field that results in localized surface plasmon resonances (LSPRs). These resonances, associated with MNPs, create sharp spectral absorption and scattering peaks as well as strong electromagnetic near-field enhancements. Plasmon physics is intriguing and its precise modelling proved to be challenging. However, the direct optical excitation of surface plasmons on MNPs provides numerous ways to control and manipulate light at nanoscale dimensions. This has stimulated the development of novel optical materials, deeper theoretical insight, innovative new devices, and applications with significant technological and societal impact. The subsequent sections of this chapter serve to describe the physical theory of LSPR formation at the surface of MNPs. Also, the theoretical concepts of probing localized surface plasmon using cathodoluminescence (CL) and surface enhanced Raman scattering (SERS) have been discussed.

3.2 Fundamentals of localized surface plasmon resonance (LSPR)

Localized surface plasmon resonance (LSPR) is an optical phenomena generated by the excitation of light or evanescent field of fast moving electron beam with conductive nanoparticles (NPs) that are smaller than the incident wavelength. As in surface plasmon resonance, the electric field of incident light can be deposited to collectively excite electrons of a conduction band, with the result being coherent localized plasmon oscillations with a resonant frequency that strongly depends on the composition, size, geometry, dielectric environment and separation distance of NPs. According to the Fermi liquid model, plasmons can be described as a negatively charged electron cloud coherently displaced from its equilibrium position around a lattice made of positively charged ions (as shown in Figure 3.1a).

Plasmons in NPs with size much smaller than photon wavelength are non-propagating excitations, called localized surface plasmons (LSPs), because the resulting plasmon oscillation is distributed over the whole particle volume.[48, 118, 119] Such a coherent displacement of electrons from the positively charged lattice generates a restoring force that pulls the polarized electrons back to the lattice, i.e. the NPs act much like a 'nanoantenna'.[120] Hence, the plasmon in an NP can be considered as a mass-spring harmonic oscillator driven by the external

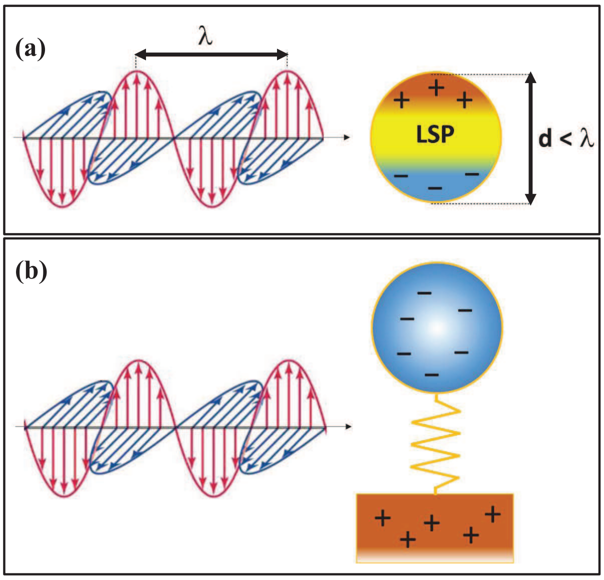

Figure 3.1: *(a) LSPs are excited by light propagating in free space or dielectric media. (b) The LSP in MNPs can be modelled, as a first approximation, like a spring-mass harmonic oscillator, where the free-electron density is the equivalent of the mass. Image adapted from Ref.[119]*

EM field, where the electron cloud oscillates like a simple dipole in parallel direction to the electric field of the electromagnetic radiation (Figure 3.1b).[9, 120–122] The simple mass-on-a-spring damped oscillator model, where the mass is represented by the electron density and the spring constant is set by the Coulomb restoring force between electrons and lattice atoms, has been utilized several times to gain conceptual and physical (semi-quantitative) understanding of plasmonic systems.[119–122] For instance, in the case of a spherical Au NP with size much smaller than the wavelength of light (quasistatic approximation), the distortion of the electron cloud in response to the electric field can be expressed by the metal polarizability:[3, 118, 119]

$$\alpha(\lambda) = 3\epsilon_m(\lambda)V_{NP}\frac{\epsilon(\lambda) - \epsilon_m(\lambda)}{\epsilon(\lambda) + \chi\epsilon_m(\lambda)} \tag{3.1}$$

where λ is the light wavelength, ϵ_m the dielectric constant of surrounding medium, V_{NP} the NP volume, χ is a geometrical factor ($\chi = 2$ in a sphere) and $\epsilon(\omega)$ is the frequency (ω) dependent complex dielectric function of the NP:[48, 119]

$$\epsilon(\omega) = Re[\epsilon(\omega)] + iIm[\epsilon(\omega)] \tag{3.2}$$

Using equation 3.1, one can arrive to the quasistatic expression of the extinction cross-section (σ_{Ext}) in a spherical Au NP:[48, 119, 123]

$$\sigma_{Ext} = \frac{18\pi[\epsilon_m(\lambda)]^{3/2}}{\lambda}V_{NP}\frac{Im\epsilon(\lambda)}{[Re[\epsilon] + 2\epsilon_m(\lambda)]^2 + Im[\epsilon(\lambda)]^2} \tag{3.3}$$

It is evident from equation 3.3 that:

1. the plasmonic properties of any material are defined by its $\epsilon(\omega)$;

2. σ_{Ext} scales with particle volume;

3. σ_{Ext} is maximum when the denominator is minimized, namely the LSP is excited at the frequency where:[3, 48, 118, 119]

$$Re[\epsilon_{NP}(\omega)] \sim \chi\epsilon_m(\omega). \tag{3.4}$$

This relationship is called the Fröhlich condition[48, 119] and the associated mode (in an oscillating field) the dipole surface plasmon of the MNP. Following the above discussion, we may conclude that the LSPR frequency strongly depends on the $\epsilon_m(\omega)$ of the surrounding medium. Moreover it is also strongly affected by NP size, shape, and composition.[3, 9, 48, 119] The imaginary part of the dielectric function also plays a role in the plasmon resonance, relating to the damping, that is, resonance peak broadening.[3, 48, 119]

3.3 Factors influencing LSPR

3.3.1 Dielectric environment

Clearly, the equation (3.4) implies that the LSPR frequency strongly depends on the $\epsilon_m(\omega)$ of the medium, i.e, it is redshifted for increasing $\epsilon_m(\omega)$ (i.e. going from water to glass) and blueshifted for decreasing $\epsilon_m(\omega)$ (i.e. going from water to air).[3, 48]

The LSPR frequency of MNP is also very sensitive to the environmental dielectric properties, such as changes in liquid or gas density, formation of organic shells such as those of stabilizing ligands, and in general to any surface adsorption of chemical compounds.

3.3.2 Size

We can express the extinction cross-section of a MNP as the sum of the absorption (σ_{Abs}) and scattering (σ_{Sca}) terms:

$$(\sigma_{Ext}) = (\sigma_{Sca}) + (\sigma_{Abs}) \tag{3.5}$$

It is very well known that for MNPs smaller than incident EM wavelength (λ), the scattering and absorption cross section depend on the 6th and 3rd power of the particles size (d), respectively.[3, 48, 119] Interestingly, the absorption dominates over scattering [48, 118, 119] when $d \ll \lambda$. However, both the effects become comparable for MNPs of about 50 nm, whereas scattering prevails above 70 - 100 nm. In fact, light scattering is an elastic process consisting in the modification of the photon propagation direction, whereas light absorption consists in the transfer of photon energy to the MNPs.

Interestingly, when the size of the MNP increases towards the wavelength of the incident EM wave, the multipolar plasmon modes come in the scenario due to the retardation effect. Typically such situations occur when the size parameter of the MNP (x) is very close to 1, where x is defined by:[123, 124]

$$x = \frac{\pi d}{\lambda} \tag{3.6}$$

In quasistatic approximation, $x \ll 1$, the size of MNP is very small compared to the incident light wavelength. Consequently the electric field distribution along the particle is essentially uniform, electron cloud polarization is coherent in each point of the metal, and dipolar plasmon oscillations are excited.[21, 48, 118] In contrast, the multipolar plamons modes are excited under resonant EM wavelength in case of larger MNP where neither the electric field distribution along the particle is uniform, nor the electron cloud polarization is coherent. The size effect is a bare electromagnetic phenomenon appearing in the optical absorption spectrum as broadening and red shift of the LSPR for increasing Au NP size. For instance, the pure dipolar modes dominate for particles of 30 nm or smaller,[118, 125] whereas the retardation effects play important roles for Au NPs above 60 nm.

3.3.3 Shape

The key to achieving broad LSPR tunability without sacrificing the linewidth of the resonance is to vary the nanoparticle shape. The position, and number of LSPR also depend on the shape of the MNPs. Over the past decade, a myriad of new MNP shapes, such as nanorods (NRs), nanoshells (NSs), nanowires, nanocubes, nanostars, nanotriangles, and nanocones, have driven a new wave of interest in tuning their LSPR properties.[3, 9, 41, 48, 119, 126, 127] The effect of particle shape on LSPR properties was dramatically demonstrated in the work of Mock et al., in which the spectra of silver nanoparticles of different shapes (spheres, triangles, and cubes) but similar volume were correlated with their structure.[128] In general, NP symmetry reduction is an effective method to modify the position, number, and intensity of LSPR. For instance, Au nanospheres with the size of 2-50 nm show only one plasmon band centred at about 520 nm, while two LSPR peaks appear when the symmetry is reduced from spherical to cylindrical, i.e. in Au NRs.[119, 129] The first peak corresponds to the plasmon oscillations along the minor axis, while the second one appears due to the plasmon oscillation along the major axis. By increasing the aspect ratio D of the NR (i.e.the major to minor axis ratio), the position of second LSPR can be shifted from the visible to the NIR range.[129–132]

There has been a great deal of interest in nanoparticle shapes with sharp features or tips, which have been developed through both bottom-up (chemical synthesis) and top-down (lithography) methods. Some of these include silver[133] and gold[134] nanocubes,[135–137] nanostars,[29–31, 61–63] nanotriangles,[36] Au trisoctahedron (TOH),[75–80] and gold nanocrescents.[138] Primary effect of the sharp tips is to produce a red shift in the plasmon resonance. Moreover, sharp features exhibit additional advantage for molecular detection at the microscopic level in that MNPs as the sharp tip creates a localized sensing/mode volume of highly enhanced electric field intensity.[3, 9, 30, 31, 41, 61–64, 68–70, 72, 73, 126, 127]

3.3.4 Other factors

Apart from these primary factors (as discussed above), the LSPR behaviour of nanoparticles also depends on the other factors,[119] like surface chemical interactions,[118, 139] temperature,[132, 140] pressure,[141, 142] non-local effects,[8, 143, 144] assembly of MNPs,[145] composition of the MNP etc.[3, 9, 41, 48, 119, 126, 127]

3.4 Probing LSPR

In recent years, the tremendous advances in instrumentation coupled with breakthroughs of synthesis methods has helped to construct several novel techniques to probe the plasmonic behaviour of single metal nanoparticles (MNPs), each with a different combination of spatial resolution, spectral resolution, expansion capabilities and ease of use and implementation. In general, these techniques can be classified in to two major groups according to their detection techniques: near field and far field techniques. The near-field optical techniques measure the optical behaviour by introducing a physical, optical probe in close proximity to the particle,[146–150] a concept first outlined by Synge in 1928.[151] A sub-diffraction-limited optical imaging technique, such as near-field scanning optical microscopy (NSOM), can achieve a resolution of $\sim$ 20 nm or slightly better, but (in the case of NSOM) is constrained by the requirement of fabricating very sharp tips and furthermore, interaction of the tip with the light in the structure often perturbs the localised surface palsmon (LSP) mode,[95] making it challenging to probe the detailed spatial profile of the resonance. So, search for a non-perturbing probe to directly explore the plasmonic behaviour including the imaging of LSP modes with high spatial resolution around MNPs remains a challenging task.

In contrast, far-field approaches are capable of probing the optical properties of MNPs from a distance much larger than the wavelength of light. Among several far field methods, the dark-field microscopy, surface enhanced spectroscopy etc. techniques have drawn much attention owing to their unique detection techniques. For example, optical dark field microscopy (DFM) has been considered as the prominent far field technique to explore the LSP behavior of the MNPs with excellent spectral resolution by probing the scattering phenomena of MNPs depending on the shape and size of the MNPs.[96, 97, 152–155] Additionally, in DFM technique, a light source excites the whole volume of the nanoparticle and therefore unable to probe the rich features arising out from the different parts of the highly complex shaped nanostructures like nanostar/flower and trisoctahedron. However, DFM technique is constrained by the diffraction limit to a spatial resolution of about half a wavelength.[26, 95]

The surface enhanced spectroscopy like surface-enhanced Raman spectroscopy (SERS) is a powerful vibrational technique that allows for highly sensitive and selective detection of low concentration analytes through this plasmonic amplification of electromagnetic fields.[90, 156–158] The electromagnetic enhancement mechanism under LSPR condition is generally believed to be the primary contributor to the SERS effect, while the chemical mechanism, which primarily results from charge transfer between the metal and molecule, provides a minor enhancement effect. It is an indirect far field characterization tool that provides the information about the average electric field enhancement around a particle or cluster of particle, leading to better understanding of plasmonic phenomena. However SERS imaging is also suffered by the diffraction limited lateral resolution of Raman microscope. In a typical optical beam based far field experiment, the spatial resolution is limited by the so-called optical diffraction limit to around half the wavelength of light. In this regard, techniques based on e-beam spectroscopy like CL has been shown to be an excellent probe of plasmons with a very high spatial resolution [37] and due to the non-contact nature they do not have undesirable effects on the measured quantities. The electromagnetic field carried by the electron beam acts like a very local plane wave or supercontinuum source of white light.[8, 21, 159, 160] It is this field which is scattered by the MNPs in the case of CL. Moreover this electromagnetic field (an electric field in the QS approximation) associated with the incoming electron that polarizes the NP of interest, which itself generates an induced field. Now one can compute the CL by estimating energy carried by the induced field and propagating to the far-field. In the subsequent sections of this Chapter, a few theoretical aspects of CL from MNPs will be addressed.

3.4.1 Interaction of fast electron with matter

For metals bombarded with e-beams the excitation of bulk or surface plasmons can occur when the moving charge couples to the free electrons in the metal. This effect was observed first in EELS and provided a first proof of the excitation of bulk and surface plasmons.[5] First observations of light emission from surface plasmons (SPs), excited by electrons and coupled out using gratings, were done by Teng and Stern.[161] Heitmann used electron excitation of SPs to map their dispersion relation on silver gratings.[162] Yamamoto et al. first reported the use of electron irradiation to determine the spatially-resolved mode distribution of plasmons localized in silver nanoparticles.[103]

3.4.1.1 Moving electron as an evanescent source of light

With respect to the Figure 3.2 electron of charge e, moving with a constant velocity v along the z axis, has been considered. It is also assumed that the electron is incident from the lower half space $z < 0$ which is taken to be vacuum ($\epsilon_1 = 1$), and it crosses the interface with the upper half space filled with a dielectric of permittivity $\epsilon_2 = \epsilon$ at $z = 0$ and time $t = 0$. The dielectric can be either a metal ($Re(\epsilon) < 0$) or dielectric ($Re(\epsilon) > 0$). The expression for electric (E) field satisfying Maxwell's equation can be written as:[8]

$$E(\vec{r}, \omega) = \frac{2e\omega}{v^2\gamma_\epsilon\epsilon} g(\vec{r}) \tag{3.7}$$

where

$$g(\vec{r}) = e^{\frac{i\omega z}{v}}[\frac{i}{\gamma_\epsilon} K_0(\frac{\omega R}{v\gamma_\epsilon})\hat{z} - K_1(\frac{\omega R}{v\gamma_\epsilon})\hat{R}] \tag{3.8}$$

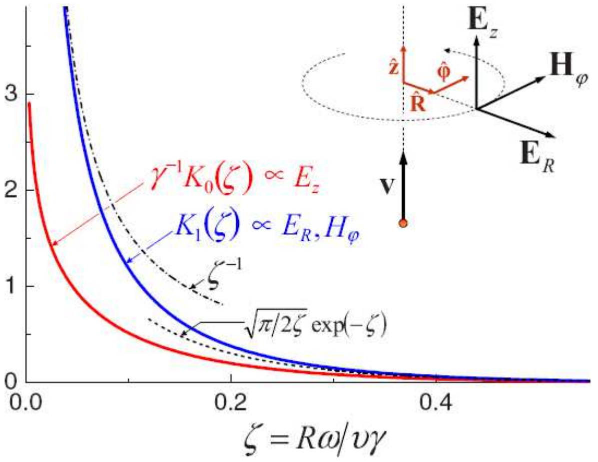

Figure 3.2: *Evanescent character of the electromagnetic field produced by a fast electron. Transverse-spatial direction dependence of the* $\exp(-i\omega t)$ *contribution to the electromagnetic field set up by an electron moving in vacuum with velocity* $v = 0.7c$ *(*$\gamma \approx 1.4$ *and kinetic energy* $\approx$ *200 keV) along the positive* z *axis. The only non-vanishing components* E_R*,* E_z*, and* H_φ *decay exponentially at large distance* R *from the trajectory. The inset shows the orientation of these components relative to the electron velocity vector. The small-R limit is dominated by the* $1/R$ *divergence of* E_R *and* H_φ*. Image adapted from Ref.[8]*

$\gamma_\epsilon = 1/\sqrt{1 - \epsilon v^2/c^2}$ is the Lorentz contraction factor and R is the distance from the electron trajectory. Similarly the magnetic field can be written as:

$$H(\vec{r}, \omega) = -\frac{2e\omega}{vc\gamma_\epsilon} K_1(\frac{\omega R}{v\gamma_\epsilon}) e^{i\omega z/v} \hat{\varphi}, \tag{3.9}$$

where $\hat{\varphi}$ is the azimuthal unit vector. From equations [3.7-3.9], one can see that moving electron acts as a broadband source of electromagnetic field with the frequency components of the field moving with velocity v along the electron trajectory. The exponential decay with R of both $\vec{E}(\vec{r}, \omega)$ and $\vec{H}(\vec{r}, \omega)$ arises from the asymptotic behavior of the modified Bessel functions K_m for large arguments. Interestingly, the external field of the electron, diverges at positions of the trajectory (Figure 3.2), meaning, theoretically infinite resolutions. Consequently, this signifies that the actual resolution of experiment is only limited by the finite size of the beam spot.

3.5 Cathodoluinescence

Since the first observation of cathodoluminescence (CL) in the mid-nineteenth century as the light emission stemming from cathode electron rays hitting a glass substrate, CL is now routinely used as a material characterization technique in mineralogy, semiconductor physics, and other fields. For example CL is widely utilized in mineralogy [163–165] to resolve the composition, contamination, and defects of natural structures with submicron detail. It is also a common tool to study the electronic bands of insulators [166] and semiconductors [167] and particularly the effect of dopants.[168] Apart from these applications, CL also offers an excellent and novel methodology to probe the surface plasmon mediated optical properties of the metal nanoparticles (MNPs).[8, 159]

In a CL technique, a fast electron beam or cathode ray is sent on to a sample, and the emitted light is collected to a CCD camera or serial detector coupled with a spectrometer (schematic diagram is shown in Figure 3.3). In last few decades, SEM/TEM fitted with CL spectroscopy has been considered as an essential tool in probing the optical properties of nanoobjects extensively at subwavelength scales, which is not easily accessible in standard standard optical techniques, such as visible-UV spectroscopy or photoluminescence (PL) and confocal set-up etc. Although the electron beam spectroscopy is being used in investigating the optical properties of the metal nanoparticles (MNPs), the surprising fact is that the electron never interacts with light in free space owing the momentum mismatch.[8, 22–27, 30, 31, 101–106, 159, 160, 169] So the question is, how the optical properties are being measured using the electron beam based spectroscopy. The underlaying physics can be explained as follows.[159] A fast electron carries a Coulomb field. A MNP close to the electron trajectory experiences a time-varying electric field pointing from the electron to the MNP. Consequently, MNP feels a pulse of electromagnetic radiation owing to the interaction between the electric filed and the MNP. The strength of the pulse depends reciprocally on the distance between the MNP and the electron beam trajectory, the electric field being mostly perpendicular to the electron axis. In this situation the electron beam acts like a plane wave packet of light propagating along the electron path. Since the pulse is relatively short in time (for a 10 nm thick NP and an electron traveling at half the speed of light, the interaction time is typically less than a femtosecond (fs)), the spectrum of the electromagnetic field accompanying the electron is white.[8, 159] Since the Coulomb interaction between the MNP and the electron is highly localized in nature, the electric field is concentrated over a very small volume. Thus the electron can act as a highly localized source of white light which may take part in the absorption, scattering or in luminescence phenomena.[8]

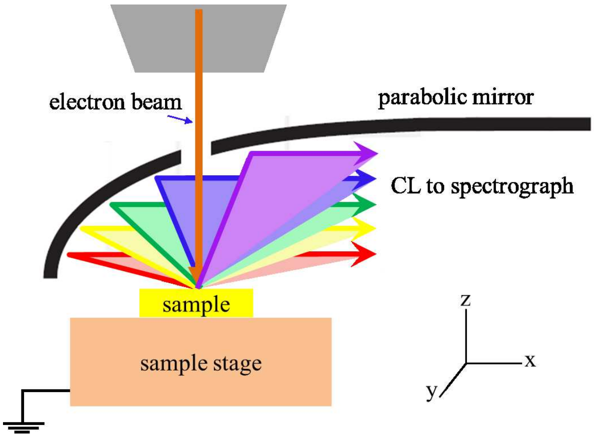

Figure 3.3: *Schematic diagram of CL technique.*

3.5.1 Basic principle of CL emission from MNP

The CL processes can be distinguished in two ways with respect to their degree of coherence: coherent CL and incoherent CL. Here the coherence maintains the conservation of energy and momentum between the excitation and the released photons. The incoherent CL process is nearly similar to the photoluminescence process: the sample is first excited and then it decays inelastically by emitting light. A typical example of incoherent CL emission is the indirect transition of an excited electron from the conduction band to the valence band in a semiconductor with indirect band gap. Such a transition requires the involvement of phonons while the emitted photons only supply the necessary energy.

Similarly, the interaction of the electron with a material gives rise to electromagnetic far-field components that are coherent with respect to the external evanescent field accompanying the moving charge. These far-field components produce the electron-induced radiation emission or "EIRE". There are several mechanisms of coherent light emission such as, transition radiation, Cherenkov radiation and diffraction radiation.

A charged particle like an electron, passing through a transparent medium, will emit Cherenkov radiation if its speed v is faster than the phase velocity of light in that medium, i.e. $v > c/n$ where n is the refractive index of the medium. Cherenkov radiation is mainly observed in dielectrics and not in metals, and will not be considered in the context of this thesis.

Transition radiation is emitted if a charged particle passes through a boundary between two media with different dielectric constants. It is created by the time dependent variation and eventual collapse of the dipole moment formed by the incident electron and its image charge in the dielectric. It is employed in crystallography to identify and characterize materials.

Surface plasmons in MNPs have finite lifetime due to radiative decay, Landau damping (e-h pair creation), and other absorption mechanisms. The former is rather efficient when the particle has non-negligible size compared to the corresponding light wavelength. Actually, the CL signal resulting from plasmon decay offers an opportunity to resolve plasmons spectrally and spatially in following way: electrons can be used as a broadband point dipole source to excite plasmon resonances, such that one can detect and locally map plasmonic behaviour by monitoring the events accompanying electron excitation. In case of coherent CL, one can measure the probability for an electron to emit a photon of given energy during the interaction process between the sample and the electron beam. This probability is commonly called "EIRE probability" when the scattering process is elastic.[170]

The CL emission comes from the skin depth under the sub-surface of metals ($\sim$ 20 nm in the visible and NIR for noble metals) which drastically erases any effects arising from the electron solid collision cascade produced by the impinging electron probe in deeper region. Moreover radiative inelastic decay has insignificant contribution to CL in metals because electronic relaxation channels are faster by several orders of magnitude. Therefore, the CL signal arising from MNPs, is dominated by EIRE. CL is computed by estimating the energy carried by the induced field and propagating to the far-field. The basic principle of CL is that energy is coupled from energetic electrons to the plasmon modes of the MNP and subsequently to the propagating light modes that constitute one of the prominent decay channels for plasmons into the far-field radiation (CL). The CL intensity can be calculated by integrating the Poynting vector over the emission directions. The emitted energy per incoming electron is given by:[8]

$$\Delta E = \int_0^\infty \hbar\omega d\omega \int d\Omega \Gamma_{CL}(\Omega, \omega), \tag{3.10}$$

where

$$\Gamma_{CL}(\Omega, \omega) = \frac{1}{4\pi^2 \hbar k} |f(\Omega)|^2 \tag{3.11}$$

is the number of photons emitted per incoming electron, per unit solid angle of emission Ω, and per unit of photon frequency range ω.

3.5.2 Plasmon mapping with CL

The interaction between an electron and a plasmonic NP is capable of producing a transient electric dipole at the point of impact. The power emitted by the transient dipole is related to local density of plasmonic states with a given relation:[171]

$$P = \frac{\pi\omega^2}{12\epsilon_0} |\vec{p}|^2 \rho_p(\vec{r}, \omega) \tag{3.12}$$

where $\vec{p}$ is the transient or induced dipole for CL, and ρ_p is the radiative portion of the local density of states (LDOS) projected along the direction of the transition dipole.[21, 103, 171, 172] This simple analytic expression conveys that the radiative power of the transient dipole efficiently couples through the radiative modes of plasmonic MNP into the far-field. Consequently, by scanning the electron beam over the entire NP allows us to spectrally resolve radiative modes of individual NP as the LDOS of plasmonic NP are very strongly correlated to the electric field of the plasmon modes of the NP.[8, 173, 174] The photon excitation map can be recorded by scanning the electron beam over the sample. Each pixel implies the superposition of the radiative strength of all plasmon modes of the NP, at the scan location. For instance, the bright pixels corresponds to the areas where the strongly excited plasmon modes emits the photons. The most important point is that CL mapping for MNPs reveals the efficiency with which electron energy is coupled to the far-field radiation as a function of electron injection position and not the distribution of light emission. The resolution of the technique is slightly larger than the beam spot size with an upper limit dictated by the extension of the evanescent electric field of the electron ($\sim v/2\omega$), where v is the electron velocity and ω is the light frequency (e.g., $v/2\omega = 16$ nm for 30 keV electrons at a wavelength of 600 nm).[23, 104]

3.6 Modeling LSPR of MNPs

3.6.1 Analytical methods: Mie theory

Mie theory provides the optical properties for homogeneous spherical particles embedded in a dielectric medium.In 1908, Gustav Mie gave a quantitative explanation of the size dependent optical properties of metal nanospheres.[6] This analytical approach is purely based on Maxwell equations and on the multipole expansion of the electromagnetic fields. However, over the years, the theory was extended to coreshell spheres,[175] and radially inhomogeneous spheres.[176]

3.6.2 Numerical methods: Non-spherical particle

In most of cases of real interest, particles are far away from exhibiting a spherical symmetry. But Mie theory is applicable to very simple isotropic geometry like sphere or infinite cylinder. To solve Maxwells equations in arbitrarily shaped structures, numerical simulation is necessary. The availability of fast numerical solvers of Maxwells equations using numerical approaches have enabled the rapid analysis of the properties of complex metallic nanostructures using realistic material parameters and in realistic, anisotropic dielectric environments. The discrete dipole method or DDA, also known as the coupled dipole method, was originally introduced by Purcell and Pennypacker for describing light scattering by interstellar dust grains,[108] and was subsequently developed by Draine et al, who also created the popular DDSCAT code.[177] However in past few decades many new computational tools, such as the finite difference in the time domain method (FDTD),[62, 109, 110] the boundary element method (BEM) [111, 112] and finite element method (FEM) [113] are introduced to understand and control the unusual, nonlinear and surprising responses of small metal NPs to light or electron beam. Among several numerical methods, FDTD method has drawn rich attention to study the LSP properties of nanosystems due to simple parametrization, and implementation.

3.7 Finite-difference time-domain based electrodynamic calculations

Recently the finite-difference time-domain method (FDTD) has been considered as one of the most popular techniques to solve the electromagnetic problems, such as scattering from metal objects and dielectrics, antennas, microstrip circuits, and electromagnetic absorption in the human body exposed to radiation. The FDTD domain method relies on propagation of the electromagnetic field defined on a spatial grid through consecutive time steps. The main three reasons of the success of the FDTD method are simple parametrization, simple implementation and time consuming of the FDTD programming even in a case of three-dimensional code.[109] For anisotropic and arbitrarily shaped MNPs the field is so complex that analytical solution of Maxwell's equations is not possible. So the electromagnetic fields in the presence of arbitrarily shaped MNPs must be solved by sophisticated numerical methods. Here the FDTD method and its application in CL based MNP plasmonics will be discussed.

The FDTD technique was first proposed by K. Yee, and then improved by others in the early 70s. In the FDTD approach, both space and time are divided into discrete segments. Space is segmented into box-shaped cells, which are small compared to the wavelength. The Maxwells equations are solved considering central difference approximations through the "leap-frog" algorithm. Practically, it means that to approximate Maxwells equations in space and time using this algorithm, one should calculate first all **H** field values, then all **E** field values, remembering always that E and H are shifted also in space by half of the discretization. According to Yee scheme, 3D Cartesian volume element of sides Δx, Δy, Δz and total volume Δ, is used for the space discretization. In this cubic volume element, E and H components are staggered at half increments in space and time (where Δt is the step size for time discretization).

According to Maxwell's equation:

$$\frac{\partial \vec{E}}{\partial t} = \frac{1}{\epsilon}[\vec{\nabla} \times \vec{H} - \vec{J}] \tag{3.13}$$

$$\frac{\partial \vec{H}}{\partial t} = -\frac{1}{\mu}[\vec{\nabla} \times \vec{E} - \vec{M}], \tag{3.14}$$

where ϵ is the permittivity and μ the permeability of the medium. The electric and magnetic current density, $\vec{J}$ and $\vec{M}$ respectively, are given by:

$$\vec{J} = \vec{J}_{Source} + \sigma \vec{E} \tag{3.15}$$

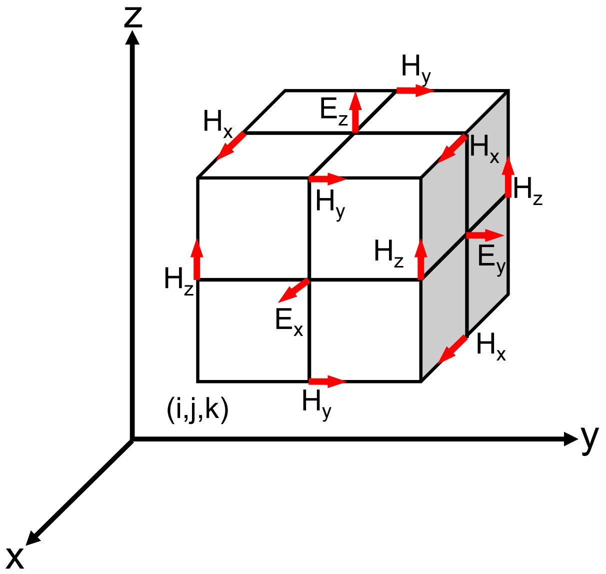

Figure 3.4: *Position of the various field (electric and magnetic)components within the Yee grid. Image courtesy ref. 178.*

$$\vec{M} = \vec{M}_{Source} + \sigma^{*}\vec{H}, \tag{3.16}$$

where, σ is the electric conductivity of the medium and σ^{*} is the equivalent magnetic loss.

If Equations 3.15 and 3.16 are put in Equations 3.13 and 3.14 and the vector components are evaluated, one gets a system of coupled equations which is the heart of FDTD algorithm. As for example, the E_x component is defined as:

$$\frac{\partial E_x}{\partial t} = \frac{1}{\epsilon}[\frac{\partial H_x}{\partial y} - \frac{\partial H_y}{\partial z} - J_{source_x} + \sigma E_x]. \tag{3.17}$$

Utilizing Yee's definition of rectangular coordinate system, one can formulate a finite difference equation from Maxwell's equation in discrete form. According to this, the E_x component at the time step $(n + 1/2)$ at one space point of the lattice $(i, j + 1/2, k + 1/2)$ that stands for the spatial location $(i\Delta x, j\Delta y, k\Delta z)$ is given by:

$$\begin{aligned}\frac{E_x|^{n+1/2}_{i,j+1/2,k+1/2} - E_x|^{n-1/2}_{i,j+1/2,k+1/2}}{\Delta t} &= \frac{1}{\epsilon_{i,j+1/2,k+1/2}}\cdot \\ &[\frac{H_z|^{n}_{i,j+1,k+1/2} - H_z|^{n}_{i,j,k+1/2}}{\Delta y} - \frac{H_y|^{n}_{i,j+1/2,k+1} - H_y|^{n}_{i,j+1/2,k}}{\Delta z} \\ &- J_{Source_x}|^{n}_{i,j+1/2,k+1/2} - \sigma|_{i,j+1/2,k+1/2}E_x|^{n}_{i,j+1/2,k+1/2}] \qquad (3.18)\end{aligned}$$

As the coefficients are fixed throughout the simulation, so they can be pre-calculated:

$$\begin{aligned}E_x|^{n+1/2}_{i,j+1/2,k+1/2} &= C_a(m)E_x|^{n-1/2}_{i,j+1/2,k+1/2} \\ &+ C_b(m)(H_z|_{i,j+1,k+1/2}n - H_z|^{n}_{i,j,k+1/2} - H_z|i,j,k+1/2^{n} + H_y|^{n}_{i,j+1/2,k} \\ &- H_y|^{n}_{i,j+1/2,k+1} - J_{Source_x}|^{n}_{i,j+1/2,k+1/2}\Delta), \qquad (3.19)\end{aligned}$$

where $C_a(m)$ and $C_b(m)$ are constants associated with the medium [178]. A more detailed and rigorous derivation can be found in Ref. [110, 179]. It is evident from Equation 3.19 that the electric field components at each point in space and in time can be calculated from the previous time step's electric component, the neighboring magnetic field components of the space lattice and the material properties. The software calculates the field components at each space point, for a specified time from the data stored and calculated previously. Then the software increases the time step and repeats the process. In the same way, similar equations can also be derived for the H field. By placing a field calculating 'monitor' at the desired location inside the simulation mesh, the software records the field components and power at each time step and outputs them for analysis at the end of the simulation. By taking the discrete Fourier transform of the stored time data at the end of simulation the E and H field behavior at each frequency, for a cell, can be calculated.

For numerical stability there is some restriction on Δt and the cell size. The fields (electric and magnetic) must not change significantly between the cells and hence the cell dimensions must be significantly less than the illumination wavelength. The minimum time step and/or cell size is determined by the Courant condition:

$$S = \frac{c\Delta t}{\Delta}, \tag{3.20}$$

where, S is the Courant number and it should be $\leq \frac{1}{\sqrt{no.of dimension}}$ for numerical stability. Hence for 3D simulation it should be $\leq 1/\sqrt{3}$ [179]. Usually in practical FDTD simulations, the cell size Δ is defined first to ensure sufficient resolution to define the structure geometry. The cell size is typically given by:

$$\Delta \leq \frac{\lambda_{min}}{10 n_{max}}, \tag{3.21}$$

where, λ_{min} is the shortest wavelength present and n_{max} is the highest refractive index present in the simulation region. So, after defining the cell size the minimum Δt can be calculated using Equation 3.20.

Due to the memory limitations the simulations must be finite and one needs proper boundary conditions at the wall of the domains. The commercially available FDTD software package from Lumerical FDTD Solutions [180] has been used in performing the numerical calculations. The important features of this software package will be briefly discussed. Several contents of this section has been taken from the FDTD reference guide which is available from `http://docs.lumerical.com/en/fdtd/reference_guide.html`.

3.7.0.1 CAD layout editor

At the user end of the graphic interface, there is a CAD layout editor in Lumerical FDTD solutions. The layout editor has two modes of operation: ‘layout mode’ and ‘analysis mode’. ‘Layout mode’ is used to setup the simulation. Simulation objects can be added, modified and deleted in this mode. After a simulation is completed, the layout editor automatically switches to ‘analysis mode’. In ‘analysis mode’, it is not possible to edit the simulation objects. The layout editor also shows graphical representation of the simulation from an XY, XZ, YZ and 3D perspective view. There is an in-built object library that includes a wide range of basic and complex objects with a documented script that can be modified to change the shape and size. More complex structures can be generated using combinations of basic structures.

3.7.0.2 Meshing and convergence

FDTD Solutions uses a rectangular, cartesian style mesh. Fundamental simulation quantities (material properties and geometrical information, electric and magnetic fields) are calculated at each mesh point. With the FDTD method, it is not possible to resolve interfaces to higher precision than the size of the mesh used. This is an important issue to consider for plasmonic simulations, since the results are often very sensitive to the size of the mesh near interfaces.

One solution is to use mesh override regions to force a very small spatial mesh to more accurately resolve the locations of the metal interface. The disadvantage of this method is that it can greatly increase simulation times and memory requirements. Lumericals conformal mesh technology can allow us to obtain more accurate results for a given mesh size, so it is always worth considering this mesh refinement method over the traditional stair-casing method. Conformal variant 0 is the default setting during all simulations unless mentioned specifically.

The mesh accuracy is an integer from 1 to 8 defining the fineness of the mesh in the FDTD domain. The number of mesh points per wavelength (ppw), where the wavelength is the shortest wavelength of the simulation bandwidth, is a major consideration for the meshing algorithm.[181]

The auto-shutoff parameter is a built-in convergence criterion of Lumerical FDTD Solutions, associated to the total amount of energy remaining in the simulation domain. The lower the auto-shutoff, the less energy remains, the better the convergence.[181]

3.7.0.3 Material database

The materials database allows one to manage (create, modify, delete) the materials that are available for use in simulations. The material database stores the material data to be used in the simulation. Experimental data can also be loaded into the database. A number of materials database are provided with the product installation. As a time domain technique, a single simulation can be used to provide simulation results at many frequency points. This provides the ability to analyze and optimize the design across a wide wavelength range but this is only true to the extent that the models used to describe the dispersive nature of the constituent materials are themselves accurate over the wavelength range of interest. To overcome the multi-wavelength challenge, Lumerical's multi-coefficient materials (MCMs) have been used. MCMs rely on a more extensive set of basis functions to better fit dispersion profiles that are not easily described by Drude, Debye, and Lorentz materials. With a comparable cost in model complexity and computation speed, the resulting MCM model is superior to the Lorentz-Drude model. The dielectric constant / refractive index used in the calculations are obtained from generalized MCM that fits the experimental dispersion data obtained from different tabulated databases [182–184] that fits better.

3.7.0.4 Sources

A number of source options are available with FDTD solutions, which are mentioned below:

- **Point dipole source:** Oscillating dipoles act as sources in Maxwell's equations to produce electromagnetic fields. Their position and direction are specified in terms of the center position and their orientation.

- **Gaussian and thin lens sources:** A Gaussian source defines a beam of electromagnetic radiation propagating in a specific direction, with the amplitude defined by a Gaussian cross-section of a given width. By default, the Gaussian sources use a scalar beam approximation for the electric field which is valid as long as the beam diameter is much larger than the diffraction limit. For a highly focused beam, there is also a thin lens source that injects a fully vectorial beam.

- **Plane wave sources:** Plane wave sources are used to inject laterally-uniform electromagnetic energy from one side of the source region. In 2D simulations, the plane wave source injects along a line, while in 3D simulations the plane wave source injects along a plane. It is also possible to inject a plane wave at an angle.

- **Total-field scattered-field (TFSF) sources:** Total-field scattered-field sources are used to separate the computation region into two distinct regions: one contains the total field (i.e. the sum of the incident field and the scattered field), while the second region contains only the scattered field. The incident field is a plane wave with a wave-vector normal to injection surface.

- **Mode sources:** The mode source is used to inject a guided mode into the simulation region. The geometry of the mode source (i.e. center location, and span) is used to compute the guided modes for the structure.

3.7.0.5 Normalization

The frequency power and frequency profile monitors record the electric and magnetic fields at a series of user-defined frequencies. These can be returned in either the continuous wave normalization state (cwnorm), or the no normalization state (nonorm). For most applications, the default cwnorm state is used. In the nonorm state, the returned fields are simply the Fourier transform of the simulated time domain fields. In the cwnorm state, the fields are normalized by the Fourier transform of the source pulse, thereby yielding the impulse response of the system. As it will be shown later in simulations of electron beam one need to deal with a large number of dipole sources and the normal normalization scheme do not work.

3.7.0.6 Boundary conditions

Boundary conditions (BCs) are very crucial in EM and simulation techniques. FDTD Solutions/propagator supports a range of boundary conditions, such as perfectly matched layer (PML), metallic, periodic, Bloch, symmetric and anti-symmetric.

Perfectly matched layer (PML) boundaries absorb the electromagnetic energy that is incident upon them. Plasmonic simulations very often employ absorbing BCs that allows the radiation to propagate out of the computational area without interfering with the field inside. PML is particularly useful when absorbing radiation in normal incidence. The number of layers depends on the mesh size. More layers causes the simulation to consume more memory. In all simulations presented in this thesis PML BCs have been used.

Other BCs like metal BCs are used to specify perfectly reflecting boundaries allowing no energy to escape along the boundary from the simulation volume. Periodic BCs can be applied when both the structures and the electromagnetic fields are periodic. Bloch BCs can be used where the structures and the electromagnetic fields are periodic but a phase shift exist between each period. Symmetric BCs can be used when the structure has one or more planes of symmetry. Both the structure and the source must be symmetric. Anti-symmetric BCs can be used when the problem exhibits one or more planes of symmetry. Anti-symmetric boundaries are anti-mirrors for electric fields and mirrors for magnetic fields.

3.7.1 FDTD simulation with electron beam as excitation source

In the present work, electron beam from a scanning electron microscope (SEM) has been used as the source of electromagnetic (EM) excitation during numerical calculations unless mentioned specifically. In present CL experiments, the electron beam energy of 30 keV with a beam current of $\sim$15 nA were used. This means the electron impact to the sample on an average in every 11 ps, which is $\sim$ 5000 times longer than one typical optical cycle in the visible spectral range and $\sim$ 200 times longer than the typical electron relaxation time in gold. So, we can neglect the electron-electron interaction and simulate the photon emission for one single electron impact. In this numerical procedure we have modeled the energetic electron as a large number of closely spaced dipoles placed vertically with a temporal phase lag that is associated with the electron velocity. The current density can be written as:

$$\vec{J}(t, \vec{r}) = -ev\hat{u_z}\delta(z - vt)\delta(x - x_0)\delta(y - y_0), \tag{3.22}$$

where e is the electronic charge and v is the velocity of electron, (x_0, y_0) represents the position of the electron beam and z is the direction of electron velocity and $\hat{u_z}$ is the unit vector along z direction. The introduced phase lag factor between two consecutive dipole is (z/v), where $v = 0.32c$ corresponding to the 30 keV electron energy used in the present experiment with c being the velocity of light in free space. In the absence of any structure, the e-beam will not generate any radiation because it is moving at a constant velocity. But in FDTD, we are obliged to simulate only a finite portion of the electron beam path and the sudden appearance and disappearance of the dipole beam will induce radiation. To minimize error arising due to this issue, we run a second reference simulation where all the structures have been removed, and we can calculate the electromagnetic fields at angular frequency ω by taking the difference in fields between the simulations. The CL emission spectra are calculated by integrating the Poynting vector components (P_z) normal to a large NP. In order to calculate the near field intensity $(|E|^2)$ map and the charge distribution map corresponding to the calculated CL emission spectra, field monitors were placed the at suitable planes passing through or very near to the nanoparticle. The dielectric constant / refractive index used in the calculations in the wavelength range 500-900 nm are obtained from generalized MCM that fits the experimental dispersion data obtained from different tabulated databases [182–184] that fits better. The Si substrate is considered as a nondispersive material with fixed refractive index 4 in same wavelength range, and having a dimension of 5 μm × 5 μm × 4 μm. The metallic structures having resonant characteristics and high index contrast interfaces are critically sensitive to the precise locations of material interfaces. So, for a better accuracy in all the calculations, Lumerical's mesh override region has been used over all the metallic structure.

In these type of simulations, one wants to calculate the response to a series of dipoles of amplitude p_0, where p_0 is independent of frequency, i.e. the impulse response which would be created in the time domain with a dipole of the form $p(t) = p_0\delta(t)$, where $\delta(t)$ is a Dirac delta function. In the frequency domain it gives $p(\omega) = p_0$. In reality, true Dirac delta function, which is numerically challenging, is not used. Instead a short pulse is used. To get the impulse response then, one need to divide the results by the spectrum of the pulse used to excite the dipole. Additionally, it is required to divide the electromagnetic fields by $1/i\omega$ after the simulation, and this comes from the fact that we simulate the impulse response to dipoles but we actually want the impulse response from a current. Then both the normalization are included to get the impulse response and the factor of $1/\omega^2$ for power and $1/i\omega$ for field.

3.8 Applications related to local-field enhancement

The MNPs are potential candidate for amplifying the electromagnetic field near the particle surface through the far-field radiation at subwavelength dimensions under the LSPR conditions. The local field enhancement in NPs depends on the radiation generated by the radiative decay of the LSPR (i.e. light scattering), associated to time-dependent electromagnetic fields that extend beyond the NP surface in the near field by some nanometers, and transform into propagating plane waves in far-field distance (i.e. at a distance larger than photon wavelength). The local-field enhancement factor (EF) at any point $\vec{r}$ can be expressed as the ratio of the moduli of the local electric field E_{loc} to the incident electric field E_0 [48, 185]:

$$EF(\vec{r}) = \frac{E_{loc}(\vec{r})}{E_0} \tag{3.23}$$

EF is dramatically affected by the LSPR properties of NPs depending on the structural parameters and position around the surface of that NP, and can range from less than 1 up to $10^2 - 10^3$. The points with the largest EF in a single NP or a group of them are called electromagnetic 'hot spots'. In general, the discontinuity of the structures such as gap, void and sharp tip (nanocubes,[58, 186, 187] nanostars,[29, 30] nanotriangles,[23] nanodecahedra,[26, 27, 94, 152] nanotrisoctahedra [28, 58] etc.) can generate high electric field when interacting with external EM field. However, due to the strong plasmonic coupling effects,[9] the nanogaps between the adjacent particles of the ensembles on substrate may serve as 'hot spots' with gigantic local-field enhancements of several orders of magnitude higher than those achievable for LSPR of individual NP. The nanolensing behaviour has been exploited to enhance several types of optical phenomena in nearby molecules or materials, such as Raman scattering,[14, 15] enhanced fluorescence,[33] and enhanced photo carrier generation,[11, 34]. Among all these enhanced optical techniques, SERS is a state-of-the-art method that allows for highly sensitive and selective detection of low concentration analytes through this plasmonic amplification of electromagnetic fields.

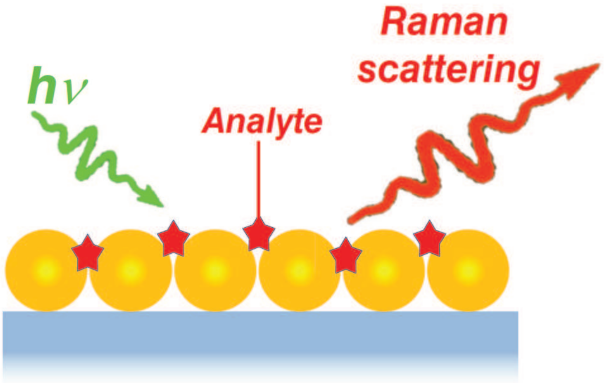

Figure 3.5: *SERS is exploited for ultrasensitive detection of analytes by Raman spectroscopy. The analyte emits intense Raman signals when attached on the MNP substrate. Image adapted from Ref.[119]*

3.8.1 Surface enhanced Raman scattering (SERS)

Surface enhanced Raman spectroscopy (SERS) is a powerful vibrational spectroscopy technique that allows for highly sensitive structural detection of molecules in very low concentrations and provides rich structural information. Since the discovery of SERS, researchers have attempted to understand how Raman signals can be enhanced so many orders. The intrinsic low efficiency of Raman scattering can be strongly improved if molecules are placed close to plasmonic MNPs (shown in Figure 3.5). The SERS enhancement relies on two main mechanisms: electromagnetic field (EM) enhancement and chemical (CM) enhancement.

In order to understand the complete SERS enhancement response after placing molecules on the metal particles, we have to find out the EM enhancement factor for both the metallic part as well as the molecular part. It is very well known fact that Raman scattering arises from the induced dipole radiation of molecules, where the induced dipole is proportional to the incident field $\vec{E}$. The relation between induced dipole moment $\vec{P}$ and the incident field $\vec{E}$ can be expressed as,

$$\vec{P} = \alpha_M \vec{E} \tag{3.24}$$

where $\vec{P}$ is dipole moment, α is molecular polarizability, and capital M refers to the molecular properties to distinguish from the dielectric materials.[156–158] It is also very well known that when we place a molecules on the metal particles such as sphere and excite the system with incident field E_0, the electric field is enhanced under LSPR condition, and the electric field becomes [158]

$$E_{out} = E_0 + E_{induced} \tag{3.25}$$

Now the molecule placed very closed to metal surface experiences the electric field E_{out} and induces a dipole moment

$$\overrightarrow{P_M} = \alpha_M \overrightarrow{E_{out}} \tag{3.26}$$

The induced oscillating dipole creates its own electric field E_{dip} and radiates at Raman frequency. This new induced electric field E_{dip} also interacts with the metal particle again to generate a new secondary scattering dipole and electric field at Raman frequency. Although the interactions between molecules and metal particles become much complicated after introducing the molecules on metal particles, one can calculate the electric field enhancement factor using appropriate approximation. However the approximated electric field enhancement factor (EF) can be expressed as,[156, 157]

$$EF = \frac{|E_{out}|^2 |E'_{out}|^2}{|E_0|^4} \tag{3.27}$$

where E_0 is incident field, and E_{out} is output field after local field enhancement mechanism. The fields are evaluated at the frequency of incident light and the frequency of Raman scattering, which represented without primed and with primed symbol respectively. One can further assume that the output fields at two frequencies are almost the same, i.e. $E_{out} \sim E'_{out}$; so EF is proportional to E^4. This is so-called E^4 approximation and is commonly reported in the literatures.[90, 156, 157] In experimental approaches, the enhancement factor (EF) of Raman signals is calculated using following equation:[156]

$$EF = \frac{(I_{SERS})(N_{normal})}{(I_{normal})(N_{SERS})} \tag{3.28}$$

I_{SERS} and I_{normal} are the intensity of particular Raman mode observed in the SERS and normal spectra, respectively; N_{normal} and N_{SERS} are the number of the molecules in the excitation volume for the normal Raman acquisition and number of adsorbed molecules on metal NP, respectively.

Another effect on SERS enhancement mechanism is chemical enhancement. Chemical enhancement (CM) is due to chemical effects from the interaction between molecules and metal surfaces such as charge transfer effect. The exact nature of the CE is still debated in the literature. However, The CM effect results from the formation of new molecule-metal surface complex and changes the polarizability of the molecule. Now the formation of this state can be resonant at the excitation laser wavelength, leading to a resonantly-enhanced Raman signal.[188, 189] From theoretical electrodynamic calculation, EM enhancement factor usually varies in the range of $\sim 10^6 - 10^8$ depending on the shape, size and material of the NP, whereas the CM enhancement factor varies typically from $10^1 - 10^2$, which is much less than EM mechanism.

Chapter 4

Inter tip coupling effect on the plasmonic behavior of individual multi-tipped gold nanoflower

The CL spectroscopy and imaging of plasmon modes have been performed to explore the inter tip plasmonic coupling effect of individually multi-tipped nanoflower. The experimental results are supported by rigorous FDTD simulations.

4.1 Introduction

Tuning the frequency of the LSPR by varying the shape, size and composition of MNPs as well as understanding the LSPR coupling of individual MNP with the other closely lying particles is a recent trend [9] in the area of plasmonics research. In this context multi-tipped (also called multi-pod, nanostar or nanoflower) MNPs, especially, gold nanostars/ nanoflowers are an exciting new class of plasmonic structures. Gold (Au) nanoflowers (NFs) consist of a near-spherical core from which numerous sharp tips of different lengths point outward. According to theoretical predictions,[62] each LSPR mode for single gold nanoflower (AuNF) is associated with one individual tip and the corresponding hotspot is located at the tip assuming a wide separation among the tips so that tip to tip interaction can be neglected. Moreover, a tip to core plasmon coupling has also been invoked by the so-called plasmon hybridization model.[62] Most of the reported works on individual Au nanostar/nanoflower so far has demonstrated no tip to tip interaction.[30, 32, 62, 63, 73] This was primarily due to the large angular separation between the tips. However, if the number of tips in a single nanostar increases, angular separation between any two tips may be very small. In those cases, due to the random orientation of the tips protruding in three dimensions, tip-tip interaction cannot be neglected. Tip-tip interaction with the incident EM field may modify the spectral and spatial localization of the LSPR mode of the individual tips. This aspect, which has far reaching consequences in designing AuNF morphology based SERS active substrate for maximizing the Raman signal, has not been addressed so far to the best of our knowledge. Consequently, experimental demonstration of the modification of LSPR properties in spectral and spatial domain for closely lying tips of a single Au-NF is of utmost importance from the perspective of light matter interaction at the nanoscale.

Here, we use CL-SEM technique to demonstrate the localization of electron beam excited plasmonic hotspots at the tips of individual AuNF. We present a detailed study of coupling between nearest neighbor tips originated from the same spherical core of the AuNF. The experimental CL spectra resulting from the electron beam impact near the apex of the closely spaced double tip matches well with the spectra calculated using finite difference time domain (FDTD) numerical method. The calculated electric near field intensity maps along with the associated vectorial plots of induced electric field show local enhancement of the field distribution in the apex and nearby region between the tips caused by the accumulation of charges of opposite signs at the neighbouring tips. This confirms tip to tip or intertip coupling in a single gold multi-tipped nanoparticle, an aspect which has never been addressed before in the case of multi-tipped star / flower shaped gold nanoparticles. Furthermore, using 3D-FDTD simulations we also show that a narrow angular separation between the nearest neighbor tips triggers the onset of intertip coupling.

4.2 Methods

4.2.1 Nanoparticle synthesis

The wet chemical systhesis procedure of the Au NFs has been discussed in Chapter 2 briefly.

4.2.2 Cathodoluminescence (CL) measurements

CL spectroscopy and imaging have been performed using the Gatan MonoCL3 optical detection system attached with ZEISS SUPRA40 field emission gun (FEG) SEM,[116] the details of which has been described in Chapter 2. In the present study the data were recorded with an electron acceleration voltage of 30 kV and beam current of about 15 nA. To minimize sample drift during acquisition, the experimental spectra have been acquired in two wavelength ranges separately: 500 700 nm and 700 900 nm, respectively. Spectral step size and dwell time were kept fixed at 4 nm and 0.25 s respectively during the entire experiment. The monochromatic CL images are recorded with 150 × 150 pixels and the total exposure time in capturing one frame is 11.25 s.

4.2.3 FDTD Simulations

3D- FDTD (commercially available FDTD package from the Lumerical Soln., version 8.4) numerical simulation has been performed for the rigorous analysis of the surface plasmon assisted photon emission. In this present study, the electron beam has been used as the source of EM excitation. The details of the electron beam simulation is discussed extensively in Chapter 3. The geometric parameters like lengths, curvature of the tips were measured from the HRSEM images, and then were used for modelling of the Au NF structure. The dispersive property of gold in the wavelength range 500-900 nm has been taken from tabulated value of Johnson and Christy.[182] The Si substrate is considered as a nondispersive material with fixed refractive index 4 in same wavelength range, and having a dimension of 5 μm × 5 μm × 4 μm. The metallic structures having resonant characteristics and high index contrast interfaces are critically sensitive to the precise locations of material interfaces. So, for a better accuracy in all the calculations, we have used the Lumerical's mesh override region over all the metallic structure. The size of fine mesh cells near the metallic structure was kept in a same value during all the numerical simulations and it was 2 nm × 2 nm × 2 nm.

4.3 Results and Discussion

Observations under SEM reveal that the nanoparticles are often aggregated in clusters (SE image in Figure 4.1a). However, one can also find sporadically spread isolated single multitipped gold nanoparticle. Representative SE image of such a single Au nanoparticle at high magnification is depicted in Figure 4.1b-f for different tilt angles (ϕ) of the sample stage (with respect to the impinging e-beam of the microscope) to aid clear visualization of the shape, size and orientation of the adjacent tips with respect to one another. During CL study the sample stage is restricted to be operated without tilt and consequently, CL experiment was performed on this Au particle without tilt (SE image in Figure 4.1b). Morphologically, the single Au particle selected here (Figure 4.1b) is a multi-tipped spherical core from which the conical and petal shaped tips are protruding out in three directions resembling like a flower and hence we will term this as gold nanoflower (AuNF) in the present study. In the following, we first collect the spectral data from tips marked as A, B, C, D and E of the AuNF shown in the inset SE image of Figure 4.2a (the same as shown in Figure 4.1b) where the tips A (length and maximum diameter are 73 nm and 34 nm respectively), and C are relatively longer (C being the largest tip of length 120 nm with a maximum diameter of 65 nm) than the tips B (length and diameter are 46 nm and 35 nm respectively), D (length and maximum

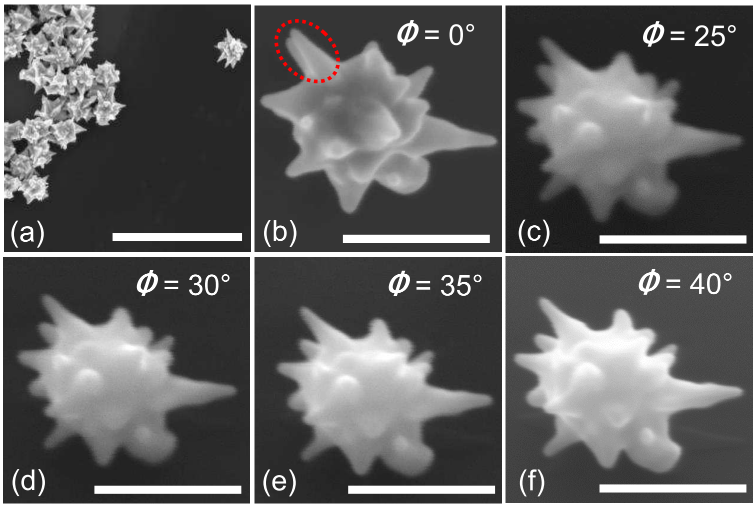

Figure 4.1: *(a) SEM image of chemically synthesized gold nanoflowers in aggregates. (b) Selected isolated multi-tipped particle for the CL study. (c-f) Series of HRSEM images at different tilt angles, (ϕ, with respect to the incoming e-beam direction), confirm that two tips of nearly equal length encircled in (b) are aligned along out-of-plane direction with a narrow angular separation between them. The scale bar is 200 nm.*

diameter are 40 nm and 30 nm respectively) and E (length and maximum diameter are 35 nm and 30 nm respectively). Figure 4.2a shows CL spectra taken from apex regions of the above marked tips. The complete spectra were taken in two different wavelength ranges, 500-700 nm and 700-900 nm to make the sample not to be exposed under e-beam for longer time so that any adverse effect by e-beam induced drift on the spectral shift/distortion is minimized. The CL spectrum is strongest at the resonance peak wavelength near 736 nm in addition to the other resonance peaks around 670 nm, 780 nm and 800 nm for the e-beam impact on the apex region of the tip A. The presence of resonance peaks slightly blue-shifted from 670 nm is common in the CL spectrum arising for the e-beam impact at the tips B, D and E. On the other hand the e-beam impact at the apex of tip C gives rise to two resonance peaks at around 860 nm and 590 nm. Moreover, few weak peaks between 500 nm and 600 nm are also visible in all the spectra. To extract

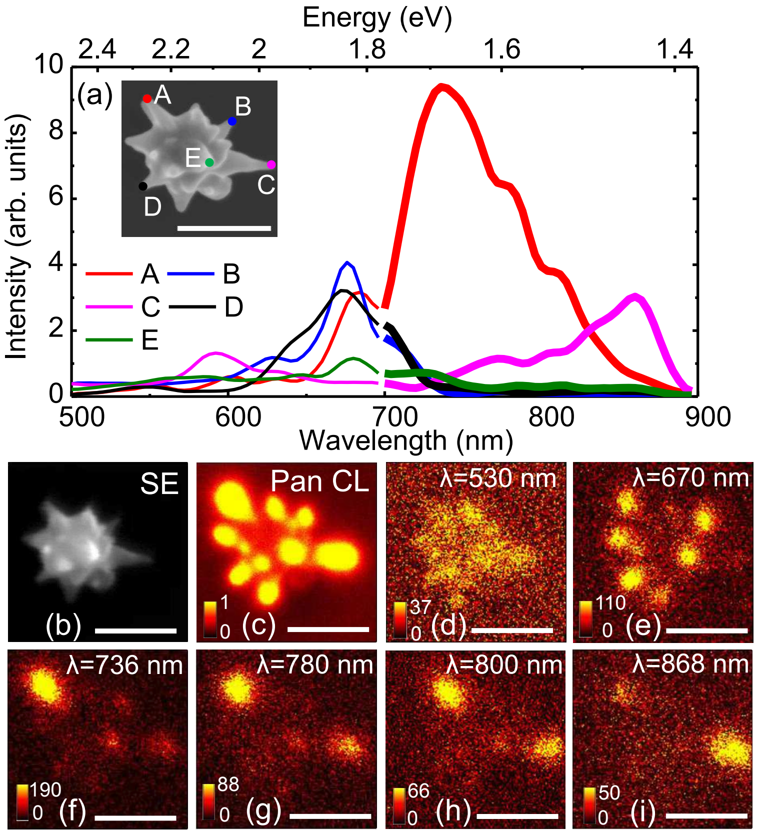

Figure 4.2: *(a) Experimentally acquired CL spectra from different tip apex regions marked as A, B, C, D and E of the AuNF. The inset SEM image shows the e-beam impact points with different colored dots. (b) The SE image of the same AuNF and the corresponding (c) panchromatic CL image along with the monochromatic CL maps for the selected resonance wavelengths (d) 530 nm, (e) 670 nm, (f) 736 nm, (g) 780 nm, (h) 800 nm and (i) 868 nm. The scale bar is 200 nm.*

the spatial distribution of the photon emission, we acquired monochromatic CL maps at different peak wavelengths (Figure 4.2d-i) along with panchromatic CL map (Figure 4.2c). Bright spots in the photon maps arise when the LSP modes are resonantly excited by the evanescent field associated with the electron beam. Intense luminescence is already discernible at the individual tips from the panchromatic photon map (Figure 4.2c). The monochromatic CL image obtained at 530 nm wavelength shows luminescent intensity when the electron beam scans over the core region (Figure 4.2d). Strong light emission occurs at other resonance wavelengths when the e-beam scans over the apex region of the tips. The LSPR at 530 nm is close to the plasmon mode of the spherical core.[30, 31, 62] The monochromatic photon maps of Figure 4.2d-i show that the luminescence enhancement of the AuNF is shifted to the far ends of the longer tips with the increase of the resonance wavelengths. This is consistent with the spectroscopic data presented in Figure 4.2a as well as with our recent study.[30] The resonance wavelength of the tip plasmon mode depends strongly on the aspect ratio of the tip. The observation of the red-shift of the LSPR peaks with increasing tip length is well established both theoretically and experimentally.[30, 62] Interestingly, while the photon maps corresponding to the CL peak wavelengths 736 nm, 780 nm, 800 nm and 868 nm (Figure 4.2f-i) indicate strong photon emission from individual longer tips of the AuNF, the CL map at 670 nm wavelength (Figure 4.2e) shows light emission from multiple tips preferably of shorter length. This is expected as the CL spectra originating from the e-beam impact near the apex of shorter tips (namely, B, D and E) are overlapped and peaked more or less near 670 nm. Moreover, the region of the spectrum beyond 670 nm is overlapped with the tail region of the strong resonance peak at 736 nm (originating from e-beam impact at tip A). Consequently, in the corresponding monochromatic map at 670 nm, we also see luminescence from tip A as well, while the e-beam scans near tips A. The resonance peaks associated with the longer tips correspond to the low-energy dipolar modes with plasmon oscillations confined around the tip regions.[63, 66] The 670 nm peak is most probably due to the dipolar mode of oscillation of shorter tips, which are present in a large number near the core surface.[30] The general trend of our experimental finding is that for all the shorter tips (B, D and E), the major plasmon mode (dipolar) lies in the wavelength range 600-700 nm.

In passing, plasmonic response of a multi-branched particle is dependent on the shape, size and number of the constituting branches/tips.[62, 63] However, the orientation of the tips with respect to the substrate also plays a very crucial role on the plasmonic properties as demonstrated quite recently by Das et al. [30] using FDTD based numerical simulation for a model single tip Au nanostructure sitting on Si substrate. The study [30] showed reduction in the intensity and red shift of LSPR peaks while the tip was moving from the parallel (w.r.t the substrate) position towards the substrate maintaining the e-beam excitation on the tip apex. On the otherhand when the tip was moving away from the substrate the observed blue-shift of the tip LSPR was attributed with uncoupling of the tip and the substrate (screened by the NP core). From the inset SE image of Figure 4.2a, it is clear that tips B, D, E are oriented more or less away from the substrate as compared to the longer tips A and C. Consequently LSP modes corresponding to these tips are blue shifted w.r.t the tip A and tip C modes. Also tips B, D, and E being shorter tips with more or less similar lengths and diameter their spectral peak positions lie approximately at the same wavelength of 670 nm. For the longest tip C which is oriented more towards the substrate compared to the other tips studied here, both direct near-field absorption in the substrate and radiative emission into the substrate introduce a loss channel for the light confined in the particle. Consequently, one observes a broadening (i.e., damping) as well as reduced intensity in the corresponding emission spectrum at the resonance peak 868 nm (Figure 4.2a) for the electron beam excitation of the longest tip C. We discuss below about the tip mode A in detail.

The excitation of LSP caused by the e-beam impact at the apex region of tip A is of particular interest. Close inspection of the series of SEM images taken at different tilt angles (Figure 4.1b-f) clearly reveals that the tip A (encircled region of the SE image in Figure 4.1b) is not an isolated single tip but is accompanied by an adjacent lower tip. While the upper tip in the encircled portion (in Figure 4.1b) is approximately parallel to the plane of substrate, the lower tip is slightly oriented towards the silicon substrate making an angular separation (θ) between the upper and lower tip. It is also clear from the figures that the two tips are nearly equal in their lengths ($\sim$ 73 nm) and aspect ratio and originated from a spherical core of diameter $\sim$ 160 nm. The close proximity of the apex of the upper tip with the lower one along the same vertical axis of the incoming electron beam thus makes it highly probable that the enhancement in the local field distribution as well as the far field radiation due to excitation of any one of these two tips being affected by that of the other tip. Consequently, one can expect coupling of the modes between such closely lying tips for e-beam impact near the region marked as A. In the following, we will focus on the origin of the strongest resonance at 736 nm followed by the other small intensity peaks using FDTD numerical simulations. The numerical simulations were performed using the 3D-FDTD codes (commercially available from Lumerical Soln.). The details of the procedure has been described in the Methods section. We have modeled our AuNF structure as a spherical core having two conical tips (hereafter called as two tip model, TTM), the geometrical configuration of which with respect to the Cartesian co-ordinate system is defined in Figure 4.3. The two closely spaced tips (length and aperture

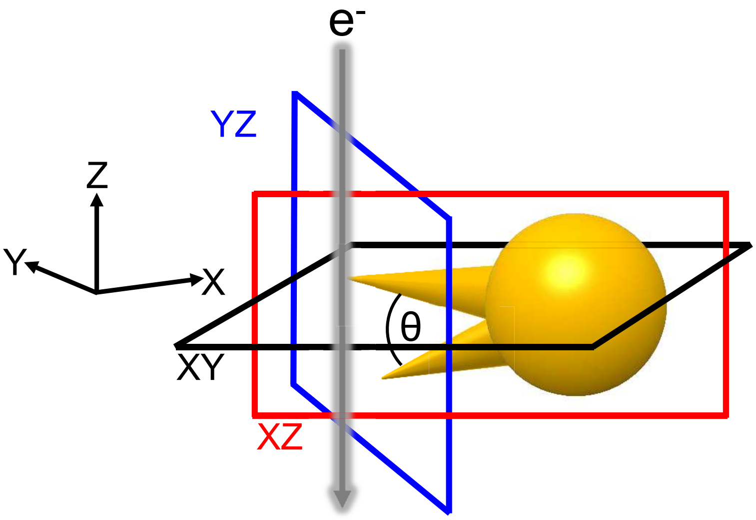

Figure 4.3: *Schematic diagram of the geometrical configuration of the AuNF along with the coordinate system used in the numerical simulation. The star (Two Tip Model/TTM) is modelled as a spherical core with two tips. Incident electron beam is highlighted by the arrow. Power monitors were placed at the XY, YZ, XZ planes, in order to calculate the near field intensity and the charge distributions. The electron beam is kept in fixed position during all numerical calculations unless mentioned specifically.*

angle of the upper tip are 70 nm and 15° and that of lower tip are 70 nm and 14°) are assumed to be aligned in XZ plane. During numerical simulation the modelled e-beam is injected to the apex of the upper tip as shown schematically in the inset of Figure 4.4a. The calculated emission spectrum (black curve in Figure 4.4a) with the resonance peaks at 733 nm and 786 nm matches reasonably well with the experimentally acquired CL spectrum (red curve in Figure 4.4a) having resonance peaks at 736 nm and 780 nm. It is also interesting to compare the emission spectra calculated with and without the Si substrate as displayed in Figure 4.4b. The presence of the silicon substrate does not affect the LSPR peak positions (Figure 4.4b). However the peak intensity is altered a bit. Hence, for numerical resource limitations, subsequent simulations are performed without the Si substrate unless mentioned specifically.

To understand further the effect of the individual upper and lower tip orientation separately on the spectrum, the spectrum was calculated assuming single tip model (STM). The individual spectrum calculated for the e-beam impact on upper tip only shows LSPR at 744 nm whereas for the e-beam impact on lower tip only shows resonance at 754 nm. Interestingly, the intensity for the upper tip is ~ 1.3 times higher than the lower one as shown in Figure 4.4c. The decrease in intensity

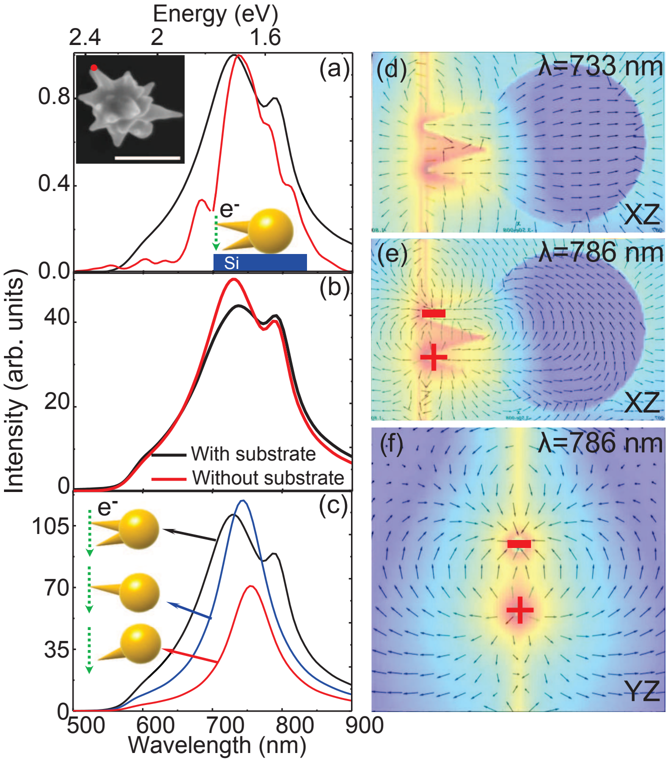

Figure 4.4: *(a) Normalized numerically calculated (3D-FDTD) spectrum (black curve) of the TTM structure and experimentally acquired CL spectrum (red curve) in the wavelength range 500 nm - 700 nm. Inset SEM image shows the e-beam is focused at the red colored position.(b) Difference between the calculated spectra of the TTM structure, with substrate (black curve) and without substrate (red curve). The spectra are calculated in 500- 900 nm range.(c) Simulated emission spectrum of different structures. The black curve represents the TTM structure. The blue and red curves represent the spectrum of the Single Tip model/STM structure for upper and lower tip respectively. Simulated near field intensity ($|E|^2$) maps and the corresponding field maps at (d) 733 nm wavelength in XZ plane, (e) 786 nm wavelength in XZ plane and (f) 786 nm wavelength in YZ plane for TTM structure.*

for the lower tip of nearly same dimension as the upper one can be accounted as follows: the evanescent field associated with the e-beam decays inversely with the distance from the e-beam trajectory at large distance from the beam. As a result, the strength of interaction with the e-beam is stronger for the upper tip than the lower tip due to the larger separation of the lower tip apex and the incident e-beam. This decreases the intensity of the resonance peak in the calculated emission spectra for the excitation of the lower tip as compared to the upper tip in the STM structure (Figure 4.4c). The small shift in the LSPR positions (~ 10 nm) can be due to the slight difference in the maximum diameter of the two tips. Moreover the finite mesh size used in FDTD simulations may also contribute to this small shift of 10 nm. Apart from this small shift in the calculated spectrum, the two resonance peaks for two individual tips at 744 nm and 754 nm seem to have the same type of plasmon mode, which is longitudinal dipolar in nature (shown in Figure 4.5). However, when the simulation is performed in presence of two tips (in TTM structure), this longitudinal plasmon mode is split into two separate new plasmon modes at 733 nm and at 786 nm as displayed in Figure 4.4c (black curve). The peak at 733 nm was blue shifted and the peak at 786 nm was red shifted with respect to the longitudinal mode at 744/754 nm calculated for the individual tips (in STM structure). This indicates that, whenever we have two closely lying tips of nearly equal dimension, we have a coupling between their plasmon modes. In order to calculate the near electric field intensity map and the corresponding mode of the surface plasmon oscillation (by plotting electric field vector map) at various resonant peak positions, we have placed field monitors at different planes in the TTM structure neglecting the silicon substrate, as shown in Figure 4.3. Now, from

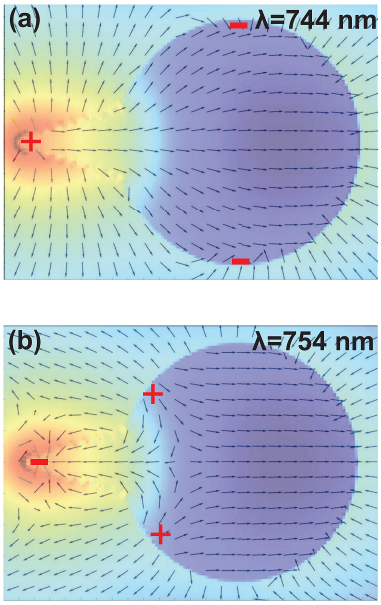

Figure 4.5: *(a) Longitudinal dipolar mode of oscillation at resonance wavelength (744 nm) in XY plane passing through the equatorial region of the spherical core of the STM structure (upper tip).(b) Longitudinal dipolar mode of oscillation at resonance wavelength (754 nm) in XY plane passing through the equatorial region of the spherical core of the STM structure (lower tip).*

the simulated near field intensity maps of Figure 4.4e we see strong localization of the field near the apex as well as in-between the upper and lower tip at 786 nm wavelength indicating the existence of very large surface charge on the tip at this wavelength. Indeed, the associated vector plots (in XZ plane) corresponding to this field intensity map show a clear dipole type field distribution where the accumulation of opposite charges is seen at the apex of the two tips. However, such tip to tip dipole formation is not observed in the vector plots (in XZ plane) at the resonance wavelength 733 nm (Figure 4.4d). Moreover, the uniform field distribution as seen in the calculated vector plots (Figure 4.4d) on the surface of the core at 733 nm is highly disturbed (Figure 4.4e) by the strong tip to tip transverse dipole field lines as well as by the field lines of the longitudinal plasmon of the individual tip interacting with the core. That the tip-tip interaction is very strong at the resonance wavelength 786 nm is clear from the calculated near field intensity map and its associated vector plots drawn also in the YZ plane (Figure 4.4f) as well.

Thus comparing the near field intensity maps along with the associated vector

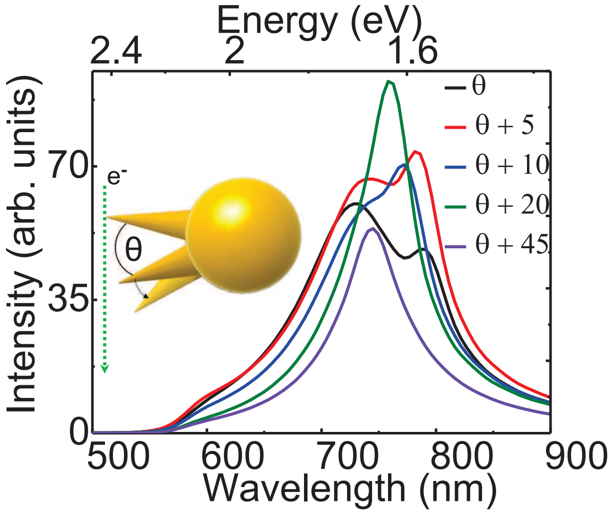

Figure 4.6: *Intertip coupling and resonance splitting in Two Tips Model/TTM structure as a function of the angular separation (θ) between two closely laying tips. The electron beam was kept in fixed position similar to the previous simulations.*

plots for the peak wavelengths 733 nm and 786 nm, the core-tip and tip-tip plasmonic modes of the AuNFs appears to be strongly coupled. Moreover, we have also verified using FDTD simulation that the coupling becomes more prominent when the adjacent tips are nearly equal in size. So, we presume the peak at 786 nm as seen in the experimental CL spectra of Figure 4.2g is a coupled LSP mode originating due to the strong electrostatic interaction between the two closely spaced out-of-plane tips of an AuNF where the oscillating dipole is aligned along the out of plane direction either in XZ or YZ planes as shown in Figure 4.4e, f. That such strong coupling of the LSPR modes leads to significant near-field enhancement as observed here is also accompanied by an increased non-radiative LSPR damping,[74] which is the reason why we see strongest intensity at the resonance around 736 nm (longitudinal dipole mode) observed in the present experiment. Although the coupling of the LSPRs between the two closely lying separate particles has been studied to some extent in recent years,[9] the evidence of the coupling within the two closely lying branches of a same nanoparticle as in the AuNF of the present study has not been reported so far to the best of our knowledge. However, we should mention here that while the experimentally acquired CL spectrum (Figure 4.4a) has four resonance peaks, the FDTD spectrum exhibits two resonance peaks. The difference can be attributed to the modelling with single or two tipped core compared to the actual one with numerous tips used in the CL experiment. The difference may also arise due to the finite size of the electron beam used in the experiment while the simulation considers only one electron as a series of closely spaced dipoles (see the FDTD simulations section).

Now, for deeper insight of the out of plane tip-tip interaction, the lower tip has been rotated in anti-clock wise direction keeping the upper tip at the same position (Figure 4.6). It is noted that with increasing angular separation (θ), the tip to tip interaction mode shows a blue shift. At lower angles less than $\theta + 10°$ when the tip apex are very close to each other, the induced charges near the apex of the tips can interact very strongly via electrostatic interaction requiring less energy. However, when the tip to tip distance is large at higher angular separation, obviously the tip-tip interaction requires more energy to compete the tip-core interaction. Consequently, coupled mode associated with the tip-tip interaction is shifted towards the high energy or shorter wavelength regime. From the spectra shown in Figure 4.6, it is also clear that the splitting of the resonance peak as per

TTM structure disappears gradually and turns into one LSP mode for very large angular separation. This single LSP mode is probably a mixing/combination of tip-tip coupled mode and core-tip longitudinal mode. Observation of such mode mixing is possible only by using of the electron beam as an excitation source, which can excite the longitudinal as well as the transverse plasmon mode at the same instant for its evanescent nature. At an angle greater than (θ + 45°), when the lower tip is far away from the upper tip, coupling between two tips become negligible. Additionally, the tip-core longitudinal plasmon mode for the lower tip also becomes less prominent due to the larger separation between the lower tip and the electron beam position. Consequently, the two tip model (TTM) will behave like the single tip model (STM) for upper tip showing only a single resonance peak at 744 nm (violet curve in Figure 4.6), similar to the spectrum of the single tip model applied for upper tip as shown in Figure 4.4c (blue curve).

4.4 Conclusions

In summary, site-specific cathodoluminescence (CL) spectroscopy and imaging technique in a high-resolution scanning electron microscope (HRSEM) have been used to investigate different localized surface plasmon (LSP) modes associated with the widely separated individual tips as well as closely lying tips of single gold nanoflower (AuNF) on a silicon substrate both in the spatial and spectral domain. The combination of CL-SEM technique and FDTD simulation have helped us to identify for the first time the plasmonic coupling between two nearest neighbor out-of-plane tips protruded from same spherical core. Detailed analysis shows that such intertip coupling within the same nanoparticle is effective within a narrow angular separation between the closely lying tips and is the origin of the double peaked strong resonance mode observed in the single AuNF of the present study. The simulated near field intensity maps drawn at the coupled LSPR mode show strong local field enhancement near the apex as well as in-between the closely lying upper and lower tip. This has far reaching consequences in designing Au nanostar morphology based SERS active substrate for maximizing the Raman signal. Consequently, the present study is important to understand the mechanism of local electron probe driven plasmonic interaction within different branches / tips of a single 3-D complex nanostructure that might have far reaching consequences in applications where localized electromagnetic field enhancement is exploited for maximizing the light signal, such as in surface enhanced Raman scattering based spectroscopy, bio-sensing or designing nanoparticle embedded solar cells.

Chapter 5

Trisoctahedral gold nanocrystal: A promising candidate for probing localised surface plasmons for surface enhanced Raman scattering

CL spectroscopy and imaging in a high-resolution SEM have been performed to investigate localized surface plasmon (LSP) behavior of trisoctahedral (TOH) gold (au) nanocrysrtals (NCs)on a silicon (Si) substrate. The CL analyses combined with FDTD simulations have helped us to explore LSP modes of TOH NCs extensively. Also, the experimental evidence of enhanced Raman scattering from these anisotropic and complex shaped TOH NCs indicating their possible technological applications in biosensing through SERS detection and SERS imaging.

5.1 Introduction

Recently, a new class of Au MNP structure, namely, trisoctahedral (TOH), which is a polyhedron bounded by 24 exposed high-index facets with Miller indices of $\{hkl\}$ $(h > l)$ has drawn much attention[75–80] because of its' superior catalytic [68–70] and SERS activities [58, 68] caused by the presence of high density of atomic steps and dangling bonds on the high-index facets. A well developed concave TOH has multitipped [58] appearance with sharp edges and corners those are favorable for possessing possible multiple "hot spots". For TOH particle where the different edges, corners and facets were oriented randomly with respect to the substrate, the possibility of the existence of out-of-plane modes along with the role of substrate on the LSP enhanced photon emissions were missing in the published reports.[58, 68] Consequently, experimental investigation on the spatial distribution of plasmons on single particle level is of utmost importance to understand the basic physics governing the local EM field enhancement.[23] Here, we report for the first time the photon emission spectroscopy and imaging of individual TOH Au NC using CL technique in a SEM. The experimentally obtained spectral and photon imaging data were extensively analyzed using FDTD numerical simulation to generate electric near-field intensity maps along with the associated vectorial plots. Such analysis helped us to identify the pattern of charge oscillations along the in-plane and out-of-plane directions corresponding to different LSP modes in addition to the effect of substrate on the plasmonic properties of individual TOH Au particle. Exploiting the strong EM field enhancement by LSPR of TOH Au NPs, we demonstrate the significant enhancement SERS active substrates through the surface enhanced Raman scattering studies.

5.2 Methods

5.2.1 Nanoparticle synthesis

The wet chemical systhesis procedure of the Au TOH NCs has been discussed in Chapter 2 briefly.

5.2.2 Cathodoluminescence (CL) measurements

CL spectroscopy and imaging have been performed using the Gatan MonoCL3 optical detection system attached with ZEISS SUPRA40 field emission gun (FEG) SEM,[116] the details of which has been described in Chapter 2. In the present study the data were recorded with an electron acceleration voltage of 30 kV and beam current of about 15 nA. To minimize sample drift during acquisition, the experimental spectra have been acquired in two wavelength ranges separately: 500700 nm and 700900 nm, respectively. Spectral step size and dwell time were kept fixed at 4 nm and 0.25 s respectively during the entire experiment. All the spectra are presented after averaging over five or six spectra for each electron beam position and then were corrected from the substrate background. The monochromatic CL images were recorded with 256 × 256 pixels and the total exposure time in capturing one frame was 13.10 s.

5.2.3 Surface enhanced Raman scattering (SERS) measurements

Raman scattering studies were performed using micro-Raman spectrometer (inVia, Renishaw) mounted in the back scattering configuration, the details of which has been described in Chapter 2.[190] The SERS substrates were prepared by spin coating the aqueous solution of TOH Au particles on Si substrates. Prior to the spin coating, Si substrates were treated with piranha solution to modify them as hydrophilic which helps in the uniform distribution of aqueous TOH shaped Au particles. The substrates were then ultrasonically cleaned with acetone, alcohol and subsequently dried with N_2 gas. TOH shaped Au coated Si substrates were then exposed to Ar-plasma for 2 min at 10^{-1} mbar, to burn the unnecessary carbon. Aqueous solution of Rhodamine 6G (R6G) molecules with different concentrations (10^{-4}M - 10^{-7}M) were used as analyte to study the SERS activity of the TOH Au particles. The samples were excited with Ar^+ laser of wavelength 514.5 nm and the scattered signals were collected using 100X objective. A grating of 1800 lines/mm and thermoelectrically cooled CCD detector were used to analyse and record the spectra.[190] The spectra were acquired at different places on the sample to make sure the homogeneous and reproducible SERS activity by the TOH Au particles. The SERS imaging was performed over a pre-defined area and grid resolution using fully automated motorized sample stage (Renishaw MS20), having a spatial resolution of 100 nm.[191] In the present study, a total area of 6 μm × 6 μm with 300 nm grid resolution is probed for the SERS mapping.

5.2.4 FDTD simulations

3D-FDTD simulations (from Lumerical solutions, Canada) were carried out to understand the electron beam induced LSP responses including the charge distribution, near-field intensity maps and substrate's effect of the TOH NP. In this present study, the electron beam has been used as the source of EM excitation. The details of the electron beam simulation is discussed extensively in Chapter 3. The geometric parameters like lengths, curvature of the corners were measured from the HRSEM images, and then were used for modelling of the Au TOH structure.

The dielectric constant/refractive index for gold in the wavelength range 500-900 nm was used from the data tabulated by CRC Handbook of Chemistry and Physics [184] which were fitted (Figure 5.1) using a multi-coefficient models (MCMs),[180] as the Lorentz, Drude and Debye models were often insufficient for real materials. MCMs deal with an arbitrary dispersion of a dielectric function through the more extensive set of basis functions. For FDTD simulations, the modelled TOH Au particle of edge length (Figure 5.2) 125 nm was assumed as a combined structure of one regular octahedron and eight triangular pyramids (considering equilateral in nature of triangular bases), where the triangular pyramids were attached on eight

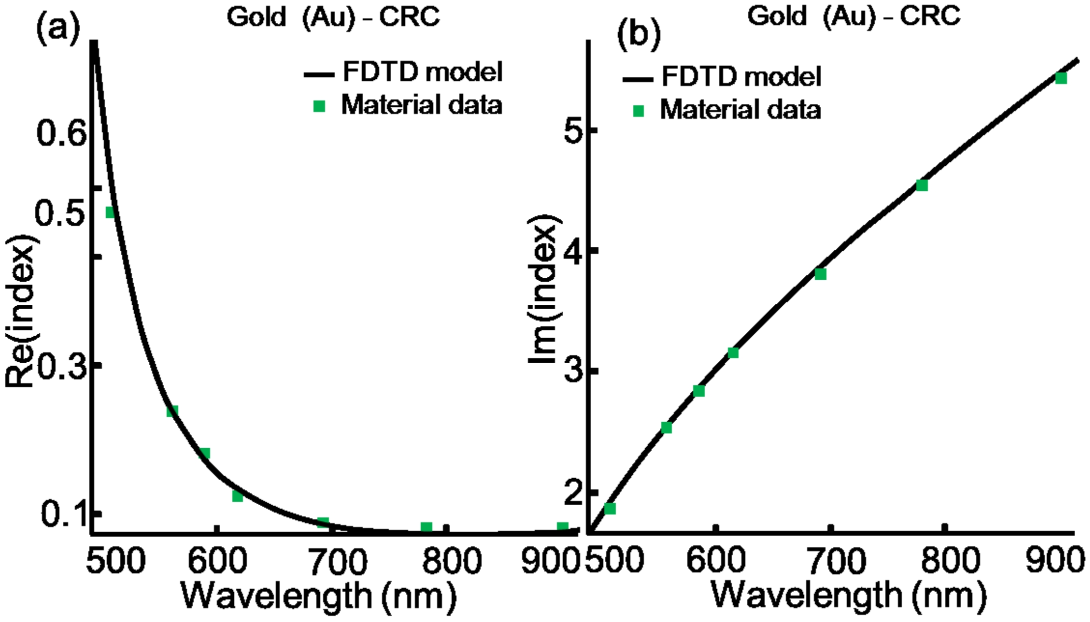

Figure 5.1: *The material data obtained from the CRC Handbook of Chemistry and Physics [Ref.184] has been fitted with the (a) real and (b) imaginary part of refractive index for the modeled Au TOH particle using the multi-coefficient models (MCMs). The images were directly captured from the Lumerical FDTD layout windows.*

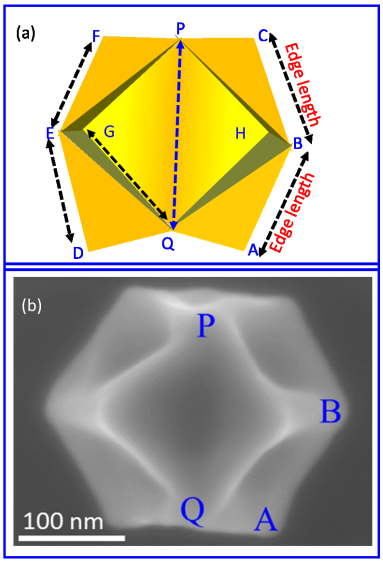

Figure 5.2: *(a) Schematic of a typical concave TOH shaped particle. The apex points are marked as A, C, D, F, G and H (similar to the studied geometry) and the base points are marked as E and B. The edge length of a TOH particle is defined as the distance between base and apex points. Here the edge is either AB or BC. The HRSEM measurement (inset figure) shows that the edge length of the studied particle is ∼125 nm. For simulation purpose we assumed this edge length to be 125 nm. The distance between the points P and Q is 190 nm (measured from HRSEM image, shown in (b)). This length is used as octahedron's edge length (also for the length of a side of triangular base of each pyramid) for simulation purpose. TOH particle has 2-fold rotational symmetry along the PQ plane. So, the point A, B and C are equivalent to the point D, E and F respectively at free-standing as well as at experimental configuration. When the TOH particle is rest on the Si substrate making an angle of 7.5° w.r.t the free-standing configuration, the points like A, D are nearer to the substrate than the points like B (or E), C (or F).*

{111} facets of the octahedron by 'pulling out' their apexes from the center of {111} facets.[58] Here, the edge length of the modelled TOH structure was defined by the edge length of each triangular pyramid. The edge length and the length of a side of triangular base of each pyramid were assumed to be 125 nm and 190 nm, respectively. According to the geometry of TOH structure, the edge length of octahedron is equal to the length of a side of the triangular base (i.e., 190 nm) of triangular pyramid. However, we have only considered the mesoscopic structural geometry in the modelling due to the limited computational resources in terms of memory and speed. The Si substrate was assumed as a non-dispersive material (with fixed dielectric constant of 4) within the wavelength range 500-900 nm. The dimension of the Si substrate was considered to be 5 μm × 5 μm × 4 μm in the present calculations. Here in our case, the mesh override region (2 nm × 2 nm × 2 nm in X × Y × Z direction) and FDTD mesh accuracy of 3 were kept fixed during all simulations constrained by our limited computational resources in terms of memory and speed.

In order to clarify the particle morphology and orientation of different points in presence and absence of substrate, we captured the 3D perspective view of the

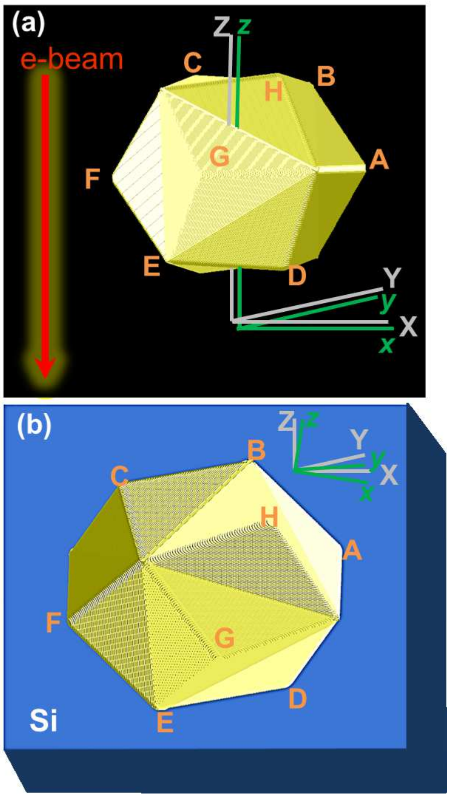

Figure 5.3: *3D perspective view of the TOH shaped particle modelled in the present FDTD software package layout in absence (a) and presence (b) of silicon (Si) substrate.*

TOH shaped particle directly from the 3D FDTD software package layout used in the present modelling. Figure 5.3a shows the orientation of the TOH morphology at free standing configuration (in free space) where the substrate is absent. The Cartesian coordinate axes defined for electron beam (e-beam) are designated by X, Y, Z (grey color) while the co-ordinate axes attached with the particle are designated with *x, y, z* (green color). For example, the incoming electron beam is indicated with the red arrow parallel to the Z axis. At free-standing configuration, both the coordinate frames coincide to each other and the points like A-F belong to the XY plane. On other hand, at experimental condition, while the particle is at rest on the substrate, two apex points and one base point (making a triangular plane) must have to be in contact with the substrate (Figure 5.3b) making the particle coordinate system being tilted with respect to the free standing configuration. By analyzing the SEM image of the TOH Au particle with the FDTD modelling we could determine the tilt angle of 7.5° between the Z axis and z axis while the particle is at rest on the substrate. Consequently, the points like A, D are nearer to the substrate than the points like B, C (shown in Figure 5.3b). The amount of this tilt angle will depend on the height of the triangular pyramid as well as the size of the TOH Au particle. For the normal SEM operation the sample mounting stage remains horizontal and one sees the top view of the particle from the SEM image. To understand the three dimensional (3D) perspective of the particle morphology and different facets or triangular pyramidal parts one needs to tilt the sample stage. See the Figure 5.4 for a representative SEM image at 45° tilt angle of the sample stage. However, during CL experiment one has to insert the light collecting paraboloid mirror for which the sample stage is constrained to remain

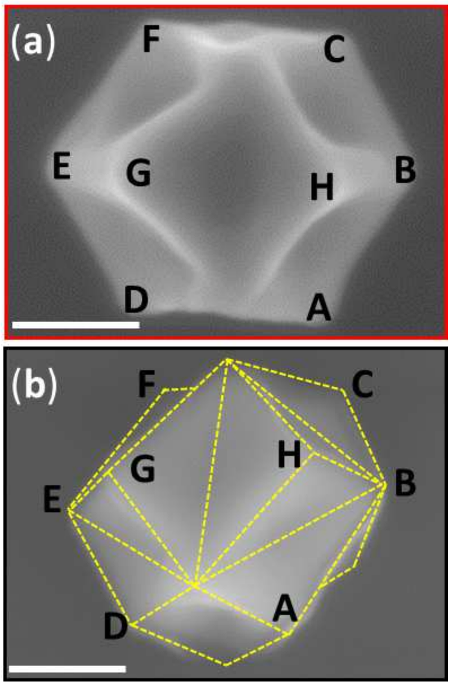

Figure 5.4: *HRSEM image of the selected TOH particle at (a) 0° and (b) 45° tilt angle of the sample stage. Scale bar is 100 nm.*

at horizontal position, a condition imposed by the maximum light collecting condition (see Cathodoluminescence Measurements section). This means, during CL experiments, while the sample is at rest on the substrate, the angle between Z and z is always 7.5° for the present TOH Au particle.

5.3 Results and Discussion

5.3.1 Cathodoluminescence Analyses

Figure 5.5a shows a representative SEM image of as-synthesized Au TOH nanostructures. The NPs are mostly aggregated in clusters. However, a single isolated TOH Au NP of edge length 125 nm (encircled with the red box), far from the clusters, is selected to investigate the LSP properties of such complex shaped MNP. Geometrically, the TOH particle is a crystalline structure where eight triangular pyramids are attached on the eight {111} facets of the octahedra by “pulling out” their apexes from the center of {111} facets. One of the pyramidal parts is very prominent in the tilted stage configuration of SEM imaging (Figure 5.5b). Figure 5.5c shows bright field (BF) TEM image of an aggregate of TOH particles in random orientations. In Figure 5.5e, we show the selected area electron diffraction (SAED) pattern from an isolated TOH particle (Figure 5.5d). The SAED pattern of the TOH NP can be indexed to the [011] zone axis of a single crystal of fcc Au; suggesting that the TOH NPs are single crystals,[75, 76] rather than multiply twinned crystals. Figure 5.6a shows the experimentally acquired site-specific CL spectra from different beam injected points marked as A-H.

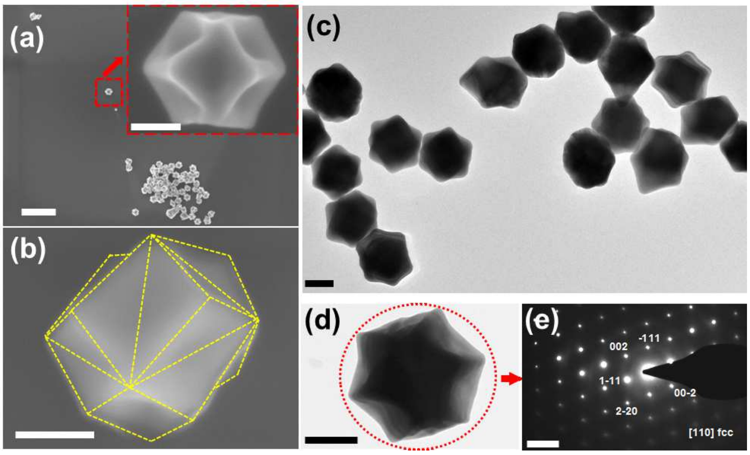

Figure 5.5: *(a) SEM image showing the aggregation of TOH Au particles on Si substrate. The studied particle is indicated with red colored box. The HRSEM image of selected TOH is shown in the inset figure. The scale bars in the figure and inset figure are respectively 1 μm and 100 nm. (b) SEM image of the TOH Au particle in tilted configuration of mounting stage. The scale bar is 100 nm (c) Bright field TEM image of a collection of TOH Au particles. An isolated TOH Au particle (encircled with red circle) and its corresponding selected area electron diffraction (SAED) pattern are shown in (d) and (e) respectively. The scale bars in the figures (c), (d) and (e) are 100 nm, 100 nm and 5 1/nm respectively.*

Now, the points namely, A, B, C and H are symmetric to the points D, E, F and G respectively, along the two-fold rotational symmetry [79] (Figure 5.2). The

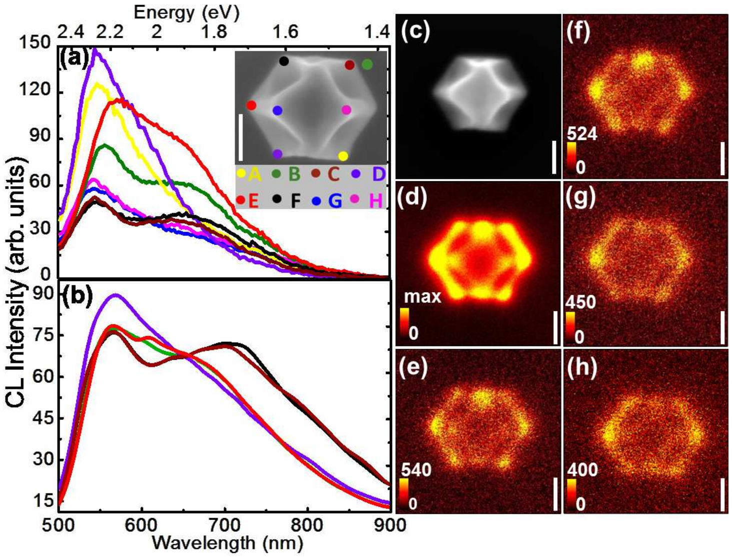

Figure 5.6: *(a) CL spectra from selected points marked as A-H of the studied TOH Au particle. The inset SEM image shows the electron beam impact points with different colored dots. (b) 3D-FDTD simulated spectra of the modelled TOH structure for beam impact at the points (A, B..., F). The electron beam is kept in 1 nm away from all the selected points during all numerical calculations, unless mentioned specifically. The SEM image and the corresponding panchromatic CL map/image of the same morphology are shown in (c) and (d) respectively. (e)-(h) Monochromatic CL maps/images at wavelengths 548, 560, 650 and 670 nm, respectively. Scale bar is 100 nm in all images.*

spectra were collected in two different wavelength ranges, 500-700 nm and 700-900 nm, to minimize the sample drift. Finally, the spectra were merged with proper normalization. It is interesting to note that except the points A, D electron beam impact at all other selected points gives rise to double peaked emission spectra. Moreover, the presence of lower wavelength resonant peak at around 548 nm in the CL spectra is common for electron beam excitation at all the marked points (A-H) showing gradual decrease in intensity as the beam probes from the symmetry points located nearer to the farthest from the substrate, specifically from A to C (see FDTD Calculations in Methods section and Figure 5.4), except the point E for which the lower wavelength peak arises around 560 nm. Consequently, the highest intensity peaks around 548 nm is observed for the electron beam impact on the points A and D (spectra with yellow and violet color in Figure 5.6a). For electron beam impact at B and E, the higher wavelength resonant peak occurs at around 650 nm. However, for beam impact at the points C and F the higher wavelength resonant peak occurs at around 670 nm. Remarkably, full-width at half maximum (FWHM) of the lower wavelength resonant peaks are less than half of that for the higher wavelength peaks, meaning lower wavelength resonant peaks are significantly narrower than the higher wavelength peaks (Figure 5.7). The broadening in all the spectra appear due to the increased damping.[8, 58]

Information about resonant peaks Marked positions	FWHM (in nm) of the lower wavelength (centered at around 548 nm) mode	FWHM (in nm) of the higher wavelength (centered at around 650 and 670 nm) mode
A	80	-
D	75	-
B	60	170 (at 650 nm)
E	60	183 (at 650 nm)
C	58	190 (at 670 nm)
F	53	193 (at 670 nm)
G	60	-
H	73	-

Figure 5.7: *FWHM of experimentally acquired different plasmon modes.*

Although we present here the experimental spectral data for a single particle, the reproducibility of our results is checked by more measurements (Figure 5.8). The spectral analysis of the experimentally observed CL resonant peaks corresponding to different LSP modes are corroborated with the spatial information through the wavelength specific photon maps or monochromatic CL images shown in Figures

5.6e-h preceded by a panchromatic CL map (Figure 5.6d). The plasmon induced luminescence is already discernible in the panCL image (Figure 5.6d) showing regions of high intensity emission at the points, marked as A-H. One can easily

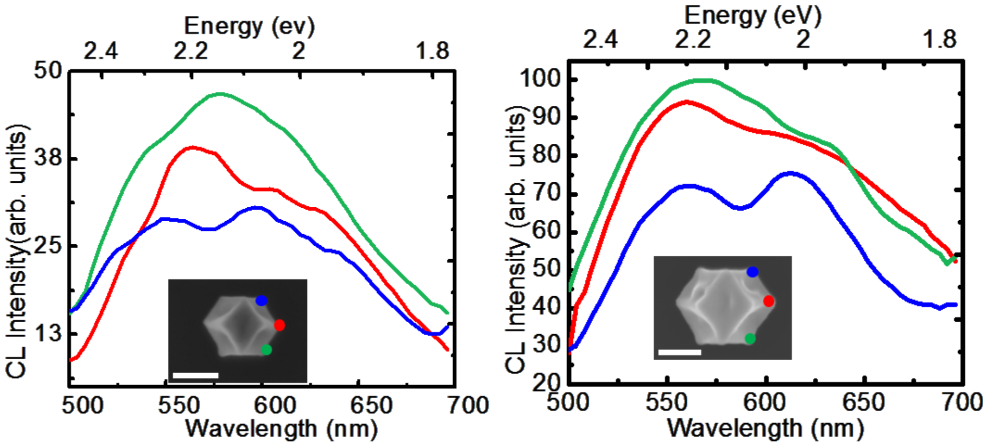

Figure 5.8: *Experimentally acquired CL spectroscopic data from TOH particle of different sizes (in terms of edge length). The single and double peaked nature with sufficient broadening is very common in all the spectroscopic results and we have analyzed the best data in this present article. Scale bar is 100 nm*

observe from the monochromatic photon maps at 548 and 560 nm (Figures 5.6e and f) that the luminescence features are nearly same in both the photon maps. Similar observation is also made for the monochromatic CL images of Figures 5.6g and h corresponding to the peaks 650 nm and 670 nm. This apparent small shift between maxima may just as well be due to the overlap of two resonant line shapes with varying weights. We thus have basically two LSP modes, one corresponding to the resonant peaks 548/560 nm and other corresponding to 650/670 nm.

The FDTD calculated spectra of the modelled TOH Au particle are shown in Figure 5.6b for all selected points except G and H. In modelling, the TOH Au particle is placed on Si substrate at rest making an angle of 7.5° (see the FDTD

Simulations in Methods section) between the Z axis and z axis reflecting the experimental configuration during CL measurement. Simulated analyses reveal that the lower wavelength LSPR mode always appears at 560 nm for all the selected points. Whereas experimentally it appears either at 548 nm or 560 nm. Interestingly, while comparing the calculated spectra with the experimental one, the best match with the experiment is found for the beam impact at the points B and E (green and red curve in Figure 5.6b). The small additional local maxima observed in the calculated spectra arise due to numerical artifact.[180] The experimentally acquired CL spectrum from point B and E should have been same due to symmetry reason. However, the experimental results show that there is a slight mismatch of ∼12 nm in the lower wavelength LPSR peak positions. The reason can be explained as follows: It is well reported in the published literature [94, 152] that the position as well as the intensity of any particular LSPR mode depends on the curvature and concaveness of the particles morphology among other factors. However, they are not exactly same for both the points as is evident from the HRSEM images (Figure 5.5a) rendering the difference in the spectra taken at these two points. In case of numerical modelling, we maintained equal roundness of curvature of 5 nm in all corner regions of the TOH Au particle. Consequently, the calculated spectra from both these points do not show significant difference. Mismatch between the experimental and simulated spectra appears to be more pronounced for the higher wavelength mode compared to the lower wavelength mode. As for example, for the electron beam impact at points C and F (brown and black curves in Figure 5.6b) where the calculated higher wavelength peak (720 nm) red shifts by 50 nm w.r.t the experimental high wavelength peak (670 nm). However, the calculated lower wavelength resonant peak (560 nm) red shifts only 12 nm compared to the experimentally observed peak at 548 nm for the CL spectra originating from points A and D (yellow and violet curve in Figure 5.6b). The mismatch between experimental and simulated spectra can be attributed as follows: the morphology of the selected TOH Au particle (shown in inset image of Figure 5.5a) in CL experiment is concave in nature. This concaveness is not perfectly maintained in the modelled TOH structure which introduces the red shift nature in the simulated spectra.[58] Additionally, the uncertainties in morphological details like surface roughness, roundness of curvature, as well as, the uncertainties in the dielectric constant, assumed in model calculation with those actually prevalent on the experimental Au particle where the possibility of ultrathin layer of surfactant cannot be ruled out; may also play a role. Overall, the fairly good agreement between experimental and simulated results indicates that the simplified modelling of the TOH shaped NP is qualitatively correct.

To get clear information about the origin of LSP modes and the corresponding oscillations of induced charges, we have performed 3D-FDTD numerical simulations in free-standing configuration without the Si substrate. For the sake of clarity an origami model of a typical TOH structure marked with the selected points of electron beam impacts A, B, H is presented in Figure 5.9a. Due to the two fold rotational symmetry [79] of TOH Au particle, the points A, B and C are equivalent to the points D, E and F, respectively. In order to calculate the near-electric field intensity ($|E|^2$) maps and the related electric field vector plots at various resonant peaks, two mutually perpendicular near-field power monitors are placed parallel to XY and XZ planes as depicted in Figure 5.9b. Here Figure 5.9c presents the

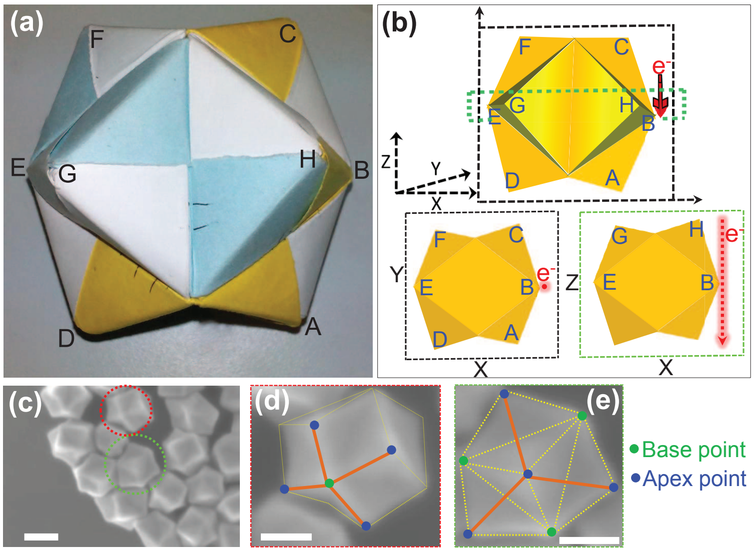

Figure 5.9: *(a) Image of the origami model of a typical TOH structure. (b) Schematic diagram of the TOH Au particle in free-standing condition. Power monitors are placed at XY and XZ planes. Cross-sectional view of TOH Au particle in XY and XZ planes are shown in the lower panel of (b). Under free-standing condition, the XY plane is parallel to the equatorial plane of the particle, i.e., perpendicular to electron-beam direction and the XZ monitor is parallel to the electron beam. (c) SEM image of ensemble of TOH Au particles, where the particles are orientated in different directions. The scale bar in (c) is 100 nm. To visualize the base and the apex points, two isolated particles are selected and encircled with red and green circles. The magnified SEM images of the selected particles are shown in (d) and (e). (d) A typical schematic of base point, where the bases of 4 nearest triangular pyramids meet together. (e) A typical schematic of apex point. The scale bar in both the the figures (d) and (e) is 50 nm.*

low magnification SEM image of an aggregate of randomly oriented TOH Au NP out of which a high magnification SEM image of an isolated TOH Au particle is selected in Figures 5.9d,e to define locations of the base and apex points to be used in our model calculation. The base point is a common point where the bases of four nearest neighbor pyramids meet together. In our case, point B (or E) is a base point and points A, C, H (or D, F, G) are the apexes of three nearest pyramids. The fourth apex point cannot be seen, as it is situated in the lower part of the particle. We will only focus on the electron beam induced LSP responses from the

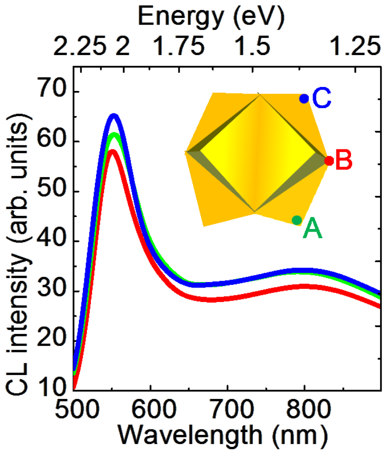

Figure 5.10: *3D-FDTD simulated CL spectrum from the selected points of the TOH structure for modelling under free-standing configuration. The spectra are calculated within the 500-900 nm wavelength range. The beam injected points and the corresponding spectra are highlighted with same color. The schematic of the TOH model is shown in the inset.*

points A, B and C only in free-standing configuration for which the calculated CL spectra are shown in Figure 5.10, indicating the existence of two LSP modes at 550 nm and 820 nm. While the experimentally observed low wavelength LSP mode (548/560 nm) agrees well with that for free-standing modelled TOH Au particle, the observed high wavelength LSP mode (650/670 nm) is blue shifted substantially with that for free-standing case, which will be discussed later in the context of substrate effect. The nature of the plasmon modes is assigned by observing the standing wave formation through the calculated near electric field intensity maps and the direction of the corresponding electric field vectors.[23, 25, 27, 93, 94] Electric field converging and diverging points are designated as the negatively and positively charged points, respectively.[23, 25, 27, 93, 94] Now, for electron beam excitation at point B, the vector plot of Figures 5.11a and b clearly depict that the LSP mode at 550 nm has dipolar nature of oscillation both in-plane as well as out-of-plane directions. The charges of opposite polarities (±) are observed to be distributed from base point to nearest apex point, e.g., between the points B-A / B-C (in XY plane) or B-H (in XZ plane). The corresponding near-field intensity map illustrates the localized and strong electric field enhancements near the points A, B, C and H. However, for electron beam excitation at point A or C, the dipolar charge oscillation between base and apex for the LSP mode at 550 nm occurs in the in-plane direction (XY plane) as revealed from the vector plots of Figures 5.11c and d. Although it seems that the field lines are emanating from the point F to C or D to A at 550 nm wavelength for electron beam excitation at point C or A (Figures 5.11c and d); however, they may also emerge from any other base points which are situated at lower portion of the particle and they are also connected with point C or A. The near-electric field intensity map also shows the strong enhancements at the negatively and positively charged regions. Interestingly, as the induced EM field from the electron beam may extend over the entire nanoparticle under resonance condition,[93] one can also observe the field enhancement at other points as well (i.e., point E in the present case) of the nanoparticle. However, the other points (i.e., the point E) do not take part in standing wave loop formation for 550 nm base-apex LSPR mode when the electron beam is probed at point B. On the other hand, for electron beam excitation either at point C or A, the higher wavelength (or lower energy) LSP mode at 820 nm also exhibits dipolar nature. However, the charge pattern oscillations occur between two nearest apex points (e.g. A-D, C-F) of TOH Au particle, as seen from Figures 5.11e and f. Geometrically, any apex of a TOH Au particle has three nearest neighbor apex points (shown in Figure 5.4e) owing to the three fold rotational symmetry.[79] This leads to a signature of 3-fold degenerate dipolar mode at the wavelength of $\lambda =$

820 nm in free-standing configuration for electron beam probe positioned at one of the symmetric [26, 27] apex points. The distance between two nearest apexes, namely, A-D or C-F is 150 nm, as measured from inset SEM image of Figure 5.6a. It is greater than that between a nearest apex and a base point (B-A or B-C). Consequently, the apex-apex dipole active mode appears at higher wavelength of 820 nm compared to the dipolar LSP modes at 550 nm along the apex-base (A-B, B-C etc.) edges.

We now discuss the role of substrate on the observed spectra. Comparing the calculated scattering spectra of TOH Au particle for free standing condition of Figure 5.10 with the calculated spectra of Figure 5.6b for particle configured with the experimental situation, one can get a hint on the role of substrate, specifically, for the lower energy degenerate apex to apex dipole active mode. In general, the longitudinal in-plane dipolar component of particles with simple geometry like rod, triangular prism [23, 25, 93] shows the redshift with respect to the free space

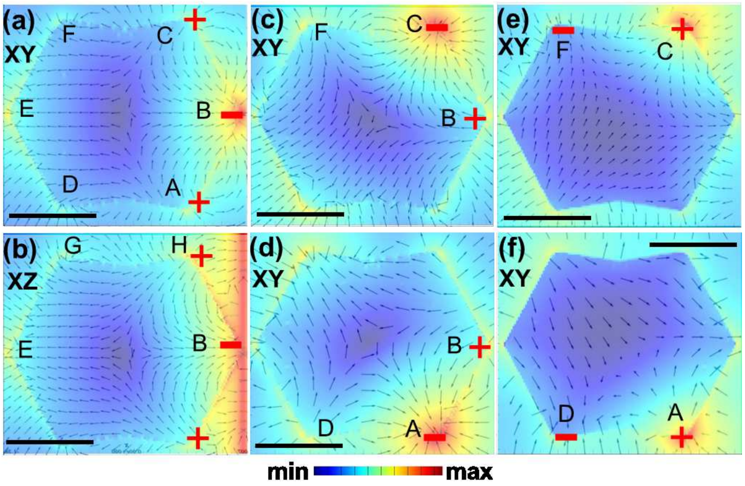

Figure 5.11: *3D-FDTD simulated near-field intensity ($|E|^2$) and corresponding field vector maps at resonant wavelengths 550 nm (a)-(d), and 820 nm (e), (f). Scale bar is 100 nm.*

resonance wavelength in presence of high index substrate. However, for TOH Au particle, the dipolar LSP modes are not so well defined in longitudinal and transverse directions as in the case for a particle with simple rod like morphology. The LSP modes are oriented along different directions due to the 3D orientations of different apex points. The modal distribution analyzed for e-beam injections at point B and C in the present case is much more complex than a simple elongated particle. Additionally, the losses due to the interband electronic transitions in Au, may play an important role in LSPR responses,[192] especially in the visible and ultra-violet (UV) spectral ranges (mainly 500-600 nm) when the Au TOH particle is exposed to the highly energetic electrons. In the present work, we have considered the dielectric permittivity tabulated by CRC [184] for the modeled Au TOH nanoparticle during the simulations where the losses are not taken into account. Moreover, the simulated results could be suffered due to the imperfect experimental structure or the meshing in FDTD simulations along with the transition losses.[193] Although the FDTD simulated results provide a qualitative perception about the substrate mediated interaction [26, 27, 194–196] on apex-apex dipolar LSP mode, quantitative assessment of the blue shifted nature of the apex-apex mode is difficult due to intricate morphology of the complex shaped TOH Au particle in presence on substrate. However, the apex-apex mode is not present in both experimental and calculated spectra (Figures 5.6a and b) for electron beam excitation at points A and D. This is because, the apex points, A and D, are very close to the high index substrate like Si compared to any other points and the apex-apex LSPR mode corresponding to these points will tend to radiate mostly into the substrate.[27] It is also observed that the base-apex LSP modes like A-B, B-C do not show any noticeable shift in spectra when the substrate is taken into account. This is consistent with the monochromatic CL map corresponding to the base-apex mode either at 548 nm or 560 nm showing (Figures 5.6e or f) that the strong luminescence coming from the base and apex points of the TOH Au particle. Recently, in a few publications,[58, 69] it is reported that the quadrupolar nature of the lower wavelength LSPR mode of Au TOH NPs may appear along with the dipolar one for the increased size of the TOH Au particle. It is established for a single particle that the higher order modes (like quadrupolar) are less affected by the substrate compared to the dipolar modes,[93] which is consistent with the present analyses where the substrate effect is negligible for the lower wavelength LSP mode with respect to the free standing case. Insignificant substrate effect is also reported [94] even in case of a mixed mode, which appears at higher energy or lower wavelength region of spectrum. Moreover, the broadening of a LSPR peak is generally regarded as the mixing of different plasmon modes for complex shaped nano-objects studied by CL spectroscopy. [26] The broadening of the 550 nm LSP mode may suggest a certain probability of the presence of quadrupolar mode in our result.

5.3.2 SERS analyses

The strength of the LSPR of TOH Au NPs in SERS activity was studied by collecting the Raman spectra of Rhodamine 6G (R6G) molecules, dispersed on SERS substrates containing ensemble of Au NPs. Since it is difficult to probe the SERS activity of single TOH Au particle having size below the optical resolution of a microscope, the SERS studies were carried out on ensemble Au NPs. Though SERS is measured on the ensemble of NPs, the hot spot at the individual NPs

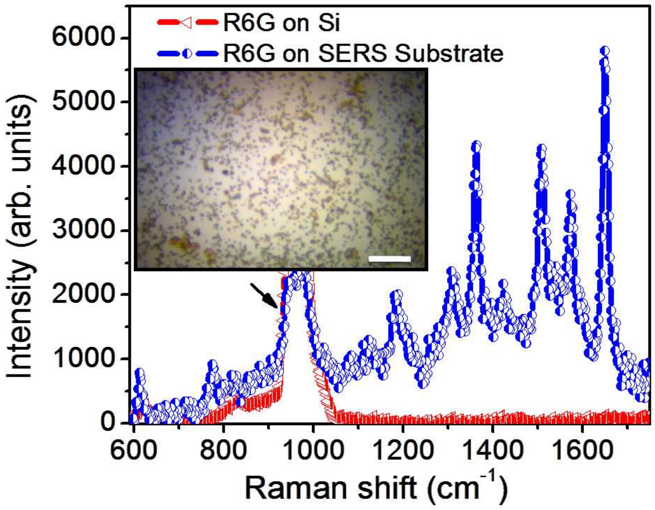

Figure 5.12: *SERS spectra of R6G molecules in aqueous solution of 10*$^{-6}$ *M concentration dispersed on SERS substrate and pure Si substrates. Arrow mark denotes the second order Raman mode of Si substrate. Inset represents the optical image of the SERS substrate at 100X magnification. Scale bar is 10* μ*m.*

or in the nanogap of two NPs will be primarily responsible for the ambiguity free measurement of the Raman enhancement. Generally SERS measurement is understood as a far-field measurement technique; however the information emerging from a localized interaction of the molecular dipoles with the near-field evanescent wave generated by the interaction of electromagnetic excitation and Au NPs remains intact even in the far-field.[172] An optical view of the SERS substrate with uniformly dispersed TOH Au NPs is shown (shown in inset, Figure 5.12). The aqueous solution of 10^{-6} M concentration of R6G molecules was dispersed on both SERS and pristine Si substrates to compare the spectral enhancement. The prominent Raman modes observed at 611, 773, 1123, 1188, 1307, 1364, 1423, 1509, 1573, and 1650 cm^{-1} (Figure 5.12) are corresponds to R6G molecules on SERS substrate.[37, 197] A broad peak around 958 cm^{-1} corresponds to the second order Raman mode of Si substrate. All the Raman modes of R6G molecules on SERS substrate have shown the enhancement in intensity, as compared to that of the pristine Si substrate. The highest enhancement was observed for 1650 cm^{-1} mode. Considering the effective laser excitation volume ($V = \pi r^2\delta$ = $15.32\ \mu m^3$; where r being radius of laser spot, δ being depth of focus) by 100X objective (N.A = 0.85) and the surface area of a single TOH Au NP, the enhancement factor (EF) of a Raman mode was estimated [58, 68] by, EF = (I_{SERS} N_{normal} / I_{normal} N_{SERS}). I_{SERS} and I_{normal} are the intensity of particular Raman mode observed in the SERS and normal spectra, respectively; N_{normal} and N_{SERS} are the number of R6G molecules in the excitation volume for the normal Raman acquisition and number of adsorbed molecules on individual TOH Au particle, respectively. N_{normal} = $(V\rho/M)N_A$ is estimated to be 2.4×10^{10} . Here ρ (1.26 $\mathrm{g.cm}^{-3}$) and M (479.02 $\mathrm{g.mol}^{-1}$) represent the density and molar mass of R6G molecules and N_A being Avogadro number. Assuming monolayer formation of R6G molecules (molecular foot print size $\approx$ 2.2 nm^2) on TOH Au particle (surface area is calculated 480×10^3 nm^2), we have estimated the N_{SERS} to be 216×10^3. The estimated EF for the 1650 cm^{-1} mode is found to be of the order of 10^8. The observed significant enhancement in the Raman scattering on TOH Au particles may be the result of hotspots present at the tips of each particle (as shown in Figures 5.6d-h), as well as in between the particles adjacent to each other. The enhancement in the present study can be understood by invoking a general principle of energy conservation, for which the total electromagnetic energy per unit volume containing several nanoparticles should be same for any shape. In such situation, due to the strong nonlinearity of the SERS enhancement factor, one strong hotspot may lead to higher SERS enhancement than many weaker hot spots. It is known

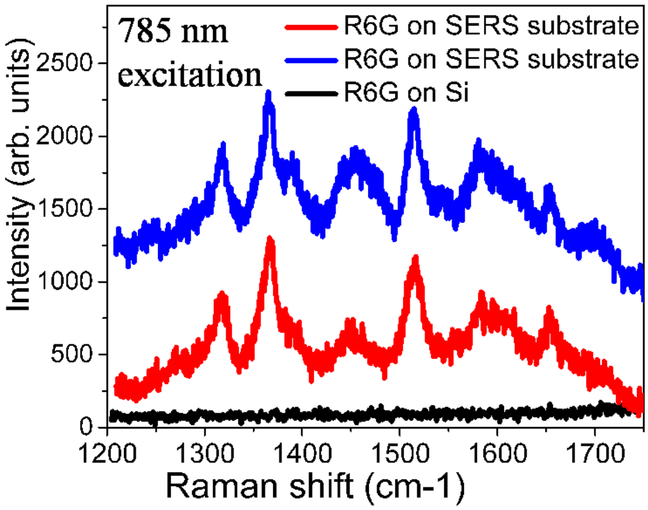

Figure 5.13: *SERS spectra of R6G molecule (1 μM) at different locations of the substrate, with excitation laser of wavelength 785 nm.*

that on-resonance excitations of Au NPs generate stronger field strength needed for Raman enhancements than the off-resonance excitation. However, the Raman scattering cross-section and molecular resonance for particular molecule depend on the excitation wavelength. In this context, we have investigated the SERS of R6G by choosing the resonance excitation of TOH Au NPs, which is close to 785 nm (Figure 5.13). The estimated EF, however, is one order less (10^7) compared to that of 514.5 nm excitation.

The SERS activity of the TOH Au NPs was tested for wide range of molar concentrations (10^{-3} to 10^{-8} M) of R6G and found that the TOH Au NPs are able to detect the R6G molecules of concentration up to 10^{-7} M (Figure 5.14). Further, the areal distribution of enhancement regions on the SERS substrate was mapped by performing the SERS imaging of R6G molecules. An area of 6 μm × 6 μm on SERS substrate containing R6G of concentration 10^{-6} M, was chosen for imaging (Figure 5.15a). The mapped integral intensity distribution of 1650 cm^{-1} mode of

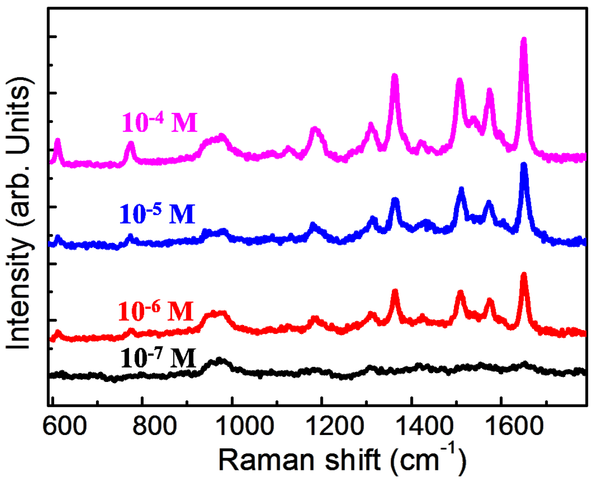

Figure 5.14: *SERS spectra of R6G molecules in different aqueous solutions of concentrations ranging from* 10^{-4} *to* 10^{-7} *M, dispersed on SERS substrates*

R6G (Figure 5.15b) shows the high intensity spots randomly distributed over the mapped area. Interestingly, one can notice from the optical image of the Au NPs on SERS substrate as shown in Figure 5.15a and also from SEM image of Figures 5.5a, c and Figure 5.9c that the Au NPs are mostly in the form ensembles implying the existence of the "nanogaps" (< 100 nm) between the Au TOH NPs. Meaning, we can not unambiguously say that maximum intensity regions in the SERS map correspond to the location of hot spots where field enhancement occurred by the LSPR of single TOH Au NPs because of the diffraction limited lateral resolution of Raman microscope (∼ 370 nm in the present case) (Figure 5.15b). However, due to the strong plasmonic coupling effects,[9] the nanogaps between the adjacent particles of the ensembles on substrate may serve as hot spots with gigantic local-field enhancements of several orders of magnitude higher than those achievable for LSPR of individual NP. We believe that such a strong hot spot could be responsible for the significant SERS enhancement observed for present TOH particles. Apart

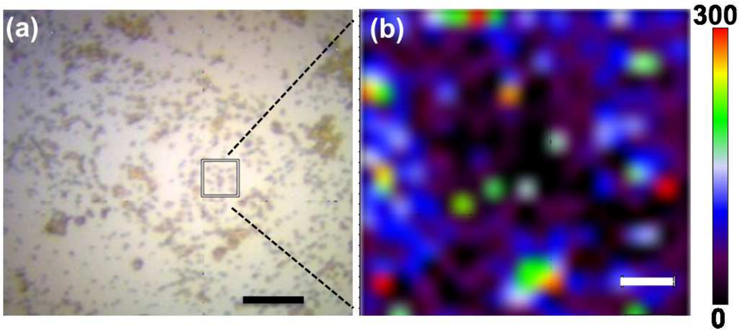

Figure 5.15: *Optical view of SERS substrate containing R6G molecules of concentration 10^{-6}M, used for SERS imaging.(a) The square box indicates the area (6 μm × 6 μm) chosen for SERS imaging of R6G. Scale bar is 10 μm.(b) The SERS map of 1650 cm^{-1} mode of R6G. Scale bar is 1 μm. The color scale bar indicates the intensity profile of the Raman mode.*

from it, the modal distributions as well as the mixing or interference of the particle plasmon modes [92] in case of anisotropic and complex shaped finite nanostructures also play very crucial role in optical properties including SERS activity of the particles. The higher order plasmon mode, i.e., the quadrupolar mode which is supposed to be present to some extent as described in our CL analysis is generally of nonradiative nature. But they can absorb light and decay through evanescent near-field, and thus may also contribute to SERS enhancements.[92]

5.4 Conclusions

In conclusion, site specific cathodoluminescence spectroscopy and imaging in a scanning electron microscope are used to study the localized surface plasmon behavior of TOH Au NCs. The CL analyses combined with FDTD simulations have helped us to identify two dipole-active LSP modes. The higher wavelength (low energy) surface plasmon mode is governed by the dipolar mode of oscillations between the apexes of the particle, which is basically 3-fold degenerate in nature. The dipolar oscillation is also active for lower wavelength (higher energy) LSP mode but charge pattern oscillation takes place between base and apex points along the in-plane and out-of-plane direction. The proximity of the substrate with respect to the point of excitation also plays a role, especially on the degenerate apex-apex LSP mode of nanoparticle due to inherent anisotropy and complexity of the TOH Au particle. The remarkably high SERS response of the present TOH particles can be understood by invoking a general principle of energy conservation, for which the total electromagnetic energy per unit volume containing several nanoparticles should be same for any shape. Moreover, it is believed that hot spots between two close-by TOH particle surfaces (so called 'nanogaps') can be significantly stronger than single particle LSPRs indicating that MNPs aggregates may serve as reliable SERS substrate as compared to individual plasmonic nanoparticles for sensing and imaging applications.

Chapter 6

Summary and outlook

A quick recapitulation has been made on the works discussed in this thesis and the general conclusions are summarized. Some future prospects of our study have also been discussed in addition.

6.1 Summary

In recent years, cathodoluminescence (CL) spectroscopy and imaging has immersed as a powerful technique to investigate the localized surface plasmon assisted optical response of individual metal nanoparticle. The main goal of this thesis is to explore the surface plasmon enhanced optical properties of the complex shaped metal nanoparticles through CL spectroscopy and imaging technique in a high resolution scanning electron microscopy (SEM). Also, the surface enhanced Raman scattering (SERS) studies are partly carried out to demonstrate the significance of field enhancement under localized surface plasmon resonance conditions in complex shaped gold metal nanoparticles.

- In **Chapter 1** a broad overview of optical properties of metal nanoparticles has been presented. In case of metal nanoparticles, the optical properties are dominated mainly by contribution from collective oscillations of electrons in the conduction band commonly termed as surface plasmon plasmons. It has been discussed why single particle spectroscopy and imaging with nanometer scale spatial resolution is essential to probe the optical properties of individual matal nanoparticles (MNPs). Also, the importance of studying the surface plasmon properties of complex shaped gold nanoparticles has been discussed.

- **In chapter 2**, a brief description of the synthesis of complex shaped Au nanoflower (NF) and trisoctahedral (TOH) NPs is presented. The experimental techniques for their morphological, elemental, structural and plasmon driven optical studies have also been discussed. The detailed synthesis protocol of Au NF and TOH shaped particle through seed mediated wet chemical synthesis mechanism is discussed. Since the SEM-CL is the major characterization tool in this thesis it has been discussed in detail. The working principles of TEM, EDS and SERS techniques are also discussed in this chapter.

- **In Chapter 3**, the basic concept of optical properties of MNPs has been discussed. The contents include the optical properties deriving from the coherent oscillation of conducting electrons in MNP depending on the surrounding medium, shape and size of the nanoparticle. The prominent advantages and advances in plasmonic studies of MNPs at single particle level have also been discussed. In this context CL, serves as an ideal tool to do truly single particle spectroscopy and imaging since freely moving beam of energetic electrons serves as an evanescent source of supercontinuum light with a probe diameter down to a few nanometers. One essential tool to understand the plasmonic response of metallic nano objects is the numerical solution of Maxwells equations for complex geometry under consideration. The basic concepts of Finite-difference time-domain (FDTD) numerical simulation have been discussed. The application of FDTD in CL based plasmonics has also been discussed in this chapter. In addition, the basic concept of the electromagnetic field enhancement over the MNP or in their proximity by placing a suitable molecular probe under LSPR condition is discussed.

- **Chapter 4** describes the first experimental realization on the selective excitation of two closely lying tips from the same spherical core of a multitipped gold nanoparticle with flower-like morphology. This gives strong multipeaked resonance in the near-infrared region of the far-field emission spectra showing a clear signature of tip to tip coupling. The cathodoluminescence (CL) technique in a scanning electron microscope (SEM) combined with finite-difference time domain (FDTD) simulation has helped us to identify the coupled plasmon modes to be originated from the interaction between two closely spaced tips with a narrow angular separation. Our analysis further estimates a range of angular separation between the tips that triggers the onset of the intertip coupling.

- Finally in **Chapter 5** the plasmonic response of a single trisoctahedral (TOH) shaped gold (Au) nanocrystals has been discussed. We examine the radiative localized surface plasmon resonance (LSPR) modes of an isolated single TOH Au NC using cathodoluminescence (CL), with high resolution spatial information on the local density of optical states (LDOS) across the visible spectral range. Further, we show pronounced enhancement in the Raman scattering by performing Raman spectroscopic measurements on Rhodamine 6G (R6G)-covered TOH Au NPs aggregates on a silicon (Si) substrate.

6.2 Outlook

The study of optical phenomena related to the electromagnetic response of noble MNPs, which is the topic of this thesis, lead to the development of a fast growing research field called plasmonics. The cathodoluminescence (CL) based experimental methodology and the finite-difference time domain (FDTD) based numerical approach presented in this thesis could be used to investigate a wide range of nanoparticle geometries and associated surface plasmon modes, thus giving insight into the light matter interaction at the nanometer scale. In particular the much higher versatility of a SEM with the increased available currents makes the SEM-CL based technique more successful in analyzing plasmonic systems. This success can be explained by the characteristics of this measurement tool which render it unique: CL has a resolution of few nanometers, does not require complex samples preparations and the measurements are relatively straightforward. Furthermore, as photons are collected, one can use standard optics components to analyze the response of the signal, its polarization state and the angular emission pattern of the emitted visible radiation. With the continuous improvement in modelling and the understanding of plasmon physics, and the parallel advancement in the realization of complex shaped MNPs with precisely controlled structure and composition, in the near future one can easily expect a further increase in the number of technological and scientific applications. For instance, new applications like, time-resolved excitation [160, 198, 199] or bio-imaging [200] capabilities in CL are most likely promised in dynamic studies of light in optical nanomaterials. In addition, the phase mapping/measurement of the induced electric field of a plasmonic system can be retrieved by using the CL technique under the LSPR condition.[201–203] In the coming years CL nanoscopy will play an important role in many scientific developments owing to its broad applicability.

The thesis addresses several problems and in doing that it arises many new problems that are yet to be addressed and will be of importance to nanophotonics community. To study the intertip plasmonic coupling effect of single Au NF, I have done experiments on two closely lying tips from the same spherical core of NF, where both the upper and lower tips were aligned along the same vertical axis of the incoming electron beam. Better understanding in this direction is expected in probing the intertip coupling effect between two or more tips lying on the perpendicular plane of the incoming electron-beam.

In case of TOH particle, CL combined with FDTD simulation have been applied extensively, to probe and visualize the plasmon modes. We believe that the hot spots between two adjacent TOH MNP surfaces (nanogaps) can be significantly stronger than single particle LSPRs. Such nanogaps hot spots may have crucial role on the substantial SERS enhancement observed in this report. Consequently, the present study indicates that MNPs aggregates are highly desirable than individual plasmonic nanoparticles for possible applications in SERS based biosensing. Probing the same particle with light and electron beam simultaneously is also expected to give more insight into the fundamentals of light mater interactions, however that needs a substantial amount of instrumentation. In addition, more interesting Physics lies in probing the coupling between two or more very closely spaced TOH particles.

The prediction of future perspectives in any kind of research field is inherently risky. Nevertheless, because of the highly diverse nature of plasmonics we can assume an exciting future, where, for example, the merging of plasmonics with quantum system, active plasmonics devices made of complex shaped MNPs or biochemical applications are named as future trends.

Bibliography

[1] M. Faraday, Philos. Trans. R. Soc. **147**, 159 (1847).

[2] D. Thompson, Gold Bull. **40**, 267 (2007).

[3] K. M. Mayer and J. H. Hafner, Chem. Rev. **111**, 3828 (2011).

[4] R. H. Doremus, J. Chem. Phys **40**, 2389 (1964).

[5] R. Ritchie, Phys. Rev. **106**, 874 (1957).

[6] G. Mie, Ann. Phys. **330**, 377 (1908).

[7] S. A. Maier and H. A. Atwater, J. Appl. Phys. **98**, 011101 (2005).

[8] F. J. García de Abajo, Rev. Mod. Phys. **82**, 209 (2010).

[9] N. J. Halas, S. Lal, W.-S. Chang, S. Link, and P. Nordlander, Chem. Rev. **111**, 3913 (2011).

[10] H. A. Atwater, Sci. Am. **296**, 56 (2007).

[11] A. Polman, Science **322**, 868 (2008).

[12] H. A. Atwater and A. Polman, Nat. Mater. **9**, 205 (2010).

[13] A. G. Brolo, Nat. Photonics **6**, 709 (2012).

[14] K. Kneipp, Y. Wang, H. Kneipp, L. T. Perelman, I. Itzkan, R. R. Dasari, and M. S. Feld, Phys. Rev. Lett. **78**, 1667 (1997).

[15] C. E. Talley, J. B. Jackson, C. Oubre, N. K. Grady, C. W. Hollars, S. M. Lane, T. R. Huser, P. Nordlander, and N. J. Halas, Nano Lett. **5**, 1569 (2005).

[16] C. Colliex, M. Kociak, and O. Stéphan, Ultramicroscopy **162**, A1 (2016).

[17] X. Huang, I. H. El-Sayed, W. Qian, and M. A. El-Sayed, J. Am. Chem. Soc. **128**, 2115 (2006).

[18] I. H. El-Sayed, X. Huang, and M. A. El-Sayed, Nano Lett. **5**, 829 (2005).

[19] V. Giannini, A. I. Fernandez-Dominguez, S. C. Heck, and S. A. Maier, Chem. Rev. **111**, 3888 (2011).

[20] T. W. Odom and G. C. Schatz, Chem. Rev. **111**, 3667 (2011).

[21] M. Kociak and O. Stéphan, Chem. Soc. Rev. **43**, 3865 (2014).

[22] J. Nelayah, M. Kociak, O. Stéphan, F. J. García De Abajo, M. Tencé, L. Henrard, D. Taverna, I. Pastoriza-Santos, L. M. Liz-Marzán, and C. Colliex, Nat. Phys. **3**, 348 (2007).

[23] P. Das, T. K. Chini, and J. Pond, J. Phys. Chem. C **116**, 15610 (2012).

[24] R. Gómez-Medina, N. Yamamoto, M. Nakano, and F. G. de Abajo, New J. Phys. **10**, 105009 (2008).

[25] P. Das and T. K. Chini, J. Phys. Chem. C **118**, 26284 (2014).

[26] V. Myroshnychenko, J. Nelayah, G. Adamo, N. Geuquet, J. Rodríguez-Fernández, I. Pastoriza-Santos, K. F. MacDonald, L. Henrard, L. M. Liz-Marzán, N. I. Zheludev, et al., Nano Lett. **12**, 4172 (2012).

[27] P. Das and T. K. Chini, J. Phys. Chem. C **116**, 25969 (2012).

[28] A. Maity, A. Maiti, B. Satpati, A. Patsha, S. Dhara, and T. K. Chini, J. Phys. Chem. C **120**, 27003 (2016).

[29] A. Maity, A. Maiti, P. Das, D. Senapati, and T. Kumar Chini, ACS Photonics **1**, 1290 (2014).

[30] P. Das, A. Kedia, P. S. Kumar, N. Large, and T. K. Chini, Nanotechnology **24**, 405704 (2013).

[31] S. Mazzucco, O. Stéphan, C. Colliex, I. Pastoriza-Santos, L. M. Liz-Marzan, J. Garcia de Abajo, and M. Kociak, Eur. Phys. J. Appl. Phys. **54**, 33512 (2011).

[32] C. Hrelescu, T. K. Sau, A. L. Rogach, F. Jäckel, G. Laurent, L. Douillard, and F. Charra, Nano Lett. **11**, 402 (2011).

[33] Y. Wang, T. Yang, M. T. Tuominen, and M. Achermann, Phys. Rev. Lett. **102**, 163001 (2009).

[34] M. L. Juan, M. Righini, and R. Quidant, Nat. Photonics **5**, 349 (2011).

[35] J. N. Anker, W. P. Hall, O. Lyandres, N. C. Shah, J. Zhao, and R. P. Van Duyne, Nat. Mater. **7**, 442 (2008).

[36] A. J. Haes and R. P. Van Duyne, J. Am. Chem. Soc. **124**, 10596 (2002).

[37] S. Nie and S. R. Emory, Science **275**, 1102 (1997).

[38] P. Bharadwaj and L. Novotny, Opt. Express **15**, 14266 (2007).

[39] T. M. Tolaymat, A. M. El Badawy, A. Genaidy, K. G. Scheckel, T. P. Luxton, and M. Suidan, Sci. Total Environ. **408**, 999 (2010).

[40] A. A. Maradudin, J. R. Sambles, and W. L. Barnes, *Modern Plasmonics*, vol. 4 (Elsevier, 2014).

[41] K. A. Willets and R. P. Van Duyne, Annu. Rev. Phys. Chem. **58**, 267 (2007).

[42] E. C. Dreaden, A. M. Alkilany, X. Huang, C. J. Murphy, and M. A. El-Sayed, Chem. Soc. Rev. **41**, 2740 (2012).

[43] D. A. Schultz, Curr. Opin. Biotechnol. **14**, 13 (2003).

[44] D. Thassu, Y. Pathak, and M. Deleers, in *Nanoparticulate Drug Delivery Systems* (CRC Press, 2007), pp. 1–31.

[45] X. Huang and M. A. El-Sayed, Alexandria J. Med. **47**, 1 (2011).

[46] P. K. Jain, I. H. El-Sayed, and M. A. El-Sayed, Nano Today **2**, 18 (2007).

[47] D. Cialla, A. März, R. Böhme, F. Theil, K. Weber, M. Schmitt, and J. Popp, Anal. Bioanal. Chem. **403**, 27 (2012).

[48] S. A. Maier, *Plasmonics: Fundamentals and Applications* (Springer Science+ Business Media, 2007).

[49] W. L. Barnes, A. Dereux, and T. W. Ebbesen, Nature **424**, 824 (2003).

[50] Z. Liu, J. M. Steele, W. Srituravanich, Y. Pikus, C. Sun, and X. Zhang, Nano Lett. **5**, 1726 (2005).

[51] X. Li, L. Jiang, Q. Zhan, J. Qian, and S. He, Colloids Surf., A **332**, 172 (2009).

[52] S. Eustis and M. A. El-Sayed, Chem. Soc. Rev. **35**, 209 (2006).

[53] L. Vigderman, B. P. Khanal, and E. R. Zubarev, Adv. Mater. **24**, 4811 (2012).

[54] C. L. Haynes and R. P. Van Duyne, *Nanosphere Lithography: A Versatile Nanofabrication Tool for Studies of Size-Dependent Nanoparticle Optics* (ACS Publications, 2001).

[55] A. Brioude and M. Pileni, J. Phys. Chem. B **109**, 23371 (2005).

[56] A. M. Angulo, C. Noguez, and G. C. Schatz, J. Phys. Chem. Lett. **2**, 1978 (2011).

[57] H. Wang and N. J. Halas, Adv. Mater. **20**, 820 (2008).

[58] Q. Zhang, N. Large, and H. Wang, ACS Appl. Mater. Interfaces **6**, 17255 (2014).

[59] Q. Zhang, N. Large, P. Nordlander, and H. Wang, J. Phys. Chem. Lett. **5**, 370 (2014).

[60] M. J. Mulvihill, X. Y. Ling, J. Henzie, and P. Yang, J. Am. Chem. Soc. **132**, 268 (2009).

[61] S. Wang, P. Huang, L. Nie, R. Xing, D. Liu, Z. Wang, J. Lin, S. Chen, G. Niu, G. Lu, et al., Adv. Mater. **25**, 3055 (2013).

[62] F. Hao, C. L. Nehl, J. H. Hafner, and P. Nordlander, Nano Lett. **7**, 729 (2007).

[63] L. Shao, A. S. Susha, L. S. Cheung, T. K. Sau, A. L. Rogach, and J. Wang, Langmuir **28**, 8979 (2012).

[64] C. G. Khoury and T. Vo-Dinh, J. Phys. Chem. C **112**, 18849 (2008).

[65] E. Nalbant Esenturk and A. Hight Walker, J. Raman Spectrosc. **40**, 86 (2009).

[66] P. S. Kumar, I. Pastoriza-Santos, B. Rodriguez-Gonzalez, F. J. G. de Abajo, and L. M. Liz-Marzan, Nanotechnology **19**, 015606 (2008).

[67] M. Bardhan, B. Satpati, T. Ghosh, and D. Senapati, J. Mater. Chem. C **2**, 3795 (2014).

[68] Y. Song, T. Miao, P. Zhang, C. Bi, H. Xia, D. Wang, and X. Tao, Nanoscale **7**, 8405 (2015).

[69] Q. Zhang and H. Wang, ACS Catal. **4**, 4027 (2014).

[70] S. Sreedhala, V. Sudheeshkumar, and C. Vinod, Catal. Today **244**, 177 (2015).

[71] W. Lu, A. K. Singh, S. A. Khan, D. Senapati, H. Yu, and P. C. Ray, J. Am. Chem. Soc. **132**, 18103 (2010).

[72] M. Chirumamilla, A. Toma, A. Gopalakrishnan, G. Das, R. P. Zaccaria, R. Krahne, E. Rondanina, M. Leoncini, C. Liberale, F. De Angelis, et al., Adv. Mater. **26**, 2353 (2014).

[73] P. Aldeanueva-Potel, E. Carbó-Argibay, N. Pazos-Pérez, S. Barbosa, I. Pastoriza-Santos, R. A. Alvarez-Puebla, and L. M. Liz-Marzán, ChemPhysChem **13**, 2561 (2012).

[74] T. Zhang, G. Lu, H. Shen, K. Shi, Y. Jiang, D. Xu, and Q. Gong, Sci. Rep. **4** (2014).

[75] Y. Ma, Q. Kuang, Z. Jiang, Z. Xie, R. Huang, and L. Zheng, Angew. Chem., Int. Ed. **47**, 8901 (2008).

[76] Y. Yu, Q. Zhang, X. Lu, and J. Y. Lee, J. Phys. Chem. C **114**, 11119 (2010).

[77] D. Y. Kim, K. W. Choi, S. H. Im, O. O. Park, X.-L. Zhong, and Z.-Y. Li, Adv. Mater. Res. **1**, 1 (2012).

[78] H.-L. Wu, C.-H. Kuo, and M. H. Huang, Langmuir **26**, 12307 (2010).

[79] R. Xu, H. Jiang, C. Song, J. A. Rodriguez, Z. Huang, C.-C. Chen, D. Nam, J. Park, M. Gallagher-Jones, S. Kim, et al., Nat. Commun. **5**, 4061 (2014).

[80] Z. Quan, Y. Wang, and J. Fang, Acc. Chem. Res. **46**, 191 (2012).

[81] M. Fleischmann, P. J. Hendra, and A. J. McQuillan, Chem. Phys. Lett. **26**, 163 (1974).

[82] N. Weiβenbacher, B. Lendl, J. Frank, H. Wanzenböck, B. Mizaikoff, and R. Kellner, J. Mol. Struct. **410**, 539 (1997).

[83] X. Zhang, M. A. Young, O. Lyandres, and R. P. Van Duyne, J. Am. Chem. Soc. **127**, 4484 (2005).

[84] L. Bao, S. Mahurin, R. Haire, and S. Dai, Anal. Chem. **75**, 6614 (2003).

[85] R. M. Jarvis, A. Brooker, and R. Goodacre, Anal. Chem. **76**, 5198 (2004).

[86] M. Culha, D. Stokes, L. R. Allain, and T. Vo-Dinh, Anal. Chem. **75**, 6196 (2003).

[87] Y. C. Cao, R. Jin, and C. A. Mirkin, Science **297**, 1536 (2002).

[88] M. Y. Sha, H. Xu, M. J. Natan, and R. Cromer, J. Am. Chem. Soc. **130**, 17214 (2008).

[89] C. L. Haynes, A. D. McFarland, and R. P. Van Duyne, Anal. Chem. (2005).

[90] P. L. Stiles, J. A. Dieringer, N. C. Shah, and R. P. Van Duyne, Annu. Rev. Anal. Chem. **1**, 601 (2008).

[91] T. Ghosh, P. Das, T. K. Chini, T. Ghosh, and B. Satpati, Phys. Chem. Chem. Phys. **16**, 16730 (2014).

[92] S. P. Hastings, P. Swanglap, Z. Qian, Y. Fang, S.-J. Park, S. Link, N. Engheta, and Z. Fakhraai, ACS Nano **8**, 9025 (2014).

[93] P. Chaturvedi, K. H. Hsu, A. Kumar, K. H. Fung, J. C. Mabon, and N. X. Fang, ACS Nano **3**, 2965 (2009).

[94] A. Maiti, A. Maity, and T. K. Chini, J. Phys. Chem. C **119**, 18537 (2015).

[95] E. Ringe, B. Sharma, A.-I. Henry, L. D. Marks, and R. P. Van Duyne, Phys. Chem. Chem. Phys. **15**, 4110 (2013).

[96] M. G. Blaber, A.-I. Henry, J. M. Bingham, G. C. Schatz, and R. P. Van Duyne, J. Phys. Chem. C **116**, 393 (2011).

[97] C. L. Nehl, H. Liao, and J. H. Hafner, Nano Lett. **6**, 683 (2006).

[98] M. Sandtke and L. Kuipers, Nat. Photonics **1**, 573 (2007).

[99] R. M. Bakker, A. Boltasseva, Z. Liu, R. H. Pedersen, S. Gresillon, A. V. Kildishev, V. P. Drachev, and V. M. Shalaev, Opt. Express **15**, 13682 (2007).

[100] M. Rang, A. C. Jones, F. Zhou, Z.-Y. Li, B. J. Wiley, Y. Xia, and M. B. Raschke, Nano Lett. **8**, 3357 (2008).

[101] M. Bosman, E. Ye, S. F. Tan, C. A. Nijhuis, J. K. Yang, R. Marty, A. Mlayah, A. Arbouet, C. Girard, and M.-Y. Han, Sci. Rep. **3** (2013).

[102] A. L. Koh, K. Bao, I. Khan, W. E. Smith, G. Kothleitner, P. Nordlander, S. A. Maier, and D. W. McComb, Acs Nano **3**, 3015 (2009).

[103] N. Yamamoto, K. Araya, and F. J. García De Abajo, Phys. Rev. B **64**, 205419 (2001).

[104] M. Kuttge, E. J. R. Vesseur, A. Koenderink, H. Lezec, H. Atwater, F. G. de Abajo, and A. Polman, Phys. Rev. B **79**, 113405 (2009).

[105] E. J. R. Vesseur, R. de Waele, M. Kuttge, and A. Polman, Nano Lett. **7**, 2843 (2007).

[106] A. Denisyuk, G. Adamo, K. MacDonald, J. Edgar, M. Arnold, V. Myroshnychenko, M. Ford, F. J. García de Abajo, and N. Zheludev, Nano Lett. **10**, 3250 (2010).

[107] M. W. Knight, L. Liu, Y. Wang, L. Brown, S. Mukherjee, N. S. King, H. O. Everitt, P. Nordlander, and N. J. Halas, Nano Lett. **12**, 6000 (2012).

[108] E. M. Purcell and C. R. Pennypacker, Astrophys. J. **186**, 705 (1973).

[109] V. Myroshnychenko, J. Rodríguez-Fernández, I. Pastoriza-Santos, A. M. Funston, C. Novo, P. Mulvaney, L. M. Liz-Marzán, and F. J. G. de Abajo, Chem. Soc. Rev. **37**, 1792 (2008).

[110] A. Taflove and S. C. Hagness, *Computational Electrodynamics* (Artech house, 2005).

[111] F. G. de Abajo and A. Howie, Phys. Rev. Lett. **80**, 5180 (1998).

[112] U. Hohenester and A. Trügler, Comput. Phys. Commun. **183**, 370 (2012).

[113] J. M. McMahon, A.-I. Henry, K. L. Wustholz, M. J. Natan, R. G. Freeman, R. P. Van Duyne, and G. C. Schatz, Anal. Bioanal. Chem. **394**, 1819 (2009).

[114] X. Lu, M. Rycenga, S. E. Skrabalak, B. Wiley, and Y. Xia, Annu. Rev. Phys. Chem. **60**, 167 (2009).

[115] M. L. Personick and C. A. Mirkin, J. Am. Chem. Soc. **135**, 18238 (2013).

[116] P. Das and T. K. Chini, Curr. Sci **101**, 849 (2011).

[117] E. Smith and G. Dent, *Modern Raman Spectroscopy: A Practical Approach* (John Wiley & Sons, 2013).

[118] U. Kreibig and M. Vollmer, *Springer Series in Materials Science* (Springer Berlin Heidelberg, 1995).

[119] V. Amendola, R. Pilot, M. Frasconi, O. M. Maragò, and M. A. Iatì, J. Phys.: Condens. Matter **29**, 203002 (2017).

[120] P. Biagioni, J.-S. Huang, and B. Hecht, Rep. Prog. Phys. **75**, 024402 (2012).

[121] J. Zuloaga and P. Nordlander, Nano Lett. **11**, 1280 (2011).

[122] M. A. Kats, N. Yu, P. Genevet, Z. Gaburro, and F. Capasso, Opt. Express **19**, 21748 (2011).

[123] C. F. Bohren and D. R. Huffman, *Absorption and Scattering of Light by Small Particles* (John Wiley & Sons, 2008).

[124] F. Borghese, P. Denti, R. Saija, G. Toscano, and O. Sindoni, Aerosol Sci. Technol. **3**, 227 (1984).

[125] P. K. Jain, K. S. Lee, I. H. El-Sayed, and M. A. El-Sayed, J. Phys. Chem. B **110**, 7238 (2006).

[126] E. Petryayeva and U. J. Krull, Anal. Chim. Acta **706**, 8 (2011).

[127] K. A. Willets, Prog. Surf. Sci. **87**, 209 (2012).

[128] J. Mock, M. Barbic, D. Smith, D. Schultz, and S. Schultz, J. Chem. Phys. **116**, 6755 (2002).

[129] S. W. Prescott and P. Mulvaney, J. Appl. Phys. **99**, 123504 (2006).

[130] N. R. Jana, L. Gearheart, and C. J. Murphy, J. Phys. Chem. B **105**, 4065 (2001).

[131] C. J. Murphy, N. R. Jana, et al., Adv. Mater. **14**, 80 (2002).

[132] S. Link and M. A. El-Sayed, *Spectral Properties and Relaxation Dynamics of Surface Plasmon Electronic Oscillations in Gold and Silver Nanodots and Nanorods* (ACS Publications, 1999).

[133] L. J. Sherry, S.-H. Chang, G. C. Schatz, R. P. Van Duyne, B. J. Wiley, and Y. Xia, Nano Lett. **5**, 2034 (2005).

[134] X. Kou, Z. Sun, Z. Yang, H. Chen, and J. Wang, Langmuir **25**, 1692 (2008).

[135] P. Matteini, M. de Angelis, L. Ulivi, S. Centi, and R. Pini, Nanoscale **7**, 3474 (2015).

[136] J. Romo-Herrera, A. González, L. Guerrini, F. Castiello, G. Alonso-Nuñez, O. Contreras, and R. Alvarez-Puebla, Nanoscale **8**, 7326 (2016).

[137] M. Rycenga, M. R. Langille, M. L. Personick, T. Ozel, and C. A. Mirkin, Nano Lett. **12**, 6218 (2012).

[138] R. Bukasov and J. S. Shumaker-Parry, Nano Lett. **7**, 1113 (2007).

[139] K. O. Aruda, M. Tagliazucchi, C. M. Sweeney, D. C. Hannah, G. C. Schatz, and E. A. Weiss, Proc. Natl. Acad. Sci. U. S. A. **110**, 4212 (2013).

[140] A. Alabastri, S. Tuccio, A. Giugni, A. Toma, C. Liberale, G. Das, F. D. Angelis, E. D. Fabrizio, and R. P. Zaccaria, Materials **6**, 4879 (2013).

[141] Y. Bao, B. Zhao, D. Hou, J. Liu, F. Wang, X. Wang, and T. Cui, J. Appl. Phys. **115**, 223503 (2014).

[142] Y. Bao, B. Zhao, X. Tang, D. Hou, J. Cai, S. Tang, J. Liu, F. Wang, and T. Cui, Appl. Phys. Lett. **107**, 201909 (2015).

[143] J. A. Scholl, A. L. Koh, and J. A. Dionne, Nature **483**, 421 (2012).

[144] S. Malola, L. Lehtovaara, J. Enkovaara, and H. Hakkinen, ACS Nano **7**, 10263 (2013).

[145] S. K. Ghosh and T. Pal, Chem. Rev. **107**, 4797 (2007).

[146] R. Vogelgesang and A. Dmitriev, Analyst **135**, 1175 (2010).

[147] H. Okamoto and K. Imura, Prog. Surf. Sci. **84**, 199 (2009).

[148] A. Lewis, M. Isaacson, A. Harootunian, and A. Muray, Ultramicroscopy **13**, 227 (1984).

[149] U. C. Fischer and D. Pohl, Phys. Rev. Lett. **62**, 458 (1989).

[150] E. Betzig, J. Trautman, et al., Science **251**, 1468 (1991).

[151] E. Synge, Philos. Mag. **6**, 356 (1928).

[152] J. Rodríguez-Fernández, C. Novo, V. Myroshnychenko, A. M. Funston, A. Sánchez-Iglesias, I. Pastoriza-Santos, J. Pérez-Juste, F. J. Garcia De Abajo, L. M. Liz-Marzán, and P. Mulvaney, J. Phys. Chem. C **113**, 18623 (2009).

[153] A. D. McFarland and R. P. Van Duyne, Nano Lett. **3**, 1057 (2003).

[154] K. Lindfors, T. Kalkbrenner, P. Stoller, and V. Sandoghdar, Phys. Rev. Lett. **93**, 037401 (2004).

[155] W.-S. Chang, L. S. Slaughter, B. P. Khanal, P. Manna, E. R. Zubarev, and S. Link, Nano Lett. **9**, 1152 (2009).

[156] E. Le Ru and P. Etchegoin, *Principles of Surface-Enhanced Raman Spectroscopy: and Related Plasmonic Effects* (Elsevier, 2008).

[157] R. Aroca, *Surface-Enhanced Vibrational Spectroscopy* (John Wiley & Sons, 2006).

[158] M. Kerker, D.-S. Wang, and H. Chew, Appl. Opt. **19**, 3373 (1980).

[159] M. Kociak, O. Stéphan, A. Gloter, L. F. Zagonel, L. H. Tizei, M. Tencé, K. March, J. D. Blazit, Z. Mahfoud, A. Losquin, et al., C. R. Phys. **15**, 158 (2014).

[160] T. Coenen, B. J. Brenny, E. J. Vesseur, and A. Polman, MRS Bull. **40**, 359 (2015).

[161] Y.-Y. Teng and E. A. Stern, Phys. Rev. Lett. **19**, 511 (1967).

[162] D. Heitmann, J. Phys. C: Solid State Phys. **10**, 397 (1977).

[163] J. Schieber, D. Krinsley, and L. Riciputi, Nature **406**, 981 (2000).

[164] G. Pratesi, A. Lo Giudice, S. Vishnevsky, C. Manfredotti, and C. Cipriani, Am. Mineral. **88**, 1778 (2003).

[165] S. J. Pennycook, Scanning **30**, 287 (2008).

[166] I. Balberg and J. Pankove, Phys. Rev. Lett. **27**, 1371 (1971).

[167] B. Yacobi and D. Holt, J. Appl. Phys. **59**, R1 (1986).

[168] B. G. Yacobi and D. B. Holt, *Cathodoluminescence Microscopy of Inorganic Solids* (Springer Science & Business Media, 2013).

[169] A. C. Atre, B. J. Brenny, T. Coenen, A. García-Etxarri, A. Polman, and J. A. Dionne, Nat. Nanotechnol. **10**, 429 (2015).

[170] A. Losquin, Ph.D. thesis, Paris 11 (2013).

[171] R. Sapienza, T. Coenen, J. Renger, M. Kuttge, N. Van Hulst, and A. Polman, Nat. Mater. **11**, 781 (2012).

[172] L. Novotny and B. Hecht, *Principles of Nano-Optics* (Cambridge university press, 2012).

[173] J.-C. Weeber, A. Dereux, C. Girard, J. R. Krenn, and J.-P. Goudonnet, Phys. Rev. B **60**, 9061 (1999).

[174] K. Imura, T. Nagahara, and H. Okamoto, J. Phys. Chem. **122**, 154701 (2005).

[175] A. L. Aden and M. Kerker, J. Appl. Phys. **22**, 1242 (1951).

[176] P. J. Wyatt, Phys. Rev. **127**, 1837 (1962).

[177] B. T. Draine and P. J. Flatau, J. Opt. Soc. Am. A **11**, 1491 (1994).

[178] K. Yee, IEEE Trans. Antennas Propag. **14**, 302 (1966).

[179] A. Taflove, A. Oskooi, and S. G. Johnson, *Advances in FDTD Computational Electrodynamics: Photonics and Nanotechnology* (Artech house, 2013).

[180] Lumerical-FDTD-Solutions, *Inc. Home Page.* (Lumerical Solutions, v. 7.5.2).

[181] Y. Cao, A. Manjavacas, N. Large, and P. Nordlander, Acs Photonics **2**, 369 (2015).

[182] P. B. Johnson and R.-W. Christy, Phys. Rev. B **6**, 4370 (1972).

[183] E. D. Palik, *Handbook of Optical Constants of Solids*, vol. 3 (Academic press, 1998).

[184] D. R. Lide, *CRC Handbook of Chemistry and Physics* (CRC press, 2004).

[185] L. O. Herrmann, V. K. Valev, C. Tserkezis, J. S. Barnard, S. Kasera, O. A. Scherman, J. Aizpurua, and J. J. Baumberg, Nat. Commun. **5** (2014).

[186] A. Maiti, A. Maity, B. Satpati, N. Large, and T. K. Chini, J. Phys. Chem. C **121**, 731 (2017).

[187] E. Ringe, J. M. McMahon, K. Sohn, C. Cobley, Y. Xia, J. Huang, G. C. Schatz, L. D. Marks, and R. P. Van Duyne, J. Phys. Chem. C **114**, 12511 (2010).

[188] J. R. Lombardi and R. L. Birke, Acc. Chem. Res. **42**, 734 (2009).

[189] S. Simoncelli, E.-M. Roller, P. Urban, R. Schreiber, A. J. Turberfield, T. Liedl, and T. Lohmuller, ACS Nano **10**, 9809 (2016).

[190] A. Patsha, S. Dhara, and A. Tyagi, Appl. Phys. Lett. **107**, 123108 (2015).

[191] A. Patsha, P. Sahoo, S. Dhara, S. Amirthapandian, and A. Tyagi, J. Raman Spectrosc. **44**, 651 (2013).

[192] P. R. West, S. Ishii, G. V. Naik, N. K. Emani, V. M. Shalaev, and A. Boltasseva, Laser Photonics Rev. **4**, 795 (2010).

[193] M. Zhao, M. Bosman, M. Danesh, M. Zeng, P. Song, Y. Darma, A. Rusydi, H. Lin, C.-W. Qiu, and K. P. Loh, Nano Lett. **15**, 8331 (2015).

[194] S. Mazzucco, N. Geuquet, J. Ye, O. Stéphan, W. Van Roy, P. Van Dorpe, L. Henrard, and M. Kociak, Nano Lett. **12**, 1288 (2012).

[195] Y. Wu and P. Nordlander, J. Phys. Chem. C **114**, 7302 (2009).

[196] O. Nicoletti, F. de La Peña, R. K. Leary, D. J. Holland, C. Ducati, and P. A. Midgley, Nature **502**, 80 (2013).

[197] A. M. Michaels, M. Nirmal, and L. Brus, J. Am. Chem. Soc. **121**, 9932 (1999).

[198] M. Kociak and L. Zagonel, Ultramicroscopy **174**, 50 (2017).

[199] M. Kociak, A. Gloter, and O. Stéphan, Ultramicroscopy **180**, 81 (2017).

[200] S. Fukushima, T. Furukawa, H. Niioka, M. Ichimiya, T. Sannomiya, N. Tanaka, D. Onoshima, H. Yukawa, Y. Baba, M. Ashida, et al., Sci. Rep. **6**, 25950 (2016).

[201] H. Saito, N. Yamamoto, and T. Sannomiya, ACS Photonics (2017).

[202] T. Sannomiya, H. Saito, J. Junesch, and N. Yamamoto, Light: Sci. Appl. **5**, e16146 (2016).

[203] N. Yamamoto, J. Electron Microsc. **65**, 282 (2016).